

A theoretical study on the structure dependence of the steam methane reforming reaction by rhodium

Citation for published version (APA):

Grootel, van, P. W. (2012). *A theoretical study on the structure dependence of the steam methane reforming reaction by rhodium*. [Phd Thesis 1 (Research TU/e / Graduation TU/e), Chemical Engineering and Chemistry]. Technische Universiteit Eindhoven. <https://doi.org/10.6100/IR721602>

DOI:

[10.6100/IR721602](https://doi.org/10.6100/IR721602)

Document status and date:

Published: 01/01/2012

Document Version:

Publisher's PDF, also known as Version of Record (includes final page, issue and volume numbers)

Please check the document version of this publication:

- A submitted manuscript is the version of the article upon submission and before peer-review. There can be important differences between the submitted version and the official published version of record. People interested in the research are advised to contact the author for the final version of the publication, or visit the DOI to the publisher's website.
- The final author version and the galley proof are versions of the publication after peer review.
- The final published version features the final layout of the paper including the volume, issue and page numbers.

[Link to publication](#)

General rights

Copyright and moral rights for the publications made accessible in the public portal are retained by the authors and/or other copyright owners and it is a condition of accessing publications that users recognise and abide by the legal requirements associated with these rights.

- Users may download and print one copy of any publication from the public portal for the purpose of private study or research.
- You may not further distribute the material or use it for any profit-making activity or commercial gain
- You may freely distribute the URL identifying the publication in the public portal.

If the publication is distributed under the terms of Article 25fa of the Dutch Copyright Act, indicated by the "Taverne" license above, please follow below link for the End User Agreement:

www.tue.nl/taverne

Take down policy

If you believe that this document breaches copyright please contact us at:

openaccess@tue.nl

providing details and we will investigate your claim.

A Theoretical Study on the Structure Dependence of the Steam Methane
Reforming Reaction by Rhodium

PROEFSCHRIFT

ter verkrijging van de graad van doctor aan de
Technische Universiteit Eindhoven, op gezag van de
rector magnificus, prof.dr.ir. C.J. van Duijn, voor een
commissie aangewezen door het College voor
Promoties in het openbaar te verdedigen
op dinsdag 24 januari 2012 om 16.00 uur

door

Pieter Willem van Grootel

geboren te Roermond

Dit proefschrift is goedgekeurd door de promotoren:

prof.dr.ir. E.J.M. Hensen
en
prof.dr. R.A. van Santen

CIP-DATA LIBRARY TECHNISCHE UNIVERSITEIT EINDHOVEN

Grootel, Pieter W. van

A Theoretical Study on the Structure Dependence of the Steam Methane Reforming Reaction by Rhodium /
by Pieter W. van Grootel - Eindhoven : Technische Universiteit Eindhoven, 2012.
Proefschrift.

A catalogue record is available from the Eindhoven University of Technology Library

ISBN: 978-90-386-3070-0

Trefwoorden: Methaan reformering door stoom, rhodium, oppervlakte chemie, dichtheidspotentialtheorie, microkinetische modellering, katalyse
Subject headings: Steam methane reforming, rhodium, surface chemistry, Density Functional Theory (DFT), microkinetic modelling, catalysis

The work described in this thesis has been carried out at the Schuit Institute of Catalysis, Laboratory of Inorganic Materials Chemistry, Eindhoven University of Technology, The Netherlands. This project has been carried out in the framework of an EOS-LT program financed by SenterNovem. Supercomputing facilities were supported by the National Computational Facilities foundation of the Netherlands Organization for Scientific Research (NWO-NCF).

*Voor Marieke
Voor Femke en Thijmen*

“In theory there is no difference between theory and practice. In practice there is.”

Yogi Berra

Contents

Chapter 1:	Introduction	7
Chapter 2:	Computational Methods	17
Chapter 3:	DFT study on H ₂ O activation by stepped and planar Rh surfaces	25
Chapter 4:	The CO Formation Reaction Pathway in Steam Methane Reforming by Rhodium	43
Chapter 5:	CH ₄ dissociation on high and low indices Rh surfaces	69
Chapter 6:	Microkinetic model of steam methane reformation	87
Summary:	A Theoretical Study on the Structure Dependence of the Steam Methane Reforming Reaction by Rhodium	103
	Samenvatting	109
	Acknowledgements	115
	Curriculum Vitea	117

Chapter 1: Introduction

1.1. Energy and catalysis

A general prediction in many scenario studies about the future supply of energy is that more than half of the global energy demand until 2050 will be met by fossil fuels such as coal, oil and gas. The combustion of these fossil fuels leads to the emission of vast amounts of greenhouse gases, mostly CO₂, into the atmosphere, which leads to global warming. The Kyoto Protocol and other national and transnational regulations commit the European Union to strive for substantial reductions in greenhouse gas emissions. Although it currently seems unlikely that these goals will be met, it has spurred research in the field of carbon capture and sequestration (CCS) technologies [1]. CCS will play an important role in the transition towards a sustainable energy infrastructure. An important advantage of fossil fuels is that these are available in large quantities at relatively low cost, even if the costs for CO₂ capture, transport and sequestration are included. Capturing CO₂ during the energy production from fossil fuels requires additional energy and investments [2]. As in many chemical conversion processes, catalysis will facilitate such processes because it allows chemical reactions to be carried out at lower temperatures (energy efficiency).

In a chemical reaction, the chemical bonds in reactants are dissociated or combined to form products. Catalysts form bonds with the reactants and lower the energy barriers of the dissociation and association reaction steps that lead to the products. This lowers the overall activation energy of the chemical reaction and implies that the same reaction can be carried out at a lower temperature than the uncatalyzed reaction (activity), as exemplified in Figure 1. Catalysts also steer the chemical reaction to certain products (selectivity), when reaction pathways to certain products have higher barriers than others. [3] The importance of catalysis

becomes clear by noting that the manufacture of nearly all base chemicals for consumer products involves catalysts. A very important and clear example is ammonia, which is produced in very large quantities by fixation of nitrogen from air with hydrogen, for fertilizers essential to sustain the large world population. The Haber-Bosch process is economically viable because of the use of catalysts. Another example is the human body, which can only work by virtue of enzymes, which are biological catalysts. The catalyst in the exhaust of a car makes hazardous fumes react into lesser harmful gasses [4].

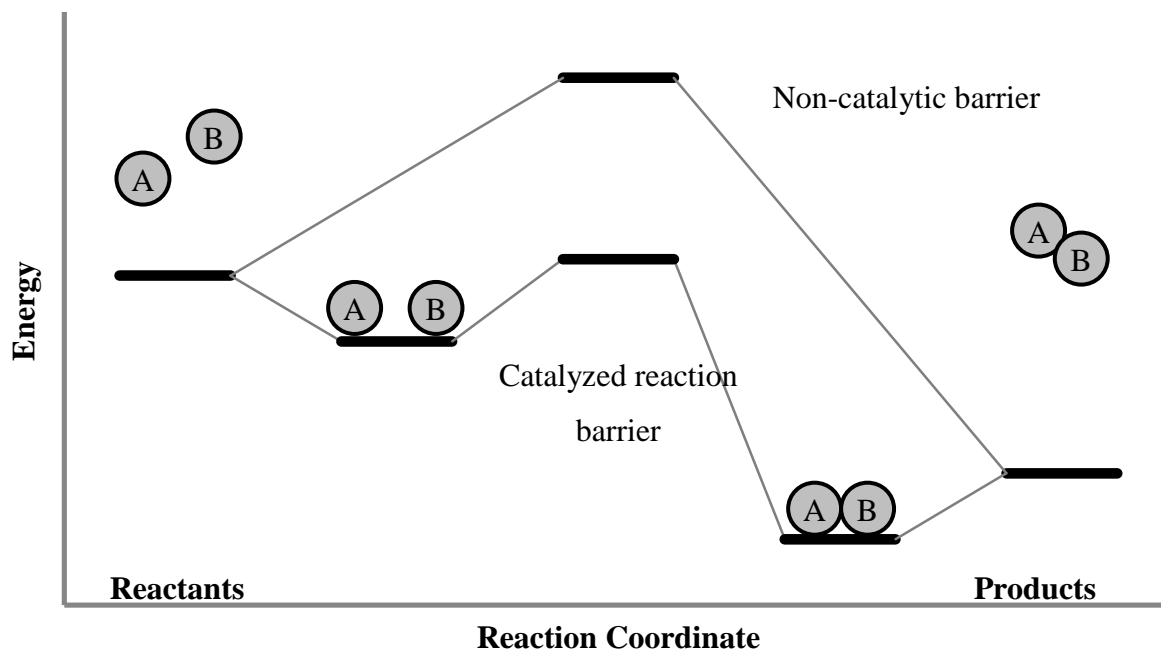


Figure 1. Potential energy diagram of the reaction of $A + B$ to give product AB comparing the catalyzed and the uncatalyzed case.

1.2. Sorption-enhanced steam methane reforming

Typically, three categories of CO_2 capture are distinguished (i) post-combustion CO_2 capture, (ii) pre-combustion CO_2 capture and (iii) oxyfuel combustion [5]. In post-combustion capture, CO_2 is captured from the exhaust gases of power plants using scrubbers, typically with liquid CO_2 adsorption materials. Usually a substantial amount of energy is required to regenerate such solvents. Oxyfuel combustion involves the combustion of fuels by pure oxygen instead of air to obtain concentrated, sequestration-ready CO_2 . This method is also expensive because of the need of air separation. In pre-combustion CO_2 capture the energy content of fossil fuels is transferred to hydrogen with simultaneous separation of CO_2 by either absorption or via a membrane.

In the present work we have focused on Steam Methane Reforming (SMR), the process in which methane is converted with water to hydrogen and carbon monoxide. This mixture is commonly called synthesis gas or syngas. Syngas can subsequently be used to produce higher hydrocarbons or alcohols via the Fischer-Tropsch synthesis reaction [6,7]. When energy production via precombustion CCS is the goal, the water-gas shift reaction is relevant to maximize the hydrogen yield. Commercially, SMR is carried out over Ni-based catalysts [8,9]. A large number of precious metals such as rhodium (Rh), ruthenium (Ru), platinum (Pt) and palladium (Pd) also display a high activity, but are typically not used because of their high cost. Typical reaction temperatures in steam reformers are around 800-900 °C [10-12].

Sorption-enhanced membrane reactors like hydrogen membrane reactors (Figure 2) are an attractive option for CO₂ capture in gas fired power stations [13]. In such a reactor, hydrocarbons are converted by a reforming catalyst, whilst a membrane selectively removes H₂ from the reaction mixture. Since removal of product H₂ shifts the reforming equilibrium to the product side, high conversions can be achieved at relatively low temperatures ($T < 600$ °C). This is advantageous because the metallic membranes for H₂ separation can typically withstand temperatures up to 550-600 °C [14]. The membrane reactor is to be integrated in a conventional power cycle, where the hydrogen is used for power generation and the remaining gas stream is predominantly CO₂ and some non-recovered hydrogen and steam at relatively high pressure. Condensation of the steam leaves concentrated CO₂ at high pressure, reducing the compression energy for transport and storage. A membrane reactor is also a typical example of process intensification. Process intensification with membrane reactors allows for more compact units, lower investment cost, higher yields and reduced energy cost.

A few important differences should be noted between the application of reforming catalysts in separation-enhanced reforming and conventional reforming. Firstly, the catalysts have to operate at significantly lower temperatures, around 550 °C instead of 900 °C. This difference is due to the limited thermal stability of the separation membranes. Another target is to limit the cost of heating. Secondly, the catalysts should be active for both the reforming reaction, converting methane with steam to hydrogen and carbon monoxide (CO) as well as the water-gas shift reaction converting CO and water to carbon dioxide (CO₂). Thirdly, the catalysts should be resistant to deactivation under the anomalous conditions in separation-enhanced reformers. During the reactions high concentrations of either carbon or hydrogen are produced, which may invoke either carbon deposition on the surface of the catalyst or

enhance sintering. A final prerequisite is that catalyst cost should be minimal when the goal is large scale electricity production.

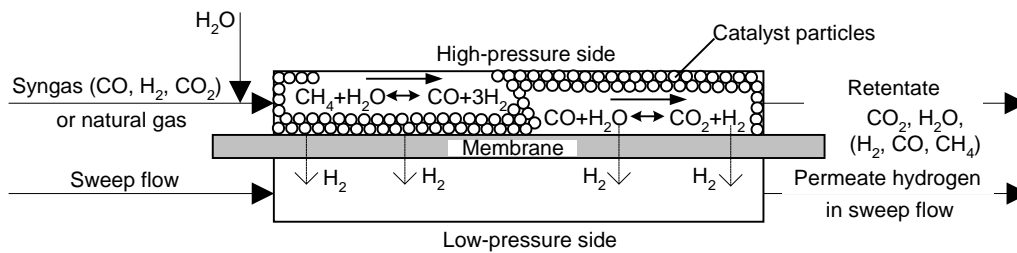


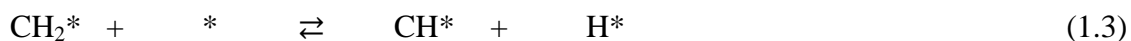
Figure 2. Operating principle of a sorption enhanced membrane reactor

Thus, it is important to identify optimum catalysts for separation-enhanced steam reforming. This may involve improvement of existing commercial Ni based catalysts, for instance by using promoters [15]. The other approach would be to use and optimize other intrinsically more active metals, since high activity at low temperature is desirable. It is hence reasonable to explore the use of noble metals such as Rh, Ru and Pd that have been reported to be much more active than Ni [10-12,16-21]. Of these metals, Rh is the most active metal for SMR and has therefore been chosen as the object of our investigations.

1.3. Mechanism of the SMR reaction

During the SMR reaction a range of surface-catalyzed processes take place in a consecutive as well as in a parallel manner. The reaction is initiated by the activation of methane on the surface resulting in the adsorbed CH_x fragments. Besides that, water also dissociatively adsorbs on the surface. To produce CO, the adsorbed CH_x fragments have to react with O adatoms resulting from dissociative water adsorption.

The dehydrogenation of methane occurs in a consecutive manner via



with $*$ indicating a vacant surface site and X^* the adsorbed X surface intermediate. The adsorbed CH^* either dissociate in C^* and H^* or react with other oxygen containing surface intermediates to HCO^* or COH^* . This essentially leads to three different pathways for the formation of adsorbed CO:

Pathway I:



Pathway II:



Pathway III:



The oxygen to remove the carbon surface adatoms originates either directly from water via:



or via an oxygen-assisted pathway.



1.4. Basic concepts in heterogeneous catalysis

Theoretical catalysis has developed several important concepts that will be used throughout this work, namely the Bond Order Conservation (BOC) principle, linear activation energy-reaction energy relationships and the Sabatier principle.

The interaction of a transition metal surface with an atom or a molecule changes the electronic structure of both the adsorbed species and the metal atoms involved in the surface chemical bond. Upon chemical bond formation the interaction between the metal atoms within the surface weakens. The essential assumptions made according to the BOC principle [22] is that the valency of a metal atom is constant. By describing the total bond strength as a sum of two-body interactions and assuming that the valency or the total bond order of an atom does not depend on the number and the type of the neighbors, it follows that the total bond order or valency is conserved. By using the BOC principle one can readily explain why the interaction energies with a surface atom increase when its coordination number to neighboring metal atoms decreases [23].

The other important concept is a linear activation energy-reaction energy relationship that can be deduced for elementary surface reactions [24]. In heterogeneous catalysis this concept is usually called the Brønsted-Evans-Polanyi (BEP) relationship and is described by the following formal equations:

$$\delta E^\# = \alpha \delta E_R \text{ with } 0 < \alpha < 1 \quad (1a),$$

where $\delta E^\#$ is the change in activation energy, δE_R is the corresponding change in reaction energy, and the BEP coefficient being

$$\alpha = \frac{1}{2} \left(1 + \frac{E_R}{E_0^\#} \right) \quad (1b).$$

For the reverse reaction the BEP relationship is then

$$\delta E^\# = -(1 - \alpha) \delta E_R \quad (1c).$$

$E^\#$ is the activation energy of a reaction, E_R is the reaction energy. $E_0^\#$ is the activation energy for the system for which the reaction energy $E_R=0$.

For many surface elementary reaction steps these relations have been validated. The relation applies as long as there is no major change in the transition state structure of the reactions that are compared. For dissociation reactions of CO or N₂ into surface adatoms, the value of α is typically 0.9. The activation energy for the dissociation reaction depends very strongly on the type of metal. It should be noted that the reverse recombination reaction of the surface adatoms to produce the molecule is independent of the metal. The value of α close to 1 implies that the transition state of dissociation is close in structure to dissociated product state.

The third important catalytic concept is the Sabatier principle. This principle gives rise to the frequently observed volcano shaped dependences when the rate of a catalytic reaction is plotted as a function of the interaction energy of reactant molecules with the catalyst surface. Examples of such behaviour are ammonia synthesis and hydrodesulfurization. It essentially relates to the kinetic consequence of the cyclic nature of a catalytic reaction event [25]. When the catalytic cycle is completed the active site must become again available for reaction. The rate of the catalytic reaction is maximum for an optimum value of the interaction energies between the surface and the reactant. For example, if the affinity between the reagents and the catalyst surface is low, there is only a small chance that they collide and the reaction

event occurs. In this case, the low rate of the initial activation of the reactants will lead to a decrease of the overall rate. Similarly, when the interaction between the catalyst surface and reactant is too strong, the regeneration of the active surface sites will require too high energies and again the overall catalytic reaction will be slow. Only when the elementary rates of the initial reactant activation and the final product desorption balance each other, the overall reaction rate is maximal.

Heterogeneous catalysis mostly refers to the case of a solid catalyst used to convert gaseous and/or liquid reactants. The elementary reaction steps, adsorption of reactants, dissociation and association reactions on the surface and desorption of the products, take place at the solid–gas or solid–liquid interface. As catalysis is a surface phenomenon, it is easily seen that the surface of the primary catalyst particles should be as high as possible. However, the surface catalytic properties of solids are often significantly changed when the size of nanoparticles becomes smaller than about 10 nm [26]. For small particles, a significant fraction of the surface will contain sites different from the regular terraces that dominate the surfaces of large particles. The edges and corners of nanoparticles have a lower coordination number than the atoms that make up the terraces and, consequently, bind adsorbates more strongly. This stronger binding of adsorbates may influence the surface reactivity, as for instance known for the C-H bond cleavage in CH₄. The strong binding of the CH₃ and H fragments in the transition state leads to its stabilization and, henceforth, to a lower barrier for dissociative methane adsorption. The surface may also contain specific arrangements of the atoms in such way that a step-edge site is obtained. These latter sites are known to be particularly active for dissociation and formation of diatomic molecules with π -bonds such as NO, CO and N₂ [26,27,28]. As the surface free energy of such more open sites will be higher than that of closed packed surfaces, the probability of finding these particular sites will increase with the particle size. It is therefore essential to understand the relation between the surface metal atom topology and coordination and reactivity.

1.5. Scope of thesis

The goal of this thesis is to investigate the structure dependence of the steam methane reforming reaction for Rh. Based on modern insights into the effect of particle size on the elementary surface reaction steps, it is expected that the proportion of different sites on Rh nanoparticles (terrace, edges, corners and step edges, Figure 3) will substantially and

differently influence the rates of the elementary reaction steps. Candidate rate controlling steps are CH_4 and H_2O activation (reactions 1.1 and 1.11) and CO recombination (reaction 1.5). Since it is not directly obvious how a change in the rate of any of the elementary reaction steps influences the overall reaction rate, a microkinetic model will be employed. This model aims to predict the overall reaction rate for different surfaces based on the rate constants of the elementary reaction steps computed by ab initio methods.

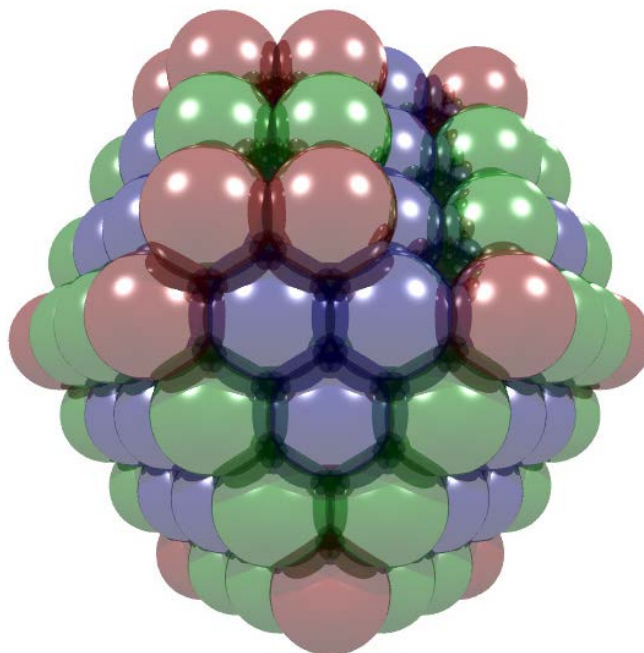


Figure 3. A spherical crystal with (111) and (100) planes exposed. The atoms in the plane have a coordination number of nine (blue), whereas those on the intersection of the plane, which are called corner atoms, have seven (green). The atoms marked red are the edge atoms, also with a coordination number of seven, but the atom in the lower plane underneath it, has eleven.

Chapter 2 of this thesis describes the computational methods employed in this study, namely quantum chemical calculations to obtain activation barriers for the elementary reaction steps in the SMR reaction and microkinetic modeling to predict macroscopic reaction rate and surface coverage as well as to identify the rate controlling steps. Chapter 3 investigates (oxygen-assisted) activation of water on two Rh surfaces, i.e. planar Rh(111) and stepped Rh(211) surfaces. In Chapter 4 of this thesis the recombination to CO is investigated. Besides direct recombination of adsorbed C and O , the recombination of CH and O and C and OH are also considered. The various mechanisms are again compared for the planar Rh(111) and the conjugated Rh(211) surface. Chapter 5 gives the results of an extensive study of the full dissociation of methane to atomic carbon on the planar Rh(111) and the conjugated Rh(211) surface as well as on two types of sites of a Rh nanowire model, representing terrace and

edge sites on small Rh nanoparticles. Chapter 6 introduces a microkinetic model that aims to obtain the reaction rate of the SMR reaction based on the reaction energy parameters computed for each of the elementary reaction steps on the planar and stepped surfaces. An analysis of the structure dependence will be presented as well.

1.6. References

- [1] S. Anderson, R. Newell, *Annu. Rev. Environ. Resour.*, 29 (2004) 109.
- [2] K.Z. House, C.F. Harvey, M.J. Aziz, D.P. Schrag, *Energy Environ. Sci.*, 2 (2009) 193.
- [3] I. Chorkendorff, J.W. Niemantsverdriet, *Concepts of Modern Catalysis And Kinetics*, Wiley-VCH, Weinheim, Germany, 2003.
- [4] M. Boudart, *Top. Catal.* 1 (1994) 405.
- [5] N. MacDowell, N. Florin, A. Buchard, J. Hallett, A. Galindo, G. Jackson, C.S. Adjiman, C.K. Williams, N. Shah, P. Fennell, *Energy Environ. Sci.*, 3 (2010) 1645.
- [6] W.W. Irion, O.S. Neuwirth, *Oil Refining*; Wiley: Weinheim, Germany, 2005, 1.
- [7] H. Topsøe, B.S. Clausen, F.E. Massoth, *Hydrotreating Catalysis, Science and Technology*; Springer: Berlin, Germany, 1996.
- [8] J.R. Rostrup-Nielsen, *Steam Reforming Catalysts*; Danish Technical Press: Copenhagen, Denmark, 1975, 17.
- [9] J. Sehested, *Catal. Today* 111 (2006) 104.
- [10] J.R. Rostrup-Nielsen, J.H. Bak Hansen, *J. Catal.* 144 (1993) 40.
- [11] D. Qin, J. Lapszewicz, *Catal. Today* 21 (1994) 552.
- [12] G. Jones, J.G. Jakobsen, S.S. Shim, J. Kleis, M.P. Andersson, J. Rossmeisl, F. Abild-Pedersen, T. Bligaard, S. Helveg, B. Hinnemann, J.R. Rostrup-Nielsen, I. Chorkendorff, J. Sehested, J.K. Nørskov, *J. Catal.* 259 (2008) 147.
- [13] H.M. Kvamsdal, K. Jordal and O. Bolland, *Energy* 32 (2007) 10.
- [14] J.A.Z. Pieterse, J. Boon, Y.C. van Delft, J.W. Dijkstra and R.W. van den Brink, *Catal. Today* 156 (2010) 153.
- [15] D.A.J.M. Ligthart, J.A.Z. Pieterse, E.J.M. Hensen, *Applied Catalysis A: General*, 405 (2011) 108.
- [16] J.M. Wei, E. Iglesia, *J. Phys. Chem. B*, 108 (2004) 4094.
- [17] J.R. Rostrup-Nielsen, J.-H. Bak Hansen, *J. Catal.*, 144 (1993) 38.
- [18] J.M. Wei, E. Iglesia, *Angew. Chem., Int. Ed.*, 43 (2004) 3685.
- [19] J.M. Wei, E. Iglesia, *J. Phys. Chem. B*, 108 (2004) 7253.
- [20] J.M. Wei, E. Iglesia, *J. Catal.*, 225 (2004) 116.
- [21] J.M. Wei, *Phys. Chem. Chem. Phys.*, 6 (13) (2004) 3754.
- [22] E. Shustorovich, *Surface Science*, 176 (1986) L863.

- [23] R.A. van Santen, M. Neurock, *Molecular heterogeneous catalysis: a conceptual and computational approach*, Wiley-VCH, Weinheim, Germany, 2006.
- [24] R.A. van Santen, *Acc. Chem. Res.* 42 (2009) 57.
- [25] R.A. van Santen, J.W. Niemantsverdriet, *Chemical Kinetics and Catalysis*, Springer Science, New York, USA, 1995.
- [26] Z.-P. Liu, P. Hu, *J. Am. Chem. Soc.*, 125 (2003) 1958.
- [27] T. Zambelli, J. Winterlin, J. Trost and G. Ertl, *Science* 273 (1996) 1688.
- [28] K. Honkala, A. Hellman, I. N. Remediakis, A. Logadottir, A. Carlsson, S. Dahl, C.H. Christensen, J.K Nørskov, *Science* 307 (2005) 555.

Chapter 2:

Computational Methods

Computer simulations are extremely useful in catalysis research because of they allow to predict the surface structure, physisorption and chemisorption of atoms and molecules on surface sites, lateral interactions between surface intermediates and activation barriers and reaction energies for the elementary surface reactions. A major goal is to predict the macroscopic reactivity of a catalytic reaction, which requires following the dynamics of the surface and the adlayer as a function of process conditions including temperature, pressure and concentrations. To do so, one needs to simulate all relevant elementary processes including adsorption, surface reaction, diffusion and desorption that make up the catalytic cycle and ideally also the structure and composition of the catalytic surface. The kinetics for catalytic systems can be modeled by deterministic kinetics based on continuum concentrations in the gas or liquid and the adsorbed phases or via stochastic kinetics [1]. Detailed knowledge about the reaction mechanism is a prerequisite. These methods also require sufficiently accurate rate constants for the elementary reactions steps that make up the mechanism. Such information is typically obtained by electronic structure calculations. A characteristic timescale of a reaction catalyzed by a heterogeneous catalyst is 1 s. This is to be compared with the time scale of a molecular frequency of 10^{-12} s or that of electronic motion of 10^{-16} s. Elementary reaction steps on the surface are usually occurring at a timescale of 10^{-6} s. [2] The overall rate of a catalytic reaction depends on phenomena that occur at very different length and time scales. As a result a comprehensive theoretical description of a catalytic process necessitates a complementary utilization of a wide range of computational techniques. This is illustrated in Figure 1. It is necessary to decouple simulations of the long time-scale phenomena. This approach is followed here. First, ab initio calculations are carried out to construct a database of rate constants and energetics of the elementary reaction steps relevant to steam methane reforming. Another goal of such

electronic structure simulations is to decide which reaction pathway is the most likely one. These calculations can also be carried out as a function of the topology of the catalytic surface to investigate the structure sensitivity of the different elementary reaction steps. In this work, we will use density functional theory (DFT) as a method to compute the electronic structure and the energies related to the elementary reaction steps. Second, this set of parameters is used to predict surface coverage, reaction rates and so forth by simulating the reaction kinetics in the mean-field approximation taking into account explicitly all elementary reactions steps.

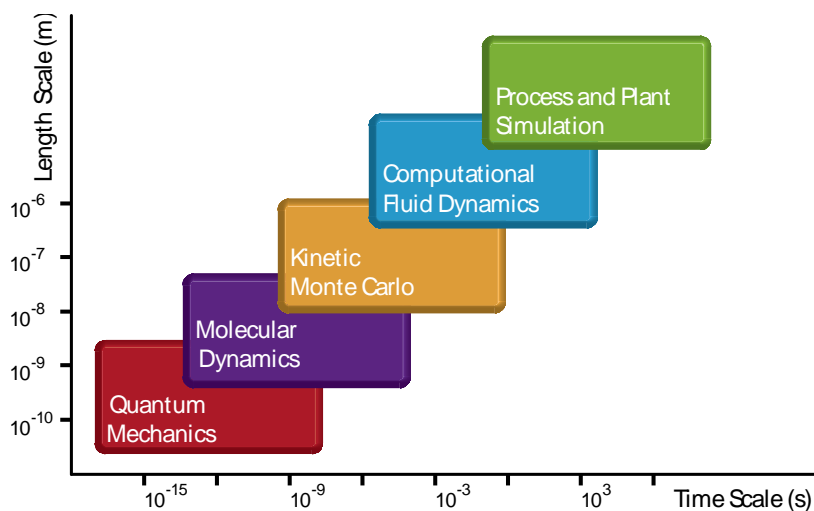


Figure 1. Computer simulations on different fields required specific time and length scales. The time scale decreases with smaller length scales. [2]

2.1. Microkinetic modeling

Microkinetic modeling is the modeling of reactions in terms of the elementary reaction steps that occur on the catalytic surface [3]. A requirement is that the reaction mechanism should be understood in sufficient detail. The temporal concentrations of the gas phase species and the surface intermediates can be followed by solving the set of differential equations that describe the rate of formation of each component. Such models define the rate on the basis of concentrations or partial pressures and surface coverage. A limitation of this mean-field approach is that it averages the intrinsic kinetics over the atomic structure. Thus, the exact features of the local structure and composition near the site where the catalytic reaction is occurring is neglected. The mean-field approach is reasonable if lateral interactions between surface intermediates are absent and fast diffusion maintains a state of ideal mixing. In the latter case, the kinetic parameters will be surface coverage independent. If lateral interaction should be incorporated, another method like kinetic Monte-Carlo [1], should be chosen.

Solving the differential equations gives the reaction rate. Employing these differential equations in a reactor model provides the possibility to follow the spatiotemporal changes of the reaction rate in a reactor. A very common assumption is to use steady-state kinetics, which implies that there is no temporal change in the concentrations of the intermediates.

The use of microkinetic models is particularly useful to obtain insight into the composition of the surface adlayer and the rates of the elementary reaction steps. Knowledge about the dependence of the reaction rate on surface composition can guide synthesis efforts. Parameters that are used as input for models are sticking coefficients, surface bond energies, pre-exponential factors for surface reactions, activation energies, surfaces bonding geometries and active site densities and ensemble sizes. Very often, experimental data have been used as input to microkinetic models. However, modern computational methods and increasing computing power make it possible to provide rate constants with reasonable accuracy. In the present case, the aim is to use ab initio data as input to a microkinetic model to simulate methane steam reforming.

We will use the Eyring's transition-state theory to compute reaction rates. In this formalism, a reaction scheme is assumed where the ground state of a reactant (R) is in equilibrium with the transition state (R^\ddagger). The overall rate is determined by the crossing of the barrier to product P.



The transition-state reaction rate constant (k^{TST}) is computed by

$$k^{TST} = \frac{k_B T}{h} \frac{Q_{R^\ddagger}}{Q_R} e^{-\frac{E_b}{k_B T}} \quad (2.1)$$

with k_B the Boltzmann's constant, T temperature, h Planck's constant, Q_{R^\ddagger} and Q_R the partition functions of the transition and ground state, respectively, and E_b is the barrier height. [4]

A condition for this equation to be valid is that the vibrational and rotational modes in the transition state are in equilibrium with the corresponding modes in the ground state. Thus, energy transfer between these modes should be fast compared to the reaction rate. This requirement is met for intramolecular reactions and most surface-mediated reactions.

The pre-exponential factor ν_{pre} and the activation barrier E_{act} are the kinetic parameters required to describe the rate of a reaction and can be deduced from the empirical Arrhenius rate expression via

$$k^{Arrh} = \nu_{pre} \cdot \frac{e^{-\frac{E_{act}}{k_B T}}}{k_B T} \quad (2.2)$$

The pre-exponential factor contains the entropic contributions

$$\nu_{pre} = \frac{k_B T}{h} \cdot \frac{Q_{R^\ddagger}}{Q_R} \quad (2.3)$$

The activation energy is defined as

$$E_{act} = E_b + \frac{1}{2} h \left(\sum_i \nu_i^\ddagger - \sum_i \nu_i^0 \right) + k_B T \quad (2.4)$$

The second term in this equation is due to the zero-point vibrational correction.

The partition functions are made up of the translational, rotational and vibrational contributions. In the calculation of the vibrational entropy of the transition state, the reaction coordinate itself is not included. The transition state is the saddle point on the potential energy surface along the reaction coordinate. [4]

In our work we have developed our own script in corporation with A.P.J. Jansen. This script is written in Matlab. The complete functioning of this tool is explained in Chapter 6.

2.2. Quantum chemical calculations

In current research, quantum chemical (QM) calculations are gaining more ground as a valuable tool to gain more insight in chemical properties and reactions, by predicting the structure, energy and properties of a many-electron system. QM calculations are used to determine the positions of electrons in the system. Based on the force they apply on each other and the nuclei, the structure of the system with the least energy can be determined. The exact electronic structure can only be determined for a limited number of cases. Three major field can be defined in QM calculations; *ab initio* wave-function based methods, like Hartree-Fock (HF) [5] and *ab initio* density functional (DFT), and semi-empirical methods. HF is not employed in our study, due to the challenges of HF when employed in periodic models. Semi-empirical methods are not included, because our system is well modeled using DFT,

without any additional modifications. These methods are typically used in systems where DFT has to be corrected to obtain realistic results, which would be the case when semiconductors like CeO_2 are studied. DFT itself is derived from first principles and lacks any assumptions.

Density function theory (DFT) is based on two theorems, namely the Hohenberg-Kohn [6] and Kohn-Sham [7] theorems. The Hohenberg and Kohn Theorem assumes that all observable quantities that can be calculated from the system's electron density can be derived from the system in its ground state. The ground state electron density, r_0 , of a many electron system in the presence of an external potential, V_{ext} , uniquely determines, except for a constant, the external potential (V_{ext}). This implies that all properties are a functional of the electron density. This theorem basically demonstrates the existence of a one-to-one mapping between the ground state electron density and the ground state wavefunction of a many-particle system.

The Kohn-Sham approximation is used to compute the energy from the N-electron density using a one-particle formalism. In this formalism, the ground state energy, kinetic energy, electron-electron interaction energy and energy of the electrons in the external potential are all functional of the electron density, and not exactly defined electron positions like in HF. One possible way to model the density is as a sum of squares of orbitals, which are in turn approximated by a specific orthonormal basis-set. The electronic structure of a system can be modeled by an infinite number of these basis functions. However, to limit the computational costs, a truncation is employed. A wide range of possible basis sets are available and should be chosen based on the system studied and the accuracy required. Plane-waves are a variation on these basis sets and are more applied in periodic modeling. Plane-waves are easily employed and typically faster than the use of basis-sets.

There are a vast amount of computational codes based on DFT available [8-12]. Based on the coordinates of a system, it is possible to calculate the energy of a given atom or molecule. The strength of most programs lies in the fact that they are able to search for a local minima on the energy surface, which corresponds to the relaxed state of a molecule or atom. The methods used to locate local minima are all based on some type of computed gradient application on the potential energy surface [13]. The reactant and product state of a given reaction are these local minima. To compute the activation energy for the reaction, a transition state has to be identified. The transition state is a saddle point of the potential

energy as a function of the positions of the nuclei. Computationally, the localization of a transition state (TS) is far more complex than finding an local minimum. The search methods for TS are evolved from the methods used to localize minima. Of the possible methods, the most commonly used in the field considered here are (climbing-images) Nudged Elastic Band [14] and Dimer [15] methods.

In our study the nudged elastic band (NEB) method is employed for identifying the transition state along a reaction coordinate. The method works by optimizing a number of intermediate images along the reaction path. For each image, the lowest energy is found, while maintaining equal spacing to neighboring images. This constrained optimization is done by adding spring forces along the band between images and by projecting out the component of the force due to the potential perpendicular to the band [14].

For refined calculations, the climbing image (CI-NEB) method is used. This method is a small modification to the NEB method in which the highest energy image is driven up to the saddle point. This image does not feel the spring forces along the band. Instead, the true force at this image along the tangent is inverted. In this way, the image tries to maximize its energy along the band, and minimize in all other directions. When this image converges, it will be at the exact saddle point.

In chapters 3-5, the computational setup used in the respective researches are explained for each individual case. In this work the Vienna Ab-Initio Simulation Package (VASP) [11,12] is used to perform these calculations.

2.3. References

- [1] A.P.J. Jansen, arXiv:cond-mat/0303028v1.
- [2] P. Atkins, J. de Paula, Atkins' Physical Chemistry, 8th ed., Oxford University Press, Oxford, UK, 2006.
- [3] J.A. Dumesic, B.A. Milligan, L.A. Greppi, V.R. Balse, K.T. Sarnowski, C.E. Beall, T. Kataoka, D.F. Rudd, Ind. Eng. Chem. Res., 26 (1987) 1399.
- [4] J.A. Dumesic, D.F. Rudd, L.M. Aparicio, J.E. Rekoske, A.A. Treviño, The Microkinetics of Heterogeneous Catalysis, ACS, Washington, USA, 1993.
- [5] V. Fock, Zeitschrift fur Physik, 61 (1930) 126.
- [6] P. Hohenberg, W. Kohn, Phys. Rev., 136 (1964) 864.
- [7] W. Kohn, L.J. Sham, Phys. Rev., 140 (1965) 1133.

- [8] B. Delley, *J. Chem. Phys.*, 113 (2000) 7756.
- [9] M.D. Segall, P.L.D. Lindan, M.J. Probert, C.J. Pickard, P.J. Hasnip, S.J. Clark, M.C. Payne, *J. Phys. Cond. Matt.* 14 (2002) 2717.
- [10] W. Andreoni, A. Curioni, *Parallel. Comput.* 26 (2000) 819.
- [11] G. Kresse, J. Furthmüller, *Comput. Mater. Sci.* 6 (1996) 15.
- [12] G. Kresse, J. Furthmüller, *Phys. Rev. B* 54 (1996) 11169.
- [13] W.H. Press, B.P. Flannery, S.A. Teukolsky, W.T. Vetterling, *Numerical Recipes* (Cambridge University Press, New York, (1986).
- [14] G. Henkelman, B.P. Uberuaga, H. Jónsson, *J. Chem. Phys.* 113 (2000) 9901.
- [15] G. Henkelman and H. Jónsson, *J. Chem. Phys.* 111 (1999) 7010.

Chapter 3: DFT study on H₂O activation by stepped and planar Rh surfaces¹

In this work the effect of surface steps and pre-adsorbed oxygen on the activation energy of water dissociation is studied for Rh with DFT modeling. Without oxygen, water activation is found to be structure insensitive. In the presence of oxygen adatoms, the barrier for H₂O dissociation will decrease significantly because adsorbed oxygen acts as a proton acceptor.

3.1. Introduction

Synthesis gas and hydrogen are produced amongst others from natural gas [1]. Synthesis gas is a versatile platform to a wide range of fuels and chemicals. Pure hydrogen is currently an essential intermediate chemical in petroleum refineries to produce clean transportation fuels [2,3]. It is expected to become even more important with serious applications in the emerging hydrogen economy. Hydrogen is mainly produced by steam reforming of natural gas [1,4–6].

The most frequently used metal for steam methane reforming (SMR) catalysts is nickel [1,7]. In most commercial applications, noble metal additives and other promoters are used. Besides nickel, a number of precious metals such as Rh, Ru, Pt and Pd display high activity [8–13], but their use is often not economically viable. Rhodium is one of the most active metals for

¹ This chapter has been published as “DFT study on H₂O activation by stepped and planar Rh surfaces” by Pieter W. van Grootel, Emiel J.M. Hensen and Rutger A. van Santen in *Surface Science* 603 (2009) 3275–3281

the reforming of natural gas, which is particularly interesting for the reforming of hydrocarbons at relatively low temperatures [9,14].

The candidate rate limiting steps for steam methane reforming are generally considered to be dissociative methane adsorption and the recombination of C and O to carbon monoxide [1,15,16]. These elementary reaction steps have been studied for a wide range of transition metals [1,8–14,16–24]. Recent works indicate a strong dependence of the rate of the methane dissociation on the coordinative saturation of the surface metal atoms [16–18,23,24]. Methane dissociation proceeds over a single surface metal atom [16–18,23,24]. In essence, the higher the coordinative unsaturation of the surface atoms (corner > step > planar), the lower the barrier for C–H bond cleavage to dissociate methane to adsorbed CH₃ and H [16–18,25]. Dissociation of adsorbed CO involves more than one surface atom. A stepped surface site is more reactive towards CO dissociation than a planar surface, because in the former case the C and O atoms are not shared by the same surface atom in the transition state [16,19,20]. In addition to the two mentioned reactions, water activation could be an additional likely candidate for the rate determining step. Activation of water is not only relevant to the steam reforming of methane but also to the water–gas shift reaction.

In contrast to methane activation and CO formation, a relatively small number of works has been devoted to the study of water activation by metals. Gong *et al.* [26] have reported calculations on the formation of water from adsorbed OH and H on planar and stepped cobalt surfaces. The barrier on Co(111) is 20 kJ/mol higher than the barrier on a stepped surface (135 kJ/mol). Grecea *et al.* [27] investigated the dissociation of water on Pt surfaces experimentally, but were not able to conclude whether the presence of steps promotes water dissociation. A comparison for copper surfaces can be made on the basis of works by Tang and Chen [28] and Gokhale *et al.* [29]. The former reports a barrier for water formation from OH and H of 60 kJ/mol for the more open Cu(110) surface. This value is about half the value computed for the Cu(111) surface as reported by Gokhale *et al.* In the presence of adsorbed oxygen atoms (O_{ads}), the differences in these energy barriers become considerably smaller. Wang *et al.* [30] have reported a substantial lowering of the barrier for water dissociation in the presence of O_{ads} for a variety of metals. Importantly, they concluded that the substantial differences in barriers between these metals tend to become smaller when water dissociation involves O_{ads}.

Herein we investigate the role of the surface geometry and coordination (stepped surfaces vs. planar surfaces) and of co-adsorbed oxygen on the dissociation of water on rhodium. Based on the results and literature values, we will analyze the periodic trends of transition metals for water dissociation. Finally, we will discuss the relevance of water dissociation for steam methane reforming.

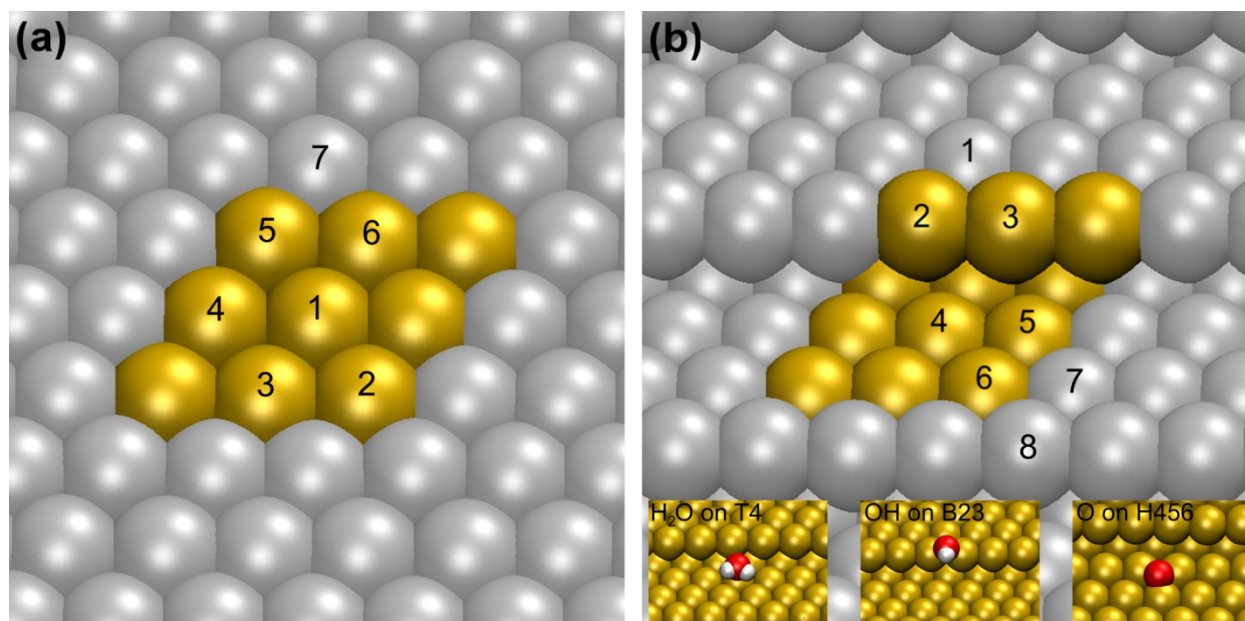


Figure 1. The two Rh surfaces investigated in this study: a planar Rh(111) surface (a) and a stepped Rh(221) surface (b). The unit cell is highlighted in yellow. The surface atoms on both surfaces are numbered to denote the various adsorption sites.

3.2. Methods

The models for Rh(111) and Rh(221) with a (110) step are shown in Figure 1. The former model consists of a $p(3 \times 3)$ unit cell consisting of five layers of Rh atoms in a fcc layering and separated by vacuum (10 Å). The resulting surface consists of close packed atoms. The layering gives rise to two kind of hollow sites, a hcp hollow site having a neighbouring Rh atom directly located in the subsurface second layer and a fcc hollow site where a subjacent atom is absent. The supercell consists of 45 Rh atoms. The coordination number of the surface Rh atoms is 9. Four symmetric adsorption sites can be distinguished on the planar surface. Besides the two threefold hollow sites (hcp and fcc), the surface contains top and bridged sites.

The Rh(221) surface contains (111) terraces and (110) oriented monoatomic step. The geometry of the terrace is the same as for the planar Rh(111) surface. The number of layers in this model is five and the super cell contains 51 rhodium atoms. The coordination number of

the terrace and step edge surface atoms is 9 and 7, respectively. The coordination number of the atoms at the bottom of the step is 11. The stepped surface introduces a higher number of potential adsorption sites. There are fourteen sites of interest, which are denoted in Figure 1b. The notations adopted in Table 2, is H for hollow, B for bridged and T for top adsorption. Three adsorption modes are shown in Figure 1b to illustrate this.

Next to the (221) surface with the (110) step, it is also possible to make a (100) step, resulting in the (211) surface. The activation energy of water dissociation has also been computed for this surface and was found to be similar (63 kJ/mol for Rh(221) and 67 kJ/mol for Rh(211)). Such differences are within the error (10–15 kJ/mol) of the calculation method chosen [31].

The vacuum space above the slab models was chosen 10 Å, because energy differences for large separation of the slabs were found to be negligible. The top three layers of the supercells were allowed to relax during energy optimizations and no symmetry restrictions were imposed.

Prior to the investigation of the energy barriers for the activation of water, the most favourable adsorption sites for the relevant species (H₂O, OH, O and H) were determined. The reaction pathway analysis was carried out from the most stable adsorption geometries of the participating molecules and atoms.

Adsorption energies (ΔE_{ads}) were calculated from the energy difference between the surface containing the geometry optimized adsorbate ($E_{\text{surface-adsorbate}}$) and the same surface with the adsorbing molecule placed in the middle of the vacuum between two slab surfaces ($E_{\text{surface + adsorbing molecule}}$):

$$\Delta E_{\text{ads}} = E_{\text{surface-adsorbate}} - E_{\text{surface + adsorbing molecule}} \quad (3.1)$$

This approach has been evaluated against the alternative method where the adsorbing molecule is placed in a large super cell without Rh. There was no significant difference between these two approaches to calculate the adsorption energy.

The quantum-chemical calculations were carried out using the Vienna Ab Initio Simulation Package (VASP) [32,33] using the gradient-corrected PW91 exchange-correlation functional [34]. The projected-augmented wave (PAW) method [35,36] was used to describe electron–ion interactions, and for valence electrons a plane wave basis set was employed. The energy cut-off was set to 400 eV. Computations were performed with $3 \times 3 \times 1$ k -point sampling of the Brillouin zone (11 k -points) [37]. The third vector is perpendicular to the surface. The

relaxation of the electronic degrees of freedom was assumed to be converged, if the total energy change and the band structure energy change between two steps were both smaller than 10^{-3} eV. An energy difference between two steps of less than 10^{-2} eV was used as the criterion for convergence of ionic relaxation. The influence of spin polarization has been studied and has been corrected for by the software used. The choices for the number of k-points, the plane-wave cut-off energy and the size of the vacuum are generally accepted values in the field of work.

For determining the transition state of reaction pathways, the Climbing Image Nudged Elastic Band-method (CI-NEB) [38] was employed. A typical calculation to search for a transition state embodies three or four CI-NEB calculations with eight images, which are constrained by a spring force of $5 \text{ eV}/\text{\AA}^2$. The initial, final and transition state geometries obtained were tested by analyzing the calculated harmonic normal modes, which were calculated using the finite difference method as implemented in VASP. Small displacements (0.02 \AA) of adsorbed atoms and the three relaxed surface layers were used for the estimation of numerical Hessian matrix. Energies were corrected for the zero point energy.

To ascertain the appropriateness of our models, we recomputed the barriers of two transition states based on the geometries provided by the authors of Ref. [30]. Our values for water dissociation on a planar surface, Rh(111) in the presence (68 kJ/mol) or absence (91 kJ/mol) of co-adsorbed O corresponds well to the values of Wang *et al.*, i.e. 58 and 104 kJ/mol, respectively.

3.3. Results

3.3.1. OH_x and H adsorption properties

The adsorption energies of OH_x and H species on Rh(111) and Rh(211) are presented in Tables 1 and 2, respectively. We studied the upright adsorption geometry of OH, while for water two adsorption geometries were included, i.e. the one parallel and the one perpendicular to the surface.

Before discussing in detail the results, we note that the computed adsorption energies of species adsorbed on equivalent sites of both surfaces, for instance H₂O on T1 of Rh(221) (-37 kJ/mol) and on top of Rh on Rh(111) (-39 kJ/mol), are similar.

Table 1. Adsorption energies for OH_x and H species on Rh(111) in kJ/mol relative to the corresponding species in vacuum and relevant literature values. The bold values indicate the most stable adsorption site for the respective species.

	H ₂ O	OH	O	H	Reference
fcc	-8a, -12b	-312	-586	-276	-
	-11	-282	n.a. ^c	-268	[39]
	0	-332	-532	-272	[40]
hcp	-7 ^a , -10 ^b	-293	-585	-274	-
	-11	-305	n.a. ^c	-266	[39]
	n.a. ^c	-306	-523	-268	[40]
top	-30 ^a , -39^b	-219	-445	-239	-
	-34	-201	n.a. ^c	-241	[39]
	-33	n.a. ^c	n.a. ^c	-230	[40]
bridge	-13 ^a , -17 ^b	-284	-540	-264	-
	-21	-287	n.a. ^c	-258	[39]
	-21	-293	-469	-255	[40]

^a Water molecule perpendicular to the surface.

^b Water molecule parallel to the surface.

^c Not available.

Table 2. Adsorption energies for OH_x and H species on Rh(221) in kJ/mol relative to the corresponding species in vacuum and relevant literature values. The bold values indicate the most stable adsorption site for the respective species. The adsorption sites are denoted by T (top), B (bridge) and H (hollow) with the numbers referring to the sites given in Figure 1b.

	H ₂ O	OH	O	H
T1	-37	-202	-506	-253
T2	-61	-293	-439	-246
T4	-33	n.a. ^a	n.a. ^a	n.a. ^a
B12	-25	-298	n.a. ^a	n.a. ^a
B23	-25	-332	-601	-286
B24	-70	-286	-533	-269
B45	-16	-276	-521	-272
B46	-21	n.a. ^a	-531	-276
H123	n.a. ^a	-315	-600	-288
H2345	n.a. ^a	-297	-547	-278
H456	-19	-266	-569	-284

^a No local minimum found.

The most favourable adsorption site for H₂O is the top site. Parallel adsorption (OH bonds parallel to the surface) is slightly more favourable than upright adsorption with the OH bonds pointing away from the surface. For OH, O and H species, the threefold hollow site is the preferred site. The values for adsorption of O and H on fcc and hcp sites are very similar (-586 vs. -585 kJ/mol, and -276 vs. -274 kJ/mol). The adsorption energies follow the trends

reported in earlier works [39,40] well. The biggest discrepancy can be found for the O adsorption, which can be attributed to the different functional and the width of the slab chosen. The corresponding geometries (Table 3) also agree well with those given in literature [41].

On the stepped Rh(221) surface, water adsorption on T2 and B24 sites (geometries are shown in Table 5) are the most favourable. Adsorption on B24 is slightly more favourable than adsorption on T2, because the hydrogen atoms point towards the terrace below the stepped surface in the former case. The adsorption geometries are very similar with the oxygen atom being adsorbed on the Rh atom at the top of the edge. This is reasonable because this Rh atom has the lowest coordination number. The geometry of the adsorption on the step corresponds to the geometry reported previously on stepped Co [26]. The B24 adsorption mode was chosen for the calculation of water dissociation on the stepped surface.

Concerning adsorption of OH and O, the most favourable site is the bridge position between two atoms of the step (B23) and the threefold hollow site (H123) behind this site. Hydrogen preferentially adsorbs in high coordination hollow and bridge sites. The adsorption energies between the various hollow and bridged sites are very similar.

Table 3. Geometrical parameters of water dissociation on Rh(111). The atom numbers refer to the numbers used in Figure 1a. Bond lengths (r) are given in Å, angles (θ) and dihedrals (φ) in degrees.

	Initial	Transition state	Final
r(Rh1 – O1)	2.28	2.08	2.17
r(Rh2 – O1)	n.a. ^a	n.a. ^a	2.16
r(Rh3 – O1)	n.a. ^a	n.a. ^a	2.18
r(Rh1 – H2)	n.a. ^a	2.11	1.85
r(Rh4 – H2)	n.a. ^a	2.06	1.89
r(Rh5 – H2)	n.a. ^a	1.82	1.86
r(O1 – H1)	1	1	0.99
r(O1 – H2)	1	1.56	2.9
θ (Rh1 – O1 – H1)	102.6	108.1	126.6
θ (Rh2 – O1 – H1)	n.a. ^a	n.a. ^a	132.1
θ (Rh3 – O1 – H1)	n.a. ^a	n.a. ^a	130
θ (Rh1 – O1 – H2)	102.8	68.5	n.a. ^a
θ (H1 – O1 – H2)	107.5	105.2	n.a. ^a
φ (Rh3 – Rh1 – O1 – H1)	106.1	104.1	n.a. ^a
φ (Rh3 – Rh1 – O1 – H2)	-142.3	-156.2	n.a. ^a

^a Value is not available or not applicable.

3.3.2. Dissociation of water

Based on these results, the dissociation of water was investigated on clean surfaces of Rh(111) and Rh(221) and these surfaces with pre-adsorbed oxygen atoms. The resulting reaction pathways and the calculated energies are shown in Figures 2 and 3, respectively. The geometrical parameters for each of the mechanisms can be found in Tables 3–6.

Table 4. Geometrical parameters of oxygen-assisted water dissociation on Rh(111). The atom numbers refer to the numbers used in Figure 1a. Bond lengths (r) are given in Å, angles (θ) and dihedrals (φ) in degrees.

	Initial	Transition state	Final
$r(\text{Rh1} - \text{O1})$	2.26	2.03	2.18
$r(\text{Rh2} - \text{O1})$	n.a. ^a	3.22	2.17
$r(\text{Rh3} - \text{O1})$	n.a. ^a	2.73	2.18
$r(\text{Rh5} - \text{O2})$	2.03	2.11	2.18
$r(\text{Rh6} - \text{O2})$	2.03	2.12	2.19
$r(\text{Rh7} - \text{O2})$	2.04	2.91	2.18
$r(\text{O1} - \text{H1})$	1	1	0.99
$r(\text{O1} - \text{H2})$	1	2.28	n.a. ^a
$r(\text{O2} - \text{H2})$	2.5	1.01	0.99
$\theta(\text{Rh1} - \text{O1} - \text{H1})$	101	110.1	132.8
$\theta(\text{Rh2} - \text{O1} - \text{H1})$	n.a. ^a	61.8	130.4
$\theta(\text{Rh3} - \text{O1} - \text{H1})$	n.a. ^a	105	131.8
$\theta(\text{Rh1} - \text{O2} - \text{H2})$	102.5	77.6	n.a. ^a
$\theta(\text{Rh5} - \text{O2} - \text{H2})$	n.a. ^a	105.3	129.6
$\theta(\text{Rh6} - \text{O2} - \text{H2})$	n.a. ^a	108.5	130.9
$\theta(\text{Rh7} - \text{O2} - \text{H2})$	n.a. ^a	171	129.7
$\theta(\text{H1} - \text{O1} - \text{H2})$	106.7	107.1	n.a. ^a
$\varphi(\text{Rh3} - \text{Rh1} - \text{O1} - \text{H1})$	-138.1	n.a. ^a	n.a. ^a
$\varphi(\text{Rh3} - \text{Rh1} - \text{O1} - \text{H2})$	111.9	n.a. ^a	n.a. ^a

^a Value is not available or not applicable.

In the transition state for the dissociation of water on Rh(111), one hydroxyl bond has rotated upwards, while the other one has stretched towards the bridged site adjacent to the initial adsorption site. Upon cleavage of the OH bond, the OH and H fragments move to adjacent fcc sites. The barrier for dissociation is computed to be 63 kJ/mol (Figure 3). We compare this dissociation pathway with the one where there is pre-adsorbed oxygen on the Rh(111) surface. The initial geometry contains water on a top site with the oxygen atom adsorbed in a proximate fcc site. Dissociation involves the translation of the oxygen atom to the bridge position in the direction of the water adsorbate. In the transition state, one of the hydrogen atoms of the water molecule is accepted by the oxygen atom. The resulting OH species

migrates back to the fcc site and the remaining OH fragment moves to a next fcc site. The activation barrier is 53 kJ/mol, which is slightly lower than the value computed for the pathway without oxygen.

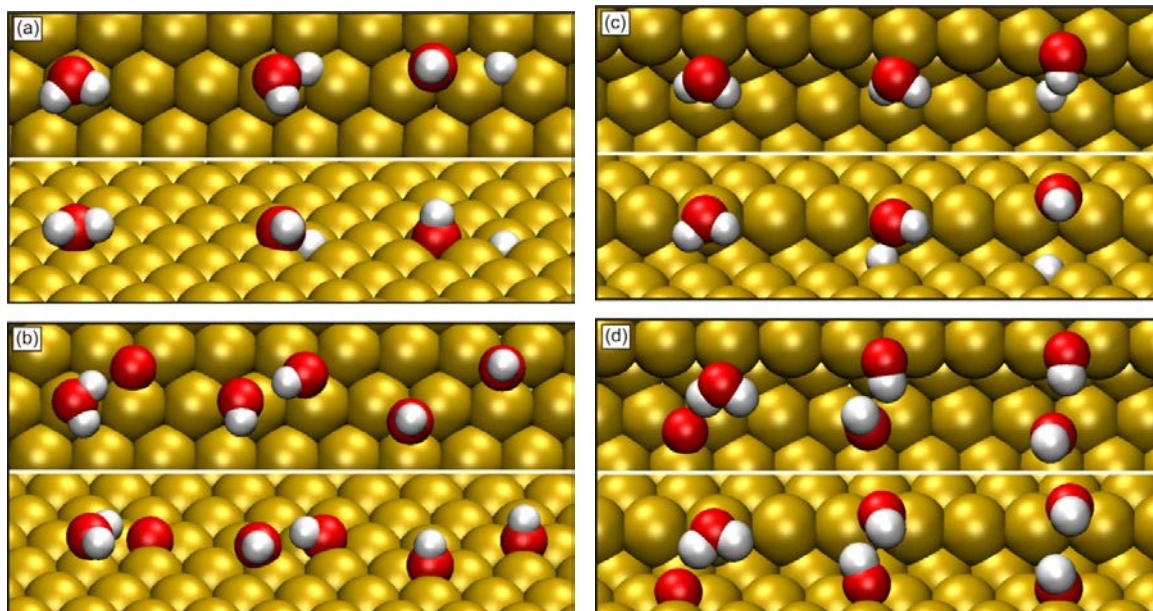


Figure 2. Dissociation of water on Rh(111) (a and b) and Rh(221) (c and d). Clean (a and c) and oxygen-containing (b and d) surfaces are depicted with oxygen and hydrogen atoms in red and white, respectively. Shown are the initial state (left), transition state (middle) and final state (right); both the top view (top) and side view (bottom) are given.

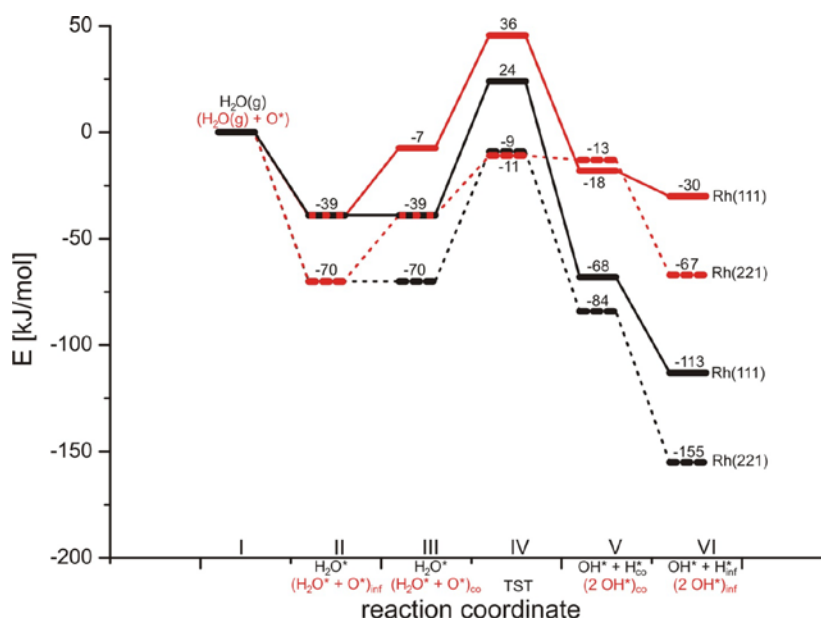


Figure 3. Reaction energy diagram of the dissociation of water over planar (full line) and stepped (dashed line) rhodium surfaces and the influence of pre-adsorbed oxygen (energies in kJ/mol). Black (red) lines without (with) pre-adsorbed oxygen. All energies are reported compared to the energy of the desorbed water (state I). The states II and VI are the energies without lateral interactions, i.e. with the adsorbates H₂O and O, OH and H or OH and OH at infinite distance.

Figure 2c depicts the pathway for the dissociation of H₂O on the stepped Rh(221) surface. In the initial state, the two OH bonds point downward with one H atom being closer to the lower lying terrace than the other. In the transition state, the former H atoms is close to the threefold hollow site on the terrace (H456), whilst the remaining OH moves toward the bridge of the two step atoms (B23). This pathway has a barrier of 61 kJ/mol. Dissociation of water on the Rh(221) surface with pre-adsorbed oxygen was computed starting from a geometry with water adsorption on the B24 site and oxygen adsorbed in a threefold hollow site on the lower lying terrace (H456). In the transition state, the H atom is transferred to this oxygen atom. The remaining OH fragment moves to the bridge site. The activation energy of water dissociation is only 28 kJ/mol for this case. In the final state, the OH fragment below the stepped site is located in the threefold hollow site (H456) and the other OH fragment in a bridged position (B23) on the top of the step.

Table 5. Geometrical parameters of water dissociation on Rh(221) surfaces for the two most favourable adsorption sites (T2 and B24). The atom numbers refer to the numbers used in Figure 1b. Bond lengths (r) are given in Å, angles (θ) and dihedrals (φ) in degrees.

	Initial (B24)	Initial (T2)	Transition state	Final
r(Rh2 – O2)	2.28	2.23	2.01	2.11
r(Rh3 – O2)	3.43	3.45	3.19	2.09
r(Rh6 – H1)	n.a. ^a	n.a. ^a	1.68	1.85
r(Rh7 – H1)	n.a. ^a	n.a. ^a	n.a. ^a	1.86
r(O2 – H1)	1.00	1.00	1.73	3.29
r(O2 – H2)	1.00	0.99	1.00	1.00
θ (Rh2 – O2 – H1)	98.2	104.9	88.7	n.a. ^a
θ (Rh2 – O2 – H2)	108.4	116.9	111.1	112.9
θ (Rh3 – O2 – H2)	n.a. ^a	n.a. ^a	n.a. ^a	112.2
θ (H1 – O2 – H2)	104.5	108.7	98.4	n.a. ^a
θ (Rh8 – Rh6 – H1)	n.a. ^a	n.a. ^a	n.a. ^a	85.1
θ (Rh8 – Rh7 – H1)	n.a. ^a	n.a. ^a	n.a. ^a	89.0
θ (Rh6 – H1 – O2)	n.a. ^a	n.a. ^a	150.8	n.a. ^a
φ (Rh1 – Rh2 – O2 – H1)	-82.1	-26.1	-101.5	n.a. ^a
φ (Rh1 – Rh2 – O2 – H2)	169.5	94.4	160	-164.7
φ (Rh2 – Rh3 – O2 – H2)	n.a. ^a	n.a. ^a	n.a. ^a	161.8

^a Value is not available or not applicable.

3.4. Discussion

Our study shows that the dissociation of H₂O on Rh(111) has a barrier of 63 kJ/mol, which is considerably lower than the value of 104 kJ/mol which was earlier reported by Wang *et al.* [30]. The difference in energy barriers relates to a difference in the reaction pathway.

Whereas the dissociation of water starts from the configuration with water on its initial top position in the present study, the pathway identified by Wang *et al.* [30] involved the diffusion of water from the top site to the adjacent bridge position. This latter step is uphill in energy (-10 kJ/mol) and is followed by the elongation of the OH bond over one of the Rh atoms, after which the dissociation follows a similar reaction pathway. This turns out to be less favourable than the dissociation of the OH bond in such way that the H atom ends up in a threefold hollow site. Indeed, our pathway has also been shown to be the preferred one for dissociation of water on a Ru(0001) [42] and Pd(111) surface [43].

Table 6. Geometrical parameters of the oxygen-assisted water dissociation on Rh(221) surfaces. The atom numbers refer to the numbers used in Figure 1b. Bond lengths (r) are given in Å, angles (θ) and dihedrals (φ) in degrees.

	Initial	Transition state	Final
r(Rh2 – O2)	2.26	3.02	2.10
r(Rh3 – O2)	3.42	2.09	2.09
r(Rh6 – O1)	2.05	2.04	2.37
r(Rh7 – O1)	2.02	2.07	2.23
r(Rh8 – O1)	2.06	2.70	2.12
r(O1 – H1)	2.17	1.20	1.00
r(O2 – H1)	1.00	1.26	n.a. ^a
r(O2 – H2)	1.00	0.99	1.00
θ (Rh2 – O2 – H1)	106.7	113.5	n.a. ^a
θ (Rh2 – O2 – H2)	107.0	112.3	112.9
θ (Rh3 – O2 – H2)	n.a. ^a	171.3	112.5
θ (Rh6 – O1 – H1)	n.a. ^a	101.0	148.6
θ (Rh7 – O1 – H1)	n.a. ^a	131.1	135.0
θ (Rh8 – O1 – H1)	n.a. ^a	162.4	113.6
θ (H1 – O2 – H2)	104.4	108.3	n.a. ^a
φ (Rh1 – Rh2 – O2 – H1)	-80.5	-96.5	n.a. ^a
φ (Rh1 – Rh2 – O2 – H2)	168.2	140.2	-164.3
φ (Rh1 – Rh3 – O2 – H2)	n.a. ^a	n.a. ^a	162.3

^a Value is not available or not applicable.

The activation energy values for the dissociation of water on the stepped (221) and planar (111) surface are not significantly different. A similar result has also been reported for the dissociation of NH₃ on clean Pt surfaces [44]: the transition state energy does not depend on the coordinative unsaturation of surface atoms, i.e. (111), (100) or (211). We believe the absence of a strong influence of the surface geometry can be attributed to the fact that the metal–oxygen (metal–nitrogen) bond does not change substantially during the dissociation reaction from the adsorbed state. The influence of the stronger metal–oxygen (metal–nitrogen) bond energy with decreasing coordinative unsaturation of the surface metal atoms

on the OH (NH) bond energy is relatively small. When we consider the case of dissociative adsorption of methane, it has been shown that the activation barrier strongly decreases with decreasing coordination number of the surface metal atom [16,23,24]. The reason might be that crossing the transition barrier involves the cleavage of the C–H bond and the formation of a σ bond between the surface metal atom and the CH₃ fragment. The latter bond is stronger for coordinatively more unsaturated surface atoms and therefore decreases the barrier substantially. In essence, the bond between the dissociating molecule (H₂O, NH₃) and the metal surface is already present, as these molecules dissociate from the adsorbed state.

The barrier of H₂O dissociation promoted by O on Rh(111) is computed to be 53 kJ/mol. This value does not differ significantly from the 58 kJ/mol reported by Wang *et al.* [30]. But in our study we found a difference in the reaction mechanism. Wang *et al.* included the diffusion of the oxygen adatom from one hollow position to the other. As shown in Figure 2b, dissociation of water in the present study starts from the initial adsorbed state, where one OH bond is stretched. This corresponds to the reaction pathway found for water dissociation on the clean surface. The preferred pathway for water dissociation is the one over the Rh(221) surface in the presence of oxygen. The much lower value of the activation energy of 28 kJ/mol compared to the other cases studied here demands an explanation. Firstly, for dissociation on the planar surface the oxygen that accepts the H atom has to move towards an energetically less favourable bridge site, whereas in the case of the stepped surface the oxygen adatom in the H456 does not need to migrate. The latter pathway is the preferred one. The difference in energy between a threefold hollow site and a bridge site on Rh(111) is 45 kJ/mol (Table 1). The difference in the barrier is, however, only 25 kJ/mol, which is reasonable since the oxygen adatom does not have to diffuse completely to the bridge position. Secondly, the O–H bond is stronger than the Rh–H bond. This implies that the cost for breaking an OH bond of water is compensated if a new OH bond is formed with an oxygen adatom. This compensation effect is much less pronounced in the case a Rh–H bond is formed. Finally, we should note that there is also an energy cost for diffusion of the oxygen adatom from the dominant terrace surface to the threefold hollow site (H456). When this energy difference of 31 kJ/mol is added to the activation energy, we find a barrier of 59 kJ/mol. This barrier is very close to the activation energies for the other situations.

Figure 4 plots the present set of activation energies and a number of computed activation energies for various other closed-packed transition metal surfaces taken from literature as a function of the metal–oxygen bond energy. For the reaction $\text{H}_2\text{O} \rightarrow \text{OH} + \text{H}$, we identify a

Brønsted–Evans–Polanyi type (BEP) relation ($E_{act} = \alpha \cdot \Delta E_O + \beta$) [45,46] with $\alpha = 0.35$. Here, we apply a combination of linear scaling relationships [47] and BEP relations, as is done in recent work [15]. To determine the nature of the transition state (early vs. late), we should however relate E_{act} to ΔE_{OH} . Taking into account the scaling properties for small H-containing molecules [47], we note that $\Delta E_{OHx} = \chi(x) \cdot \Delta E_O + \nu$ with $\chi = (x_{max} - x)/x_{max}$, where x_{max} is the maximum number of H atoms that can bond to the atom O ($x_{max} = 2$). With $x = 1$, a value of $\chi(1) = 0.5$ is predicted [47]. The resulting BEP parameter $\alpha = 0.7$ suggests that one is dealing with a transition state that is intermediate between early and late, with a slight bias for lateness [48]. Interestingly, the reacting OH bond has stretched by 50% in the transition state, which confirms the intermediate character found earlier. The transition states for H₂O dissociation by Rh(111) and Rh(221) are very similar in energy (61 vs. 63 kJ/mol) and geometry, since they take place over a single rhodium atom. This is also in line with the very small differences in the sum of the energies OH and H separately adsorbed in the final state with respect to the initial H₂O adsorption energies (Figure 3, 14 kJ/mol). For the surface oxygen-assisted dissociation of water, the energy barrier depends only weakly on the metal–oxygen (metal–hydroxyl) bond energy. The same holds for the reverse reaction. We attribute this finding to compensation effects: when one OH bond is cleaved, another one is formed; the cleavage of the OH bond becomes easier with increasing metal–hydroxyl bond strength, but concomitantly the formation of a new hydroxyl bond becomes less favourable.

Based on these results and those of Liu and Hu [16], we discuss the implications for methane steam reforming. As discussed above, the barrier for methane activation depends strongly on the surface geometry. Dissociation of methane takes place over one surface atom. The activation energy decreases from 65 to 31 kJ/mol when the coordination number of the surface atom decreases from 9 (planar surface) to 7 (stepped surface). The recombination of CO from adsorbed C and O proceeds with barriers of 178 and 114 kJ/mol on planar and stepped Rh surfaces, respectively. Nørskov and co-workers have found strong indications that the steam reforming of methane takes place on step sites of transition metal surfaces such as Rh [24]. When we assume that the step sites dominate the reactivity, the relevant activation energies to consider are 31, 114 and 60 kJ/mol for CH₄ dissociation, CO formation and H₂O dissociation, respectively. Related research [15] demonstrated that the reaction conditions are of importance on the rate of steam reforming. It was argued that the energy barrier for methane dissociation increases with respect to the reactant free energy difference, whereas the reverse holds for CO formation. In other words, with increasing temperature the rate

limiting step was argued to shift from CO recombination to methane activation. In our study we have concluded that H₂O dissociation has no sensitivity for surface unsaturation. When we take into account the activation of water, it may be argued that H₂O dissociation may become rate limiting at high temperatures, and has to be taken into account when studying steam methane reforming.

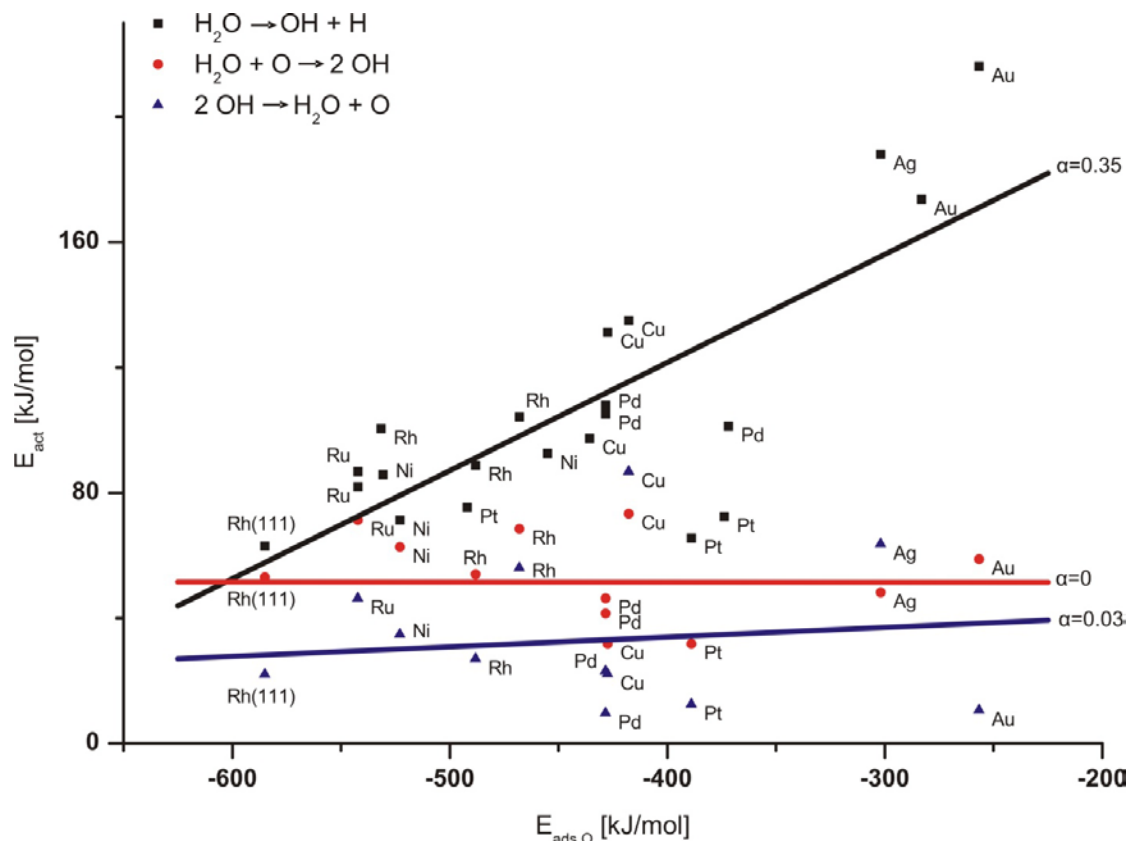


Figure 4. Dependence of the activation energies for the dissociation of water ($H_2O \rightarrow OH + H$, $H_2O + O \rightarrow 2 OH$) and the reverse reaction of the oxygen-assisted dissociation, i.e., the recombination of OH ($2 OH \rightarrow H_2O + O$) on the metal–oxygen bond strength for a large number of metal surfaces. Values are computed by quantum-chemical calculations, only on the closed packed surface of the metal, and taken from Refs. [29,30,40,49,50] and this work.

3.5. Conclusions

In this study, the dissociation of adsorbed water on planar and stepped surfaces of rhodium and the role of oxygen adatoms herein were investigated. The activation of water does not depend strongly on the coordination number of the surface metal atom: activation barriers for Rh(111) (63 kJ/mol) and Rh(221) (61 kJ/mol) for the oxygen-free case were very similar. This result is very different from the case of dissociative methane adsorption. The introduction of oxygen adatoms results in a significant decrease (53–28 kJ/mol) of the activation barrier as an H atom of water can be accepted by adsorbed O. Thus, the barriers of

around 60 kJ/mol for water dissociation on a clean Rh surface decrease to 28 kJ/mol on Rh(221) containing oxygen adatoms in the step. However, the substantial cost of diffusion of oxygen from the terrace sites to the step site has to be accounted for. As a result, we can conclude the energy barrier for dissociation does not depend strongly on the coordination number of the surface metal atom nor on the presence of oxygen adatoms. A Brønsted–Evans–Polanyi type plot of the activation barrier as a function of the metal–hydroxyl bond energy for a large number of transition metal surfaces shows that (i) the transition state is slightly biased towards a late character ($\alpha = 0.7$) and (ii) there are large compensation effects for the case of oxygen-assisted water dissociation.

3.6. Acknowledgements

This project has been carried out with financial support from SenterNovem. Super computing facilities were supported by the National Computational Facilities Foundation of the Netherlands Organization for Scientific Research (NWO-NCF).

3.7. References

- [1] J.R. Rostrup-Nielsen, J. Sehested, J.K. Nørskov, *Adv. Catal.* 47 (2002) 65.
- [2] W.W. Irion, O.S. Neuwirth, *Oil Refining*, Wiley, Weinheim, 2005, p. 1.
- [3] H. Topsøe, B.S. Clausen, F.E. Massoth, *Hydrotreating Catalysis*, Science and Technology, Springer, Berlin, 1996.
- [4] J.D. Holladay, J. Hu, D.L. King, Y. Wang, *Catal. Today* 139 (2009) 244.
- [5] R.M. Navarro, M.A. Peña, J.L.G. Fierro, *Chem. Rev.* 107 (2007) 3952.
- [6] PennWell Publishing Company, *Oil Gas J.* 90 (1992) 92.
- [7] C.H. Bartholomew, R.J. Farrauto, *Fundamentals of Industrial Catalytic Processes*, second ed., Wiley, USA, 2006.
- [8] J.M. Wei, E. Iglesia, *J. Phys. Chem. B* 108 (2004) 4094.
- [9] J.R. Rostrup-Nielsen, J.-H. Bak Hansen, *J. Catal.* 144 (1993) 38.
- [10] J.M. Wei, E. Iglesia, *Angew. Chem., Int. Ed.* 43 (2004) 3685.
- [11] J.M. Wei, E. Iglesia, *J. Phys. Chem. B* 108 (2004) 7253.
- [12] J.M. Wei, E. Iglesia, *J. Catal.* 225 (2004) 116.
- [13] J.M. Wei, *Phys. Chem. Chem. Phys.* 6 (13) (2004) 3754.
- [14] J.R. Anderson, M. Boudart, *Catalytic Steam Reforming in Catalysis*, Science and Technology, Springer-Verlag, New York, 1984.

- [15] G. Jones, J.G. Jakobsen, S.S. Shim, J. Kleis, M.P. Andersson, J. Rossmeisl, F. Abild-Pedersen, T. Bligaard, S. Helveg, B. Hinnemann, J.R. Rostrup-Nielsen, I. Chorkendorff, J. Sehested, J.K. Nørskov, *J. Catal.* 259 (2008) 147.
- [16] Z.-P. Liu, P. Hu, *J. Am. Chem. Soc.* 125 (2003) 1958.
- [17] I.M. Ciobca, F. Frechard, R.A. van Santen, A.W. Kleyn, J. Hafner, *J. Phys. Chem. B* 104 (2000) 3364.
- [18] I.M. Ciobica, R.A. van Santen, *J. Phys. Chem. B* 106 (2002) 6200.
- [19] F. Abild-Pedersen, O. Lytken, J. Engbk, G. Nielsen, I. Chorkendorff, J.K. Nørskov, *Surf. Sci.* 590 (2005) 127.
- [20] I.M. Ciobica, R.A. van Santen, *J. Phys. Chem. B* 107 (2003) 3808.
- [21] B.S. Bunnik, G.J. Kramer, *J. Catal.* 242 (2006) 309.
- [22] A. Kokalj, N. Bonini, C. Sbraccia, S. de Gironcoli, S. Baroni, *J. Am. Chem. Soc.* 126 (2004) 16732.
- [23] A. Kokalj, N. Bonini, S. de Gironcoli, C. Sbraccia, G. Fratesi, S. Baroni, *J. Am. Chem. Soc.* 128 (2006) 12448.
- [24] Z.-P. Liu, P. Hu, *J. Chem. Phys.* 114 (2001) 8244.
- [25] R.A. van Santen, *Acc. Chem. Res.* 42 (1) (2009) 57.
- [26] X.-Q. Gong, R. Raval, P. Hu, *Surf. Sci.* 562 (2004) 247.
- [27] M.L. Grecea, E.H.G. Backus, B. Riedmüller, A. Eichler, A.W. Kleyn, M. Bonn, *J. Phys. Chem. B* 108 (2004) 12575.
- [28] Q.-L. Tang, Z.-X. Chen, *J. Chem. Phys.* 127 (2007) 104707.
- [29] A.A. Gokhale, J.A. Dumesic, M. Mavrikakis, *J. Am. Chem. Soc.* 130 (2008) 1402.
- [30] G.-C. Wang, S.-X. Tao, X.-H. Bu, *J. Catal.* 244 (2006) 10.
- [31] J.J.M. Wiener, P. Politzer, *J. Mol. Struct.* 427 (1998) 171.
- [32] G. Kresse, J. Furthmüller, *Comput. Mater. Sci.* 6 (1996) 15.
- [33] G. Kresse, J. Furthmüller, *Phys. Rev. B* 54 (1996) 11169.
- [34] J.P. Perdew, J.A. Chevary, S.H. Vosko, K.A. Jackson, M.R. Pederson, D.J. Singh, C. Fiolhais, *Phys. Rev. B* 46 (1992) 6671.
- [35] P.E. Blöchl, *Phys. Rev. B* 50 (1994) 17953.
- [36] G. Kresse, J. Joubert, *Phys. Rev. B* 59 (1999) 1758.
- [37] H.J. Monkhorst, J.D. Pack, *Phys. Rev. B* 13 (1976) 5188.
- [38] G. Henkelman, B.P. Uberuaga, H. Jónsson, *J. Chem. Phys.* 113 (2000) 9901.
- [39] M. Pozzo, G. Carlini, R. Rosei, D. Alfè, *J. Chem. Phys.* 126 (2007) 164706.
- [40] S. Wilke, V. Natoli, M.H. Cohen, *J. Chem. Phys.* 112 (2000) 9986.
- [41] A. Michaelides, V.A. Ranea, P.L. de Andres, D.A. King, *Phys. Rev. Lett.* 90 (2003) 216102.
- [42] A. Michaelides, A. Alavi, D.A. King, *J. Am. Chem. Soc.* 125 (2003) 2746.
- [43] Y. Cao, Z.-X. Chen, *Surf. Sci.* 600 (2006) 4572.

- [44] W.K. Offermans, A.P.J. Jansen, R.A. van Santen, G. Novell-Leruth, J.M. Ricart, J. Prez-Ramrez, *J. Phys. Chem. C* 111 (2007) 17551.
- [45] N. Brønsted, *Chem. Rev.* 5 (1928) 231.
- [46] M.G. Evans, N.P. Polanyi, *Trans. Faraday Soc.* 34 (1938) 11.
- [47] G. Jones, T. Bligaard, F. Abild-Pedersen, J.K. Nørskov, *J. Phys. Condens. Matter* 20 (2008) 064239.
- [48] A. Michaelides, Z.-P. Liu, C.J. Zhang, A. Alavi, D.A. King, P. Hu, *J. Am. Chem. Soc.* 125 (2003) 3704.
- [49] A. Michaelides, P. Hu, *J. Am. Chem. Soc.* 123 (2001) 4235.
- [50] A.A. Phatak, W.N. Delgass, F.H. Ribeiro, W.F. Schneider, *J. Phys. Chem. C* 113 (2009) 7269.

Chapter 4: The CO Formation Reaction Pathway in Steam Methane Reforming by Rhodium¹

Three different pathways toward CO formation from adsorbed CH and O are compared by quantum-chemical density functional theory (DFT) calculations for planar and stepped Rh surfaces. The overall barrier for CO formation of the conventional pathway and the pathway involving a formyl (CHO) species are very similar. This holds for both surfaces. The barrier for carbon-oxygen bond formation for the planar surface (180 kJ/mol) is substantially higher than that for the stepped surface (90 kJ/mol). The reaction path through intermediate formyl formation competes with direct formation of CO from recombination via adsorbed C and O atoms. Calculations are used as a basis for the analysis of the overall kinetics of the methane steam reforming reaction as a function of the particle size and the metal.

4.1. Introduction

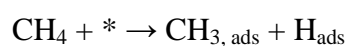
Steam methane reforming (SMR) is widely applied to produce hydrogen and synthesis gas (carbon monoxide and hydrogen) [1]. Synthesis gas is a versatile feedstock to produce

¹ This chapter has been published as “The CO Formation Reaction Pathway in Steam Methane Reforming by Rhodium” by Pieter W. van Grootel, Emiel J.M. Hensen and Rutger A. van Santen in *Langmuir* 2010, 26(21), 16339–16348

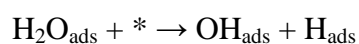
chemicals such as methanol or hydrocarbons through Fischer-Tropsch synthesis [2,3]. The most frequently used metal for SMR is nickel. In most applications, precious metal additives are used. Precious metals such as Rh, Ru, Pt, and Pd have a higher activity in SMR than Ni [1,3-9], but their use is limited by cost. The exact activity order remains a matter of debate [3-9]. As one of the most active metals for methane steam reforming, rhodium has been extensively studied as a reforming catalyst by quantum-chemical methods [10-15]. It remains a challenge to formulate detailed structure-activity relationships, not only because of the complex composition of the catalyst systems employed¹ but also due to the complex molecular chemistry occurring on metal surfaces [11,14-16]. Catalyst performance and deactivation of the catalyst are closely intertwined [16]. For a rational approach to select the optimum catalyst, a molecular description of the chemical events on the catalyst surface is required.

Of critical importance in steam methane reforming is the dependence of the reaction rate on the metal particle size. Experimentally, it has been demonstrated that the rate strongly depends on the particle size [4,6-9,11], which is due to the exposure of different surface metal atom topologies. A linear increase in the surface atom reaction rate has been reported with increasing metal dispersion for nanometer-sized particles [4,11]. Insight into the influence of the surface topology on the reactivity has recently been significantly improved by computer modeling [11,15,17-20]. These studies have described some of the reaction steps relevant to SMR, but they do not unequivocally support the experimental observation of a linear dependence of the rate on dispersion.

The answer to the question of how the SMR rate depends on the metal particle size is not straightforward. One realizes this when the reaction is unraveled into its elementary reaction steps. Methane activation results in adsorbed H and CH₃ species via



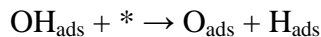
The adsorbed CH₃ is further dehydrogenated on the metal surface to adsorbed C via C-H bond cleavage reactions. Water activation proceeds either via



or via oxygen adatoms via



The backward reaction can also be used to generate oxygen adatoms on the surface. Either reaction is followed by O-H bond cleavage to O_{ads}



The third important step is the recombination of carbon and oxygen to CO and is the subject of the current study. Conventionally, this step is considered to involve C_{ads} and O_{ads} , requiring the dissociation of the methylidene (CH) intermediate prior to C-O bond formation



As methylidene dissociation is the most difficult of the consecutive dehydrogenation steps starting from $CH_{3,ads}$, pathways involving COH_{ads} (mechanism II) [25,27] and HCO_{ads} (mechanism III) [21,25-28] have also been considered. Mechanism II proceeds via formation of OH, subsequent formation of COH, and dissociation toward CO [25,27]:



The alternative involves formyl (CHO) as an intermediate toward CO formation [25,27] and takes place via



There is substantial computational catalysis and surface science literature available on each of these steps [21,24-28]. In this work, we will specifically address the issue of the particle size dependence of CO recombination for mechanisms I-III. In the discussion, we will compare our data with relevant literature data. To introduce these issues properly here, we will summarize the most important features of these reactions known from theory with respect to the particle size dependence [17,18].

Whereas most computed reaction data refer to surface slab calculations, these can be translated to particle size dependent trends as long as particles are not so small that bulk cluster-particle electronic effects start to play a role. This limits such considerations on particle size dependence to particles larger than approximately 1-1.5 nm. Above this particle size, differences in reactivity between particles become dominated by differences in the relative ratio of surface atoms with different topologies or coordination. The relative

concentration of edge and corner atoms on small particles is larger than that on large particles. Atoms with lower metal-metal coordination numbers than atoms in extended surfaces can be easily modeled by proper design of the surface slabs. The activation of methane is strongly affected by such sites. Trends in the particle size dependence of the methane activation reaction are well understood [4-9,11,13-16,18]. The activation barrier strongly decreases for corner and edge atoms compared to terrace atoms. Therefore, the rate of methane activation is expected to strongly increase for smaller particles. When one compares different metals, the activation energy of methane is found to correlate with the adsorption energies of C_{ads} [29].

Very important are also sites of particular topology, which have been called “B5” [23] or “C6” sites [30,31]. These sites are similar to the step-edge sites of surfaces. They consist typically of a particular configuration of 5 or 6 metal surface atoms. The activation of molecules such as CO and N_2 as well as the recombination of C_{ads} and O_{ads} proceed with a low energy barrier on such sites. The (211) surface investigated in this paper can be considered to model such “B5” sites. Early work by Van Hardeveld and Van Montfoort [23] suggested that topologies as those of the “B5” sites cannot be stabilized on particles smaller than 2-2.5 nm. Hence, reaction schemes involving C and O recombination as the rate controlling step would become suppressed when the particle size decreases below this threshold of disappearance of the “B5” type sites. This has recently been confirmed for the particle size dependence of the ammonia synthesis reaction for which N_2 dissociation is the slow step [32]. As for CO, low activation energy N_2 dissociation requires “B5” sites [33]. The lower activation energy of CO dissociation on step edge compared to terrace sites is well documented [15,17,20,21]. This difference also implies lower activation energy for CO recombination on sites with a lower metal-metal coordination number. Because these sites cannot be stabilized by small particles, one expects a maximum in the particle size dependence of the steam reforming reaction. This optimum can be as low as 2 nm, but it can be larger depending on the exact particle shape. Studies of CO recombination have been mostly explored from adsorbed C and O [15,17,20,21]. Although some works have considered reactions involving CH and O for Ru [26,28], Co [21,28], Pt, Rh, Pd [28], and Ni [25,28], the structure dependence is less understood.

Finally, the activation of water has only been scarcely investigated [10,34]. For Rh surfaces, we have recently found that H_2O dissociation is independent of surface coordination, but is of

comparable energy with the activation energy of methane dissociation on low-coordinated atoms [10].

An important microkinetic study of the SMR reaction has been recently published [11]. In this study, only the direct C and O recombination step is considered. It is the comparison of the three recombination steps that forms the main body of this paper. In the discussion, we will analyze our results with respect to the dependence of the overall SMR reaction rate as a function of particle size and comment on the optimum performance found for other metals.

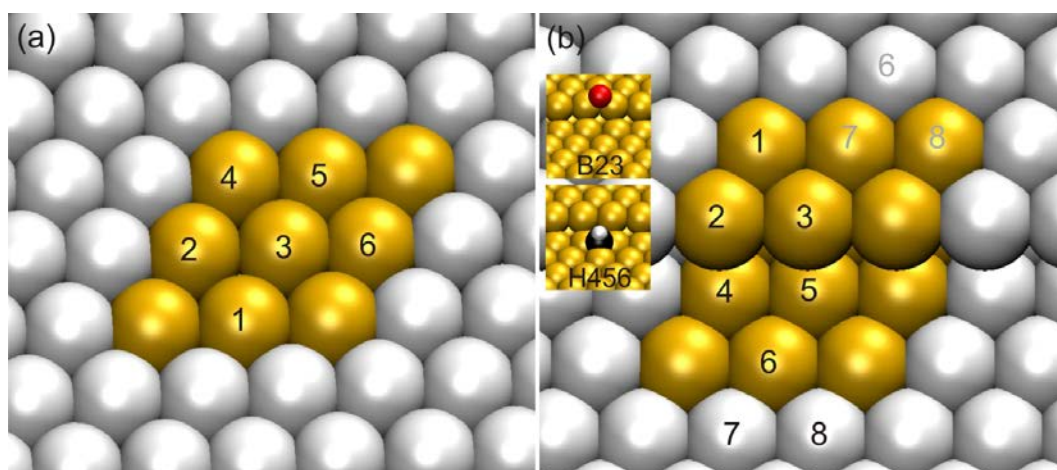


Figure 1. Schematic presentation of the two Rh surfaces employed in the present work: (a) Rh(111) and (b) Rh(211) surfaces. The yellow atoms make up the surface atoms in one unit cell. The numbers of the surface atoms denote the various adsorption sites. The two panels in (b) give an example of names for the adsorption sites.

4.2. Methods

The quantum-chemical calculations were carried out using the Vienna ab initio simulation package (VASP) [35,36] using the gradient-corrected PW91 exchange-correlation functional [37]. The projected-augmented wave (PAW) method [38,39] was used to describe electron-ion interactions. A plane wave basis set was employed for the valence electrons. The energy cutoff was set to 400 eV. Computations were performed with $3 \times 3 \times 1$ k -point sampling of the Brillouin zone (11 k -points) [40]. The third vector is perpendicular to the surface. The relaxation of the electronic degrees of freedom was assumed to be converged, when the total energy and the band structure energy changes between two electronic optimization steps were both smaller than 10^{-5} eV. Forces below 10^{-3} eV/Å for all ions were used as the criterion for convergence of ionic relaxation. The choices for the number of k -points, the plane-wave cut-off energy, and the size of the vacuum are generally comparable to research [11,13-15] to which we will mainly refer.

Adsorption energies (ΔE_{ads}) were calculated from the energy difference between the surface containing the geometry optimized adsorbate ($E_{\text{surface + adsorbate}}$) and the same surface with the adsorbing molecule placed in the middle of an empty box ($E_{\text{surface}} + E_{\text{adsorbing molecule}}$)

$$\Delta E_{\text{ads}} = E_{\text{surface + adsorbate}} - (E_{\text{surface}} + E_{\text{adsorbing molecule}})$$

For determining the transition state of reaction pathways, the climbing images nudged elastic band (CI-NEB) [41] method was employed. The initial, final, and transition state geometries were tested by analyzing the harmonic normal modes, which were calculated by using the finite difference method as implemented in VASP. Small displacements (0.02 Å) of adsorbed atoms and the three relaxed surface layers were used for the estimation of numerical Hessian matrix. The energy of each state was corrected for the zero point energy [42], computed using the results of the normal-mode analysis.

The model Rh(111) and Rh(211) surfaces are shown in Figure 1. The Rh(111) model consists of a periodic $p(3 \times 3)$ unit cell containing five layers of Rh atoms in a face-centered cubic (fcc) arrangement and a vacuum of 13 Å. The resulting surface consists of close packed atoms. The layering gives rise to two kind of hollow sites, a hexagonal close-packed (hcp) hollow site having a neighboring Rh atom directly located in the subsurface second layer and a fcc hollow site that does not contain a subjacent metal atom. This super cell contains 45 Rh atoms. The coordination number of the surface Rh atoms is 9. Four symmetric adsorption sites can be distinguished on the terrace surface. Besides the two 3-fold hollow sites (hcp and fcc), the surface contains top and bridge sites.

The Rh(211) surface contains (111) terraces and a (100) oriented monatomic step. The geometry of the terrace is the same as that of the Rh(111) surface. The number of layers in this model is 6, and the supercell contains 66 Rh atoms. The coordination numbers of the terrace and step edge surface atoms are 9 and 7, respectively. The coordination number of the atoms at the bottom of the step is 11. The stepped surface leads to a large number of potential adsorption sites. Fourteen symmetric adsorption sites are considered as sites of interest and are named by the numbers shown in Figure 1b and H for hollow, B for bridge, and T for top site.

Prior to the determination of the energy barriers for the activation of methylidyne (CH), the most favorable adsorption sites of the relevant species (CO, C, CH, O, and H) were determined. The reaction pathway analysis was then carried out starting from the most stable adsorption geometries of the participating molecules and atoms.

The vacuum space above all slab models was chosen to be 13 Å. Larger separation distances between the slabs in periodic images did not lead to a significantly lower energy. The top three layers of the supercells were allowed to relax during energy optimizations, and no symmetry restrictions were imposed. For several reaction pathways, it was confirmed that dipole corrections were not required.

4.3. Results and Discussion

4.3.1. Adsorption of Fragments on Rh(111) and Rh(211)

Surfaces. The adsorption energies of the surface adsorbates relevant for the surface reactions of CH with O are collected in Tables 1 and 2.

Table 1. Adsorption energies (kJ/mol) of CH_x, CO, OH_x, and H on the Rh(111) surface. Energies (kJ/mol) are relative to the corresponding species in vacuum. The most stable adsorption sites of the respective species are in bold.

	C	CH	CO	OH	O	H
bridge	-702	-652	-198	-284	-540	-262
fcc	-755	-695	-207	-312	-586	-275
hcp	-770	-709	-213	-293	-585	-272
top	-560	-498	-191	-219	-445	-237

Table 2. Adsorption energies (kJ/mol) for CH_x, CO, OH_x, and H species on Rh(211). Energies are relative to the corresponding species in vacuum. Bold values indicate the most stable adsorption site for the respective species, except for H since the differences between most sites are within the margin of the calculation methods used. The adsorption sites are denoted by T (top), B (bridge), and H (hollow) with the numbers referring to the sites given in Figure 1b.

	C	CH	CO	OH	O	H
B46	-701	-640	-197	n.a. ^a	-452	-155
B45	n.a. ^a	n.a. ^a	n.a. ^a	-277	-482	-154
B24	n.a. ^a	-622	-209	-278	-473	-161
B12	n.a. ^a	-624	-196	-274	-472	-151
B23	-702	-631	-217	-335	-529	-165
H456	-740	-683	-204	-270	-503	-164
H2345	-813	-695	-189	n.a. ^a	-512	-157
H123	-777	-694	-219	-300	-528	-163
T6	-540	-478	-189	n.a. ^a	n.a. ^a	-130
T1	-540	n.a. ^a	-187	-254	-356	-127
T2	-571	-514	-204	-295	-427	-128

a) not available

Methyldiyne (CH) preferentially adsorbs in the hcp-hollow site on the planar Rh(111) surface in accordance with previous studies [14,27] (Figure 2a). In accordance with previous results [27], CH is substantially less stable on bridge and top sites. The case is different for the

stepped Rh(211) surface, where three favorable configurations are identified for CH, namely, the hcp-hollow sites below and on top of the step (H123 and H456) and the 4-fold hollow site in the step (H2345) (Figure 2b) with very small energy differences. Similar to the planar surface, adsorption in bridge and top sites is much less favorable. For the planar surface, adsorption of the carbon atom in the hcp-hollow site is preferred by 15 kJ/mol over the fcc-hollow site. Similar to CH, the adsorption of C on bridge and top sites is unfavorable.

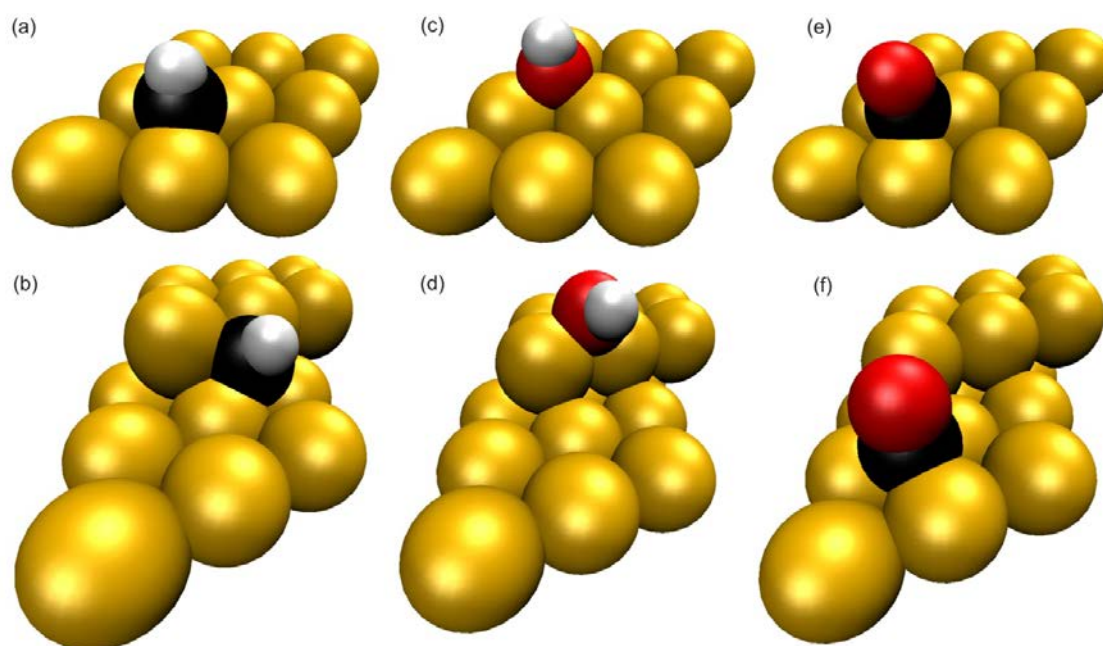


Figure 2. Geometries of the most stable adsorption states of CH (a,b), OH (c,d), and CO (e,f) on the planar (top) and stepped (bottom) surfaces of rhodium

For the stepped surface, the 4-fold hollow site formed by the step (H2345) presents a very stable adsorption site for atomic carbon. The adsorption of carbon on the adjacent hcp hollow site (H123) is less stable by 73 kJ/mol. As expected, there is a slight preference for H adsorption in the hollow sites. The energy differences with the bridge sites are relatively small, implying that H diffusion over the surface should be fast. Oxygen prefers to sit in hcp- and fcc-hollow sites on the planar surface, whereas it is preferentially located on the bridge site of the step (B23) and the adjacent hcp-hollow site (H123) on the stepped surface. The barrier for migration between H123 and B23 is very small (17 kJ/mol).

Finally, the intermediate OH fragment is preferentially located on the fcc-hollow site and the bridge site of the step (B23) on the planar and stepped surface, respectively. On the planar surface, OH adsorbs with in a slightly tilted mode. On the stepped surface, OH points away from the step site (Figure 2c,d). The CO product of the reactions under investigation prefers

to adsorb on the hollow sites of the planar surface and the bridge site of the step (B23) and the adjacent hcp-hollow site for the stepped surface (H123) (Figure 2e,f). On the planar surface, the CO has an upright adsorption. On the stepped surface, CO is adsorbed on the lower terrace and is tilted toward the adjacent step atoms.

4.3.2. Mechanistic Investigation

The reaction pathway of the three mechanisms (I-III) for CO formation considered in the Introduction were determined by quantum-chemical calculations. Figures 3 and 4 show the potential energy diagram for these reactions for the planar Rh(111) and stepped Rh(211) surfaces, respectively. For the planar surface, the starting configuration includes CH in the hcp-hollow site and an O atom at infinite distance in the hcp-hollow site. Similarly, the reaction pathway starts with CH in the 4-fold hollow site of the step H2345 and O at the B23 site at infinite distance. The energy differences for migration of H(O) from (to) the reaction site are accounted for in the potential energy diagrams.

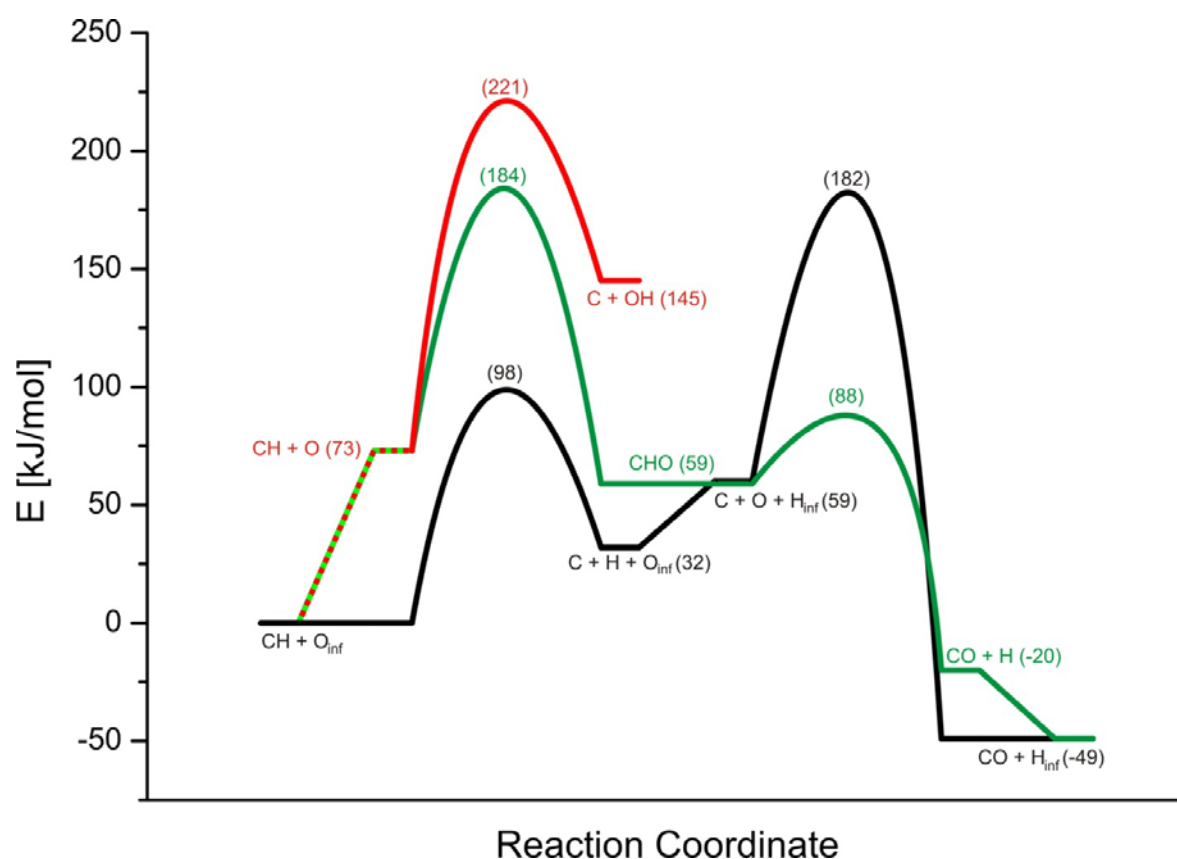


Figure 3. Energy diagram for CO formation pathways I (black), II (red), and III (green) on Rh(111) in kJ/mol. The starting configuration is carbon and oxygen in 3-fold hollow sites at infinite distance. The barriers for mechanisms I and III are close at about 180 kJ/mol.

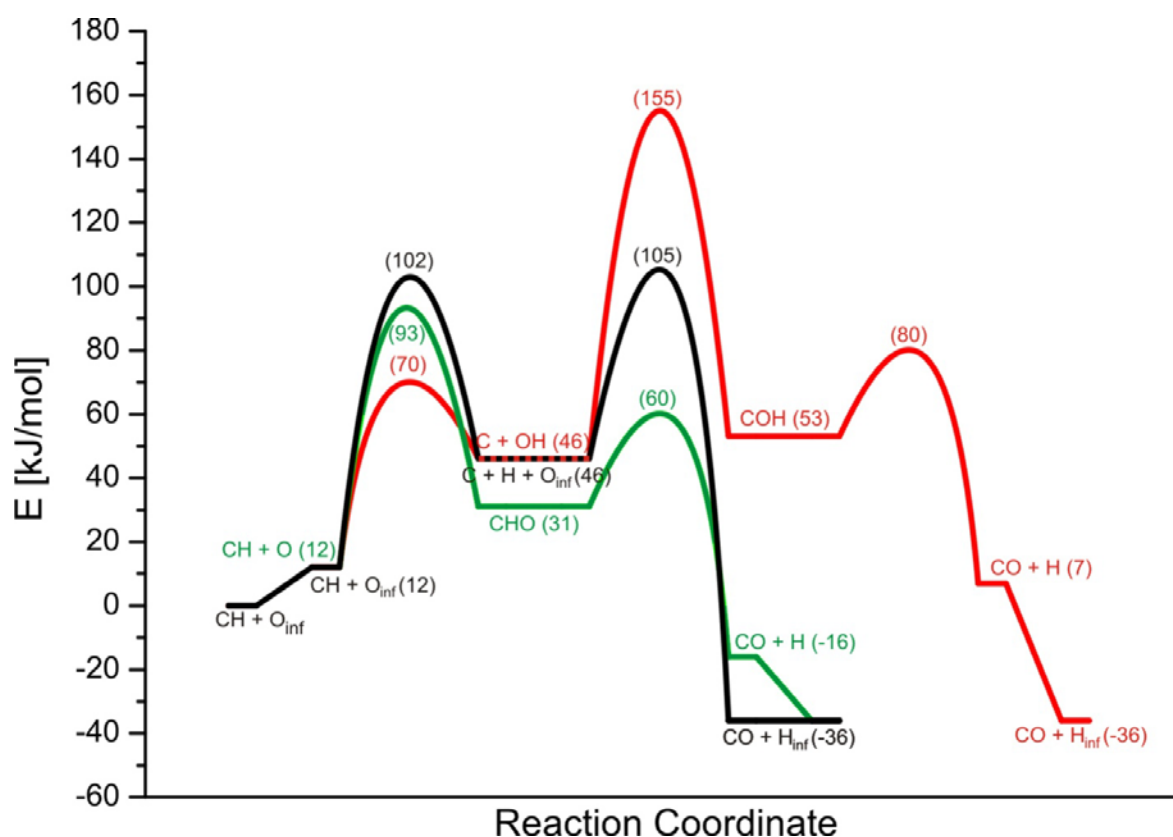


Figure 4. Energy diagram for CO formation pathways I (black), II (red), and III (green) on Rh(211) in kJ/mol. The starting configuration is CH in the 4-fold hollow site of the step (H2345) and O at infinite distance on the bridge site of the step. Mechanisms I and III have comparable overall barriers at approximately 90 kJ/mol.

4.3.2.1 Mechanism I

The CH + O reaction to form CO by recombination of adsorbed C and O atoms requires the dissociation of methylidyne (reaction Ia). On the planar surface, CH is initially adsorbed in the hcp-hollow site (Figure 5A and Table 3). In the transition state, the CH bond is stretched toward the top of an adjacent Rh atom. During dissociation, the hydrogen does not cross over the top of the atom but migrates into the vacant hcp hollow site. The barrier for CH dissociation and the reaction enthalpy are 91 and 32 kJ/mol, respectively. Both the activation energy and the reaction enthalpy are slightly lower than reported values for the activation energy (116 kJ/mol [14] and 125 kJ/mol [27]) and for the enthalpy (57 kJ/mol [14] and 66 kJ/mol [27]). This is mainly due to our choice of a larger unit cell, which leads to a smaller influence of lateral interactions with adsorbates in adjacent cells. Another reason is that our energies are corrected for the vibrational zero-point energy. On the stepped surface, methylidyne is preferentially adsorbed in the 4-fold hollow site (H2345). The preferential pathway for dissociation involves C-H cleavage from the 3-fold site (H456). This adsorption state will also be considered for the other two mechanisms on the stepped surface.

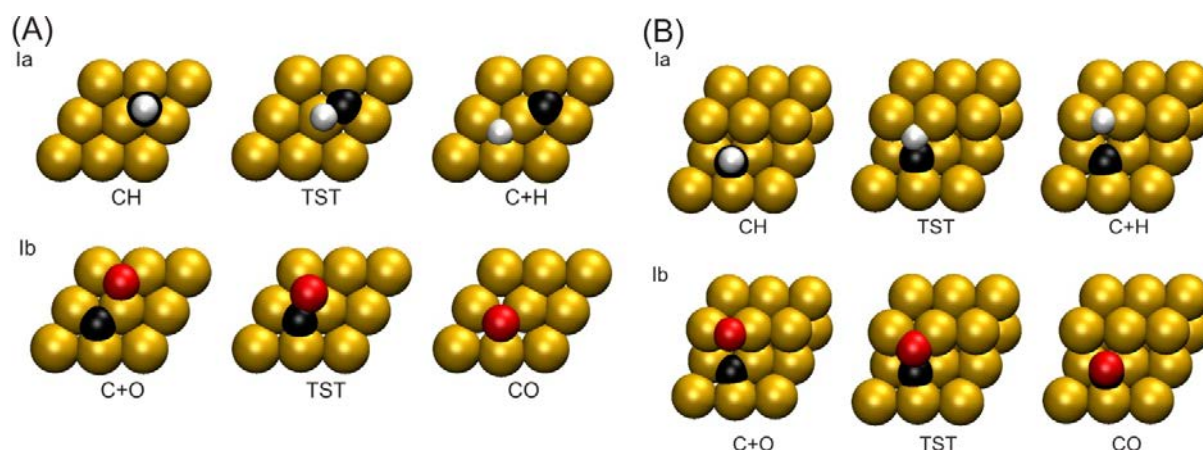


Figure 5. Formation of CO via mechanism I on Rh(111) (A) and Rh(211) (B) with carbon, oxygen, and hydrogen atoms in black, red, and white, respectively. Shown are the initial state (left), transition state (middle), and final state (right).

Table 3. Geometrical parameters of CO formation via Pathway I on Rh(111). The atom numbers refer to the numbers used in Figure 1a. Bond lengths (r) are given in Å and angles (θ) in degrees.

	CH	TST	C+H	C+O	TST	CO
$r(\text{Rh1} - \text{C})$	1.98	1.89	1.89	1.88	1.96	2.15
$r(\text{Rh2} - \text{C})$	1.98	1.89	1.89	1.89	1.90	2.14
$r(\text{Rh3} - \text{C})$	1.98	1.95	1.90	1.95	1.97	2.15
$r(\text{C} - \text{H})$	1.10	1.66	n.a.	n.a.	n.a.	n.a.
$r(\text{Rh3} - \text{H})$	n.a.	1.62	1.83	n.a.	n.a.	n.a.
$r(\text{Rh5} - \text{H})$	n.a.	n.a.	1.87	n.a.	n.a.	n.a.
$r(\text{Rh6} - \text{H})$	n.a.	n.a.	1.87	n.a.	n.a.	n.a.
$r(\text{Rh3} - \text{O})$	n.a.	n.a.	n.a.	2.07	2.08	n.a.
$r(\text{Rh4} - \text{O})$	n.a.	n.a.	n.a.	1.99	2.02	n.a.
$r(\text{Rh5} - \text{O})$	n.a.	n.a.	n.a.	1.99	n.a.	n.a.
$r(\text{C} - \text{O})$	n.a.	n.a.	n.a.	n.a.	1.87	1.77
$\theta(\text{Rh1} - \text{C} - \text{H})$	125.1	126.0	n.a.	n.a.	n.a.	n.a.
$\theta(\text{Rh2} - \text{C} - \text{H})$	125.1	126.0	n.a.	n.a.	n.a.	n.a.
$\theta(\text{Rh3} - \text{C} - \text{H})$	125.3	52.4	n.a.	n.a.	n.a.	n.a.
$\theta(\text{Rh1} - \text{C} - \text{O})$	n.a.	n.a.	n.a.	n.a.	158.4	120.0
$\theta(\text{Rh2} - \text{C} - \text{O})$	n.a.	n.a.	n.a.	n.a.	95.0	119.4
$\theta(\text{Rh3} - \text{C} - \text{O})$	n.a.	n.a.	n.a.	n.a.	65.5	119.8

Table 4. Geometrical parameters of CO formation via Pathway I on Rh(211). The atom numbers refer to the numbers used in Figure 1b. Bond lengths (r) are given in Å.

	CH	TST	C+H	C+O	TST	CO
$r(\text{Rh4} - \text{C})$	1.99	1.94	1.88	1.87	1.92	2.07
$r(\text{Rh5} - \text{C})$	1.99	1.94	1.90	1.91	1.94	2.09
$r(\text{Rh6} - \text{C})$	1.99	1.98	1.88	1.87	1.96	2.05
$r(\text{Rh2} - \text{H})$	3.30	2.00	1.78	n.a.	n.a.	n.a.
$r(\text{Rh3} - \text{H})$	3.09	1.89	1.76	n.a.	n.a.	n.a.
$r(\text{C} - \text{H})$	1.10	1.57	3.20	n.a.	n.a.	n.a.
$r(\text{Rh2} - \text{O})$	n.a.	n.a.	n.a.	1.90	1.99	3.22
$r(\text{Rh3} - \text{O})$	n.a.	n.a.	n.a.	1.90	1.98	3.06
$r(\text{C} - \text{O})$	n.a.	n.a.	n.a.	3.22	1.99	1.24

During dissociation, the CH bond (Figure 5B and Table 4) stretches toward the bridge of the step (B23), which forms the final adsorption site for the H atom. The barrier is found to be 90 kJ/mol, and the reaction enthalpy 34 kJ/mol. Typically, the energy barrier for dissociation of diatomic molecules is much lower on stepped than on planar surfaces [15,20,21], because the particular surface topology of steps avoids the sharing of metal atoms with the dissociating fragments. In the present case, however, the barriers for CH dissociation are similar for both surfaces, because the geometrical and electronic advantages of the stepped site are negated by the relatively long distance that the C-H bond has to stretch toward the B23 site.

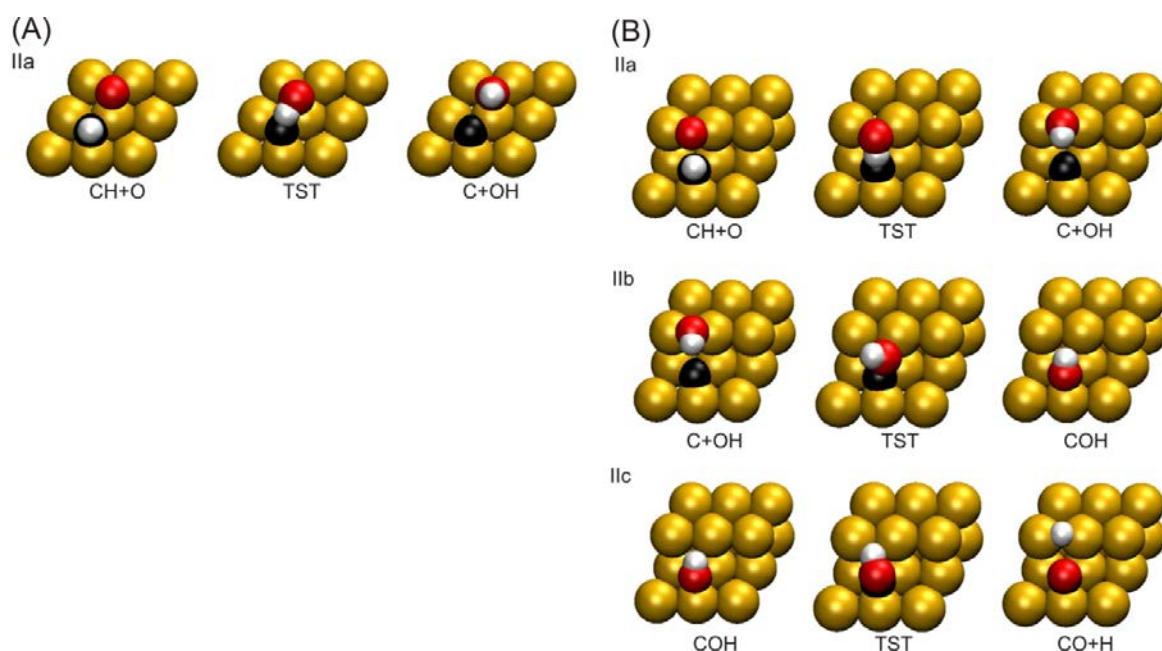


Figure 6. Formation of CO via mechanism II on Rh(111) (A) and Rh(211) (B) with carbon, oxygen, and hydrogen atoms in black, red, and white, respectively. Shown are the initial state (left), transition state (middle), and final state (right).

During the CO forming (reaction Ib) on Rh(111), the carbon atom has to move slightly out of the 3-fold site to react with the oxygen adatom. The final adsorption site of the CO product is the hcp-hollow site where carbon was initially present. This pathway has a barrier of 123 kJ/mol and a reaction enthalpy of -108 kJ/mol. The activation energy is close to the value reported by Inderwildi *et al.* [27] (99 kJ/mol) but lower than the one reported by Liu and Hu [15] (178 kJ/mol). The higher value of Liu and Hu is due to the choice of the reference state, that is, C and O adsorbates at infinite distance in their case and in close proximity in ours. Based on the reaction enthalpy, we compute a barrier for CO dissociation on the planar surface of 231 kJ/mol in agreement with literature [25]. On Rh(211), carbon recombines from the 3-fold hollow site on the lower terrace (H456) with the oxygen on the bridge site of the step (BU23). The oxygen atom moves toward the carbon atom and the final configuration

involves CO in the H456 site. This pathway for CO formation has an activation barrier of only 59 kJ/mol and a reaction enthalpy of -82 kJ/mol. The barrier for CO formation is much lower than that on the planar surface, which is understood by the fact that on this particular surface metal sharing between the C and O adsorbates is avoided in the initial state and the transition state.

Table 5. Geometrical parameters of CO formation via Pathway II on Rh(111). The atom numbers refer to the numbers used in Figure 1a. Bond lengths (r) are given in Å and angles (θ) in degrees.

	CH + O	TST	C+OH
$r(\text{Rh1} - \text{C})$	1.96	1.94	1.88
$r(\text{Rh2} - \text{C})$	1.97	1.94	1.90
$r(\text{Rh3} - \text{C})$	3.01	2.04	1.95
$r(\text{Rh3} - \text{O})$	2.07	2.13	2.21
$r(\text{Rh4} - \text{O})$	1.99	2.00	2.16
$r(\text{Rh5} - \text{O})$	2.00	2.62	2.16
$r(\text{C} - \text{H})$	1.10	1.33	n.a.
$r(\text{O} - \text{H})$	n.a.	1.34	0.99
$\theta(\text{Rh1} - \text{C} - \text{H})$	127.0	163.7	n.a.
$\theta(\text{Rh2} - \text{C} - \text{H})$	122.6	99.5	n.a.
$\theta(\text{Rh3} - \text{C} - \text{H})$	121.6	78.4	n.a.
$\theta(\text{Rh3} - \text{O} - \text{H})$	n.a.	74.6	120.7
$\theta(\text{Rh4} - \text{O} - \text{H})$	n.a.	109.2	133.7
$\theta(\text{Rh5} - \text{O} - \text{H})$	n.a.	143.4	137.6
$\theta(\text{C} - \text{H} - \text{O})$	n.a.	132.1	n.a.

4.3.2.2 Mechanism II

This mechanism involves the oxygen assisted dissociation of methylidyne which, for Rh(111), proceeds with CH and O adsorbed in adjacent hcp-hollow sites (Figure 6A and Table 5). The cost associated with bringing the two reactants in this configuration is 73 kJ/mol. During CH dissociation, the O atom (reaction IIa) moves toward the CH fragment, after which the hydrogen is transferred to oxygen. The barrier is 148 kJ/mol and the reaction enthalpy 72 kJ/mol in agreement with literature [27]. The relatively high barrier is due to the fact that the carbon and oxygen atoms share the same Rh atoms in the initial and transition state. On the stepped surface (Figure 6B and Table 6), however, the accepting oxygen atom is located on the bridge of the step (B23) and the methylidyne on the lower terrace (H456). The final state consists of the hydroxyl on the bridge site, while the carbon remains in the 3-fold hollow site. This pathway has a much lower barrier of 58 kJ/mol, and the energy of reaction is 34 kJ/mol. As the barrier for the oxygen-assisted dissociation on Rh(111) is significantly higher than that of the CH dissociation (reaction Ia), reaction IIb was not further considered for this surface. On the stepped surface, COH formation via this reaction proceeds with a

barrier of 109 kJ/mol (Figure 6B). COH is finally adsorbed in H456. The final step H abstraction step (reaction IIc) proceeds with a very low barrier of 27 kJ/mol.

Table 6. Geometrical parameters of CO formation via Pathway II on Rh(211). The atom numbers refer to the numbers used in Figure 1b. Bond lengths (r) are given in Å and angles (θ) in degrees.

	CH + O	TST	C + OH	TST	COH	TST	CO + H
r(Rh4 – C)	1.99	1.97	1.89	1.92	2.02	2.05	2.09
r(Rh5 – C)	2.00	1.99	1.91	1.95	2.03	2.05	2.10
r(Rh6 – C)	1.95	1.92	1.88	1.93	1.97	1.99	2.07
r(Rh2 – O)	1.91	2.07	2.10	2.65	3.57	3.04	n.a.
r(Rh3 – O)	1.90	2.00	2.11	2.11	3.45	2.95	n.a.
r(C – H)	1.10	1.33	3.55	n.a.	n.a.	n.a.	n.a.
r(O – H)	2.44	1.26	0.99	1.00	1.01	1.30	n.a.
r(C – O)	n.a.	n.a.	n.a.	1.98	1.35	1.30	1.23
r(Rh2 – H)	n.a.	n.a.	n.a.	n.a.	n.a.	1.91	1.78
r(Rh3 – H)	n.a.	n.a.	n.a.	n.a.	n.a.	2.15	1.75
θ (Rh4 – C – H)	125.2	103.5	94.9	n.a.	n.a.	n.a.	n.a.
θ (Rh5 – C – H)	126.3	108.37	101.7	n.a.	n.a.	n.a.	n.a.
θ (Rh6 – C – H)	124.5	151.8	142.9	n.a.	n.a.	n.a.	n.a.
θ (C – H – O)	106.1	148.0	91.7	n.a.	n.a.	n.a.	n.a.
θ (Rh2 – O – H)	n.a.	103.9	115.2	76.2	49.6	22.8	n.a.
θ (Rh3 – O – H)	n.a.		100.8	116.3		128.5	45.0
θ (Rh4 – C – O)	n.a.		n.a.	n.a.		109.7	128.7
θ (Rh5 – C – O)	n.a.		n.a.	n.a.		99.8	131.0
θ (Rh6 – C – O)	n.a.		n.a.	n.a.		144.9	120.5
θ (C – O – H)		n.a.		n.a.	n.a.		120.7

Table 7. Geometrical parameters of CO formation via Pathway III on Rh(111). The atom numbers refer to the numbers used in Figure 1a. Bond lengths (r) are given in Å and angles (θ) in degrees.

	CH + O	TST	CHO	TST	CO + H
r(Rh1 – C)	1.96	2.18	3.02	2.79	2.09
r(Rh2 – C)	1.97	1.96	2.17	2.12	2.08
r(Rh3 – C)	3.01	2.04	1.98	2.03	2.08
r(Rh3 – O)	2.07	2.06	n.a.	n.a.	n.a.
r(Rh4 – O)	1.99	2.03	n.a.	n.a.	n.a.
r(Rh5 – O)	2.00	3.05	n.a.	n.a.	n.a.
r(C – H)	1.10	1.10	1.10	1.16	n.a.
r(C – O)	n.a.	1.82	1.33	1.26	1.22
r(Rh3 – H)	n.a.	n.a.	n.a.	n.a.	1.82
r(Rh4 – H)	n.a.	n.a.	n.a.	n.a.	1.83
r(Rh5 – H)	n.a.	n.a.	n.a.	n.a.	1.83
θ (Rh1 – C – H)	127.0	108.2	81.6	60.9	n.a.
θ (Rh2 – C – H)	122.6	130.9	119.0	129.6	n.a.
θ (Rh3 – C – H)	121.6	129.8	122.6	81.4	n.a.
θ (H – C – O)	n.a.	94.0	115.1	120.5	n.a.
θ (Rh1 – C – O)	n.a.	n.a.	n.a.	141.8	127.2
θ (Rh2 – C – O)	n.a.	n.a.	82.6	97.1	128.3
θ (Rh3 – C – O)	n.a.	n.a.	118.5	120.5	129.5

4.3.2.3 Mechanism III

The third pathway considered here involves the formyl intermediate (CHO). For the planar Rh(111) surface (Figure 7A and Table 7), formyl is formed in the bridge position from CH and O adsorbed in two adjacent hcp-hollow sites (reaction IIIa). Similar to pathway II, the migration of the fragments to this position costs 73 kJ/mol. Formation of formyl proceeds with a barrier of 111 kJ/mol and an enthalpy of -16 kJ/mol. These values are in excellent agreement with the values of 113 and -14 kJ/mol reported by Inderwildi *et al.* [27] The formation of formyl on Rh (211) (Figure 7B and Table 8) from methylidyne in H456 and oxygen in B23 has a lower activation energy of 81 kJ/mol and a reaction enthalpy of 19 kJ/mol. The formyl intermediate is less stable on Rh(211) than on Rh(111). The reason is the steric hindrance of the step. The final step is the dissociation of the C-H bond of formyl (reaction IIIb), which proceeds with very low barriers, 29 mol for both Rh(111) and Rh(211) surfaces.

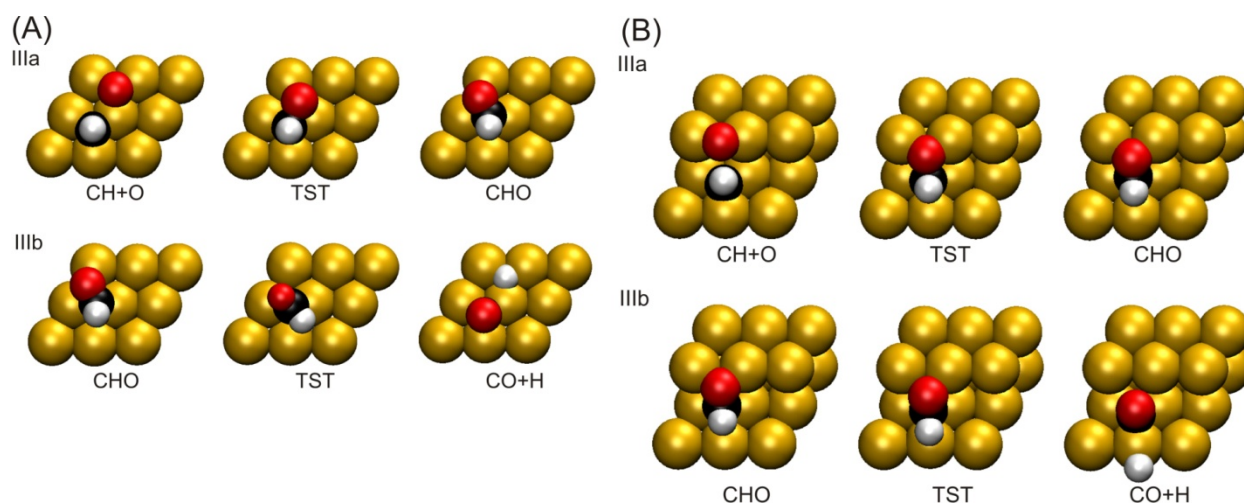


Figure 7. Formation of CO via mechanism III on Rh(111) (A) and Rh(211) (B) with carbon, oxygen, and hydrogen atoms in black, red, and white, respectively. Shown are the initial state (left), transition state (middle), and final state (right).

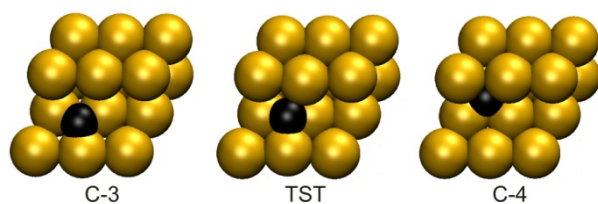


Figure 8. Pathway for C migration from the 3-fold hollow site into the 4-fold hollow site formed by the stepped surface, with carbon atoms in black. Shown are the initial state (left), transition state (middle), and final state (right).

Table 8. Geometrical parameters of CO formation via Pathway III on Rh(211). The atom numbers refer to the numbers used in Figure 1b. Bond lengths (r) are given in Å and angles (θ) in degrees.

	CH + O	TST	CHO	TST	CO + H
r(Rh4 – C)	1.99	1.98	2.04	2.03	2.10
r(Rh5 – C)	2.00	2.00	2.08	2.04	2.11
r(Rh6 – C)	1.95	2.26	2.59	2.15	2.04
r(Rh2 – O)	1.91	1.98	2.14	2.46	3.20
r(Rh3 – O)	1.90	1.97	2.11	2.27	3.01
r(C – O)	n.a.	1.88	1.38	1.32	1.23
r(C – H)	1.10	1.10	1.12	1.47	n.a.
r(Rh6 – H)	n.a.	n.a.	n.a.	1.65	1.86
r(Rh7 – H)	n.a.	n.a.	n.a.	n.a.	1.83
r(Rh8 – H)	n.a.	n.a.	n.a.	n.a.	1.84
θ (Rh4 – C – H)	125.2	133.9	118.7	118.4	n.a.
θ (Rh5 – C – H)	126.3	132.1	115.7	116.1	n.a.
θ (Rh6 – C – H)	124.5	88.2	62.7	49.9	n.a.
θ (H – C – O)	n.a.	86.7	108.6	102.4	n.a.
θ (Rh4 – C – O)	n.a.	100.9	112.8	115.7	126.9
θ (Rh5 – C – O)	n.a.	105.4	115.9	116.6	128.0
θ (Rh6 – C – O)	n.a.	174.8	62.7	152.3	134.4

Table 9. Geometrical parameters of C migration from threefold hollow site into the fourfold hollow site unique to the stepped surface Rh(211). The atom numbers refer to the numbers used in Fig. 1b. Bond lengths (r) are given in Å.

	C-3	TST	C-4
r(Rh2 – C)	3.39	3.03	2.11
r(Rh3 – C)	3.20	2.48	1.97
r(Rh4 – C)	1.89	1.92	1.99
r(Rh5 – C)	1.91	1.91	2.05
r(Rh6 – C)	1.89	2.14	3.49

4.3.3. General Discussion

Here, we will discuss the implication of our results for CO recombination on planar and stepped Rh surfaces in combination with literature data on Rh-catalyzed SMR. In general, dissociative CH₄ adsorption and CO formation have been considered rate limiting steps in the steam reforming of methane [11,12]. In the further dehydrogenation of the CH₃ adsorbate toward adsorbed C following methane dissociative adsorption, the dissociation of CH has the highest barrier [14]. Besides direct recombination of C_{ads} and O_{ads}, CO formation can occur via CH through formyl formation by recombination with O_{ads} or via an alcoholate intermediate. The present results show that CO formation via a formyl intermediate (mechanism III) competes with the direct pathway (mechanism I). The pathway involving a COH intermediate (mechanism II) is not favorable and can be discarded for both surfaces. On Rh(111), the formation of the C-O bond to CO or CHO proceeds with a high energy barrier

due to the destabilization of the transition state, which results from shared bonding of the reaction fragments with a single metal surface atom. The barrier for this reaction step is around 180 kJ/mol, which is substantially higher than the computed barrier for the stepped Rh(211) surface. The absence of metal atom sharing during C-O bond formation steps for the stepped surface explains the lower barrier. In this case, the pathway via formyl is slightly favored over the conventional pathway. Because of the absence of metal atom sharing, the oxygen-assisted cleavage of CH is the most favorable initial step on the stepped surface. Another significant difference with the planar surface is the much lower energy cost for bringing CH and O in positions favorable for H transfer. The formation of COH is also very unfavorable for the stepped surface.

Our analysis of the reactions occurring on the stepped surface indicates that the surface carbon atom formed upon C-H cleavage can easily diffuse (barrier ~15 kJ/mol) to the 4-fold hollow site in the step (H2345) (Figure 8 and Table 9), where it is more stable by 73 kJ/mol than in its initial hcp-hollow site (H456). Thus, although the energy cost for the overall pathway to CO via COH is prohibitively high, the low barrier for the formation of atomic carbon by dissociation of COH into adsorbed C and OH fragments opens a potential pathway to deactivation of the step sites. Note that the barrier for direct atomic carbon atom formation by CH bond cleavage is significantly higher.

We will now turn to the implications of these results for the particle size dependence of Rh-catalyzed SMR and extend this discussion to other metals. A comparison of the computed activation energies of dissociative CH₄ adsorption (70 kJ/mol) [14] and H₂O dissociation (67 kJ/mol) [11] with that of CHO formation (~180 kJ/mol) would suggest that the surface reaction of CO formation is the rate limiting step in the steam reforming reaction of methane on the planar surface. Experimentally, however, methane dissociation has most frequently been reported to be the rate limiting step [6-9,11]. The reason for this apparent discrepancy is that, whereas entropic changes are small for surface reactions, these tend to become large for elementary reaction steps involving adsorption or desorption of molecules. At typical reforming temperatures, the entropy loss due to adsorption substantially contributes to the free energy of activation via $\Delta G_{\text{act}} = \Delta E_{\text{act}} - T\Delta S_{\text{act}}$. Assuming that in the transition state for dissociation there is no mobility of the fragments and just one rotational degree of freedom, an activation entropy of $\Delta S = -130 \text{ J/mol}\cdot\text{K}$ is estimated for methane dissociative adsorption. The loss in activation entropy for water dissociation with respect to the gas phase has a

comparable value. At a temperature of 773 K, this entropy loss implies an increase of the activation free energy of 100 kJ/mol. This is to be contrasted to the activation entropies of the surface recombination reactions. Because adsorbates as well as transition states for recombination are rather immobile to a very good approximation, activation entropies can be ignored [43]. As a consequence, the dissociative adsorption of methane and water dissociation may become rate limiting under experimental conditions. This notion has an interesting consequence for the particle size dependence of the reaction. If, for instance, the barrier for methane dissociation is higher than the barriers of the other steps, the particle size dependence of methane activation will control the particle size dependence of the overall steam reforming reaction. Consequently, the reaction rate increases with decreasing particle size in line with the observed experimental behavior.

By applying Brønsted-Evans-Polanyi (BEP) principles [17,22,44-48] to available activation energy data, we can extrapolate the discussion of the overall reaction rate as a function of particle size for Rh to other metals. In BEP relations, the activation energy is related to the adsorption energy of the reacting adsorbate(s) $\Delta E_{\text{act}} = \alpha \Delta E_{\text{act}} + \beta$. The proportionality constant α is a measure of the lateness of the transition state (TS) of a reaction, with α being between 0 (early TS) and 1 (late TS).

We base our analysis on the schematic Figure 9. The behavior of the three essential elementary reaction steps as a function of the relevant adsorption energies is sketched. We use the activation energies for methane and water dissociation for the planar close packed surfaces of a number of metals based on literature data [15,20,34,49-58]. Expectedly, these barriers strongly depend on the adsorption energy of carbon and oxygen, respectively. This dependence is well understood. The late transition state nature of dissociative adsorption of methane implies a BEP proportionality constant close to unity [17,43]. The value of α for methane dissociation of ~ 0.8 is in good agreement with this notion [17,22]. As reported earlier [10], the BEP proportionality constant for water dissociation amounts to $\alpha = 0.5$. When related to the adsorption energy of OH, this proportionality constant is unity in line with the late nature of this step.

Based on our results and the limited data in literature [28], we can also determine how the barrier for CH and O recombination depends on the adsorption energies of CH and O. It turns out that the barrier for the surface recombination of CHO depends only weakly on the adsorption energies of the relevant adsorbates and has a relatively small proportionality

constant ($\alpha = 0.05$) in the BEP-type relation $\Delta E_{\text{act}} = \alpha (\Delta E_{\text{CH}} + \Delta E_{\text{O}}) + \beta$, with ΔE_{CH} and ΔE_{O} being the adsorption energies of methylidyne and atomic oxygen, respectively. This value is conveniently close to zero to set the value of α to zero in Figure 9. This result is expected, because surface recombination reactions tend to have low BEP proportionality constants [17].

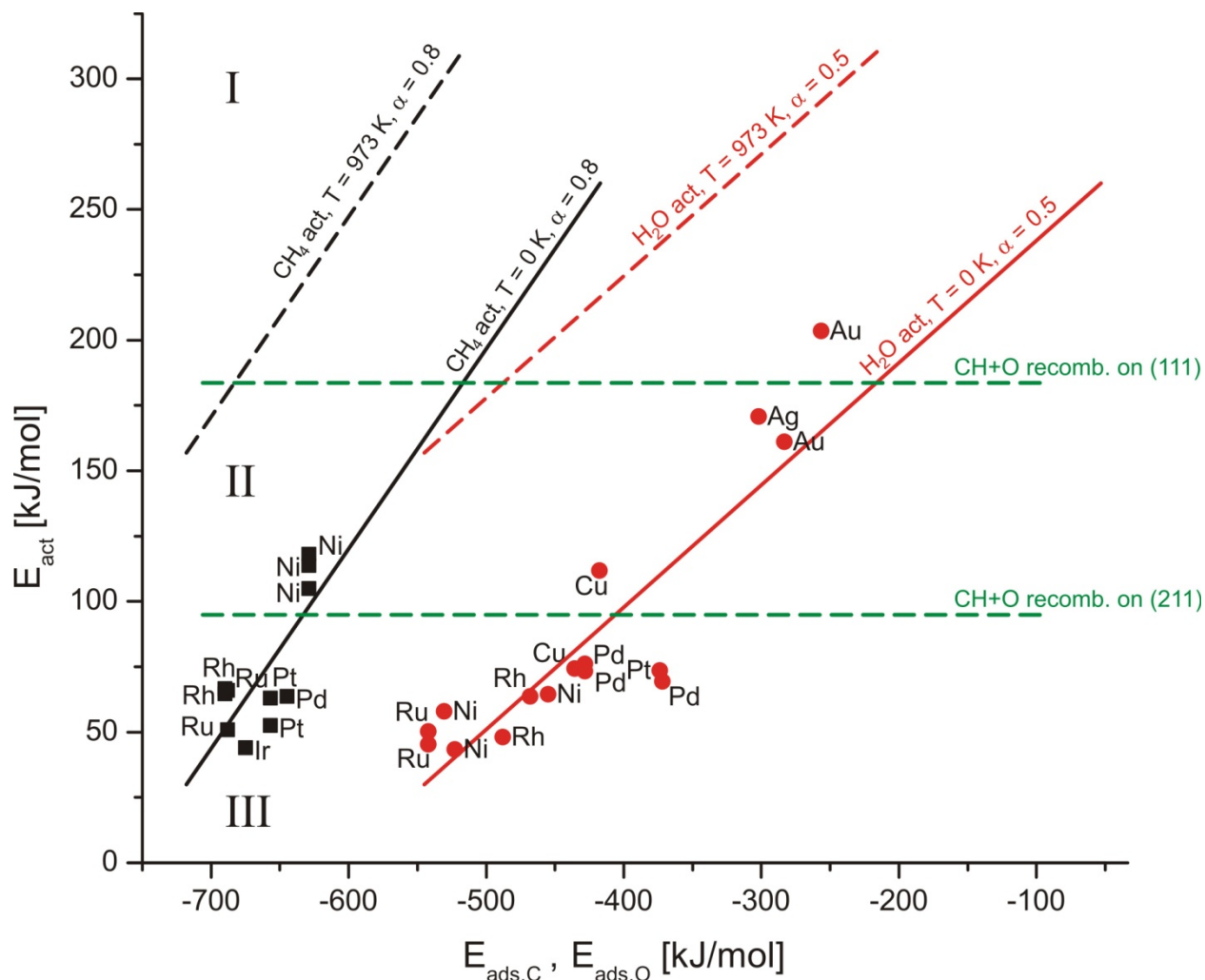


Figure 9. Activation energies for CH_4 (black) [15,20,41-46] and H_2O (red) [47-51] dissociation at 0 K plotted versus the adsorption energy of C or O. The water dissociation energy is relative to the desorbed state of the H_2O molecule. The dashed lines represent the free activation energies at a reaction temperature of 973 K. The trend lines and values for α are obtained by applying linear regression of the data points. The trend line for the free activation energy of $\text{CH} + \text{O}$ on Rh(111) and Rh(211) is also given (green).

Three different performance-structure regimes can be distinguished in Figure 9. The first regime at high temperature involves free activation energies for methane and water dissociation higher than the barrier for carbon-oxygen bond recombination on the planar surface (180 kJ/mol). The free activation energy for methane dissociation is typically higher than that for water dissociation. Thus, methane dissociation can be expected to be rate

controlling. The reaction rate increases uniformly with particle size decrease. The second regime occurs at lower temperature and involves free activation energies for methane dissociation between 90 and 180 kJ/mol. The former value is the barrier for the CO bond formation on the Rh(211) surface. The latter one is the barrier for CO bond formation on the Rh(111) terrace. If the metal particles are large enough to support “B5” sites [17,23], for which the Rh(211) step is a model, C-O bond formation is fast and methane dissociation will remain the rate determining step. However, particles below a certain size do not support “B5” sites and, for this particular case, CH + O recombination reactions become rate limiting. In such a case, we expect to find a different particle size effect. The overall rate of the reaction will decrease when the particle size has decreased below a certain particle size limit, because C-O bond formation will become rate limiting for smaller particles. For large particles, methane dissociation remains rate limiting. Geometric considerations predict such an optimum in the reaction rate for metal particles of about 2.5 nm [17,23].

In the third regime, the free activation energy of methane and water dissociation are lower than 90 kJ/mol. This regime pertains to relatively low reaction temperatures. Now C-O bond formation is rate controlling for all particle sizes. If the metal particles become too small to support “B5” sites, the overall activity of the catalyst will significantly decrease due to an increase of the activation energy for CO formation from 90 to 180 kJ/mol.

The experimentally observed relation between the SMR reaction rate and particle size for Rh catalysts [11] indicates that the first regime applies to these catalysts. Note however that the smallest particles evaluated in the study of Jones et al. [11] is ~4 nm, which is above the geometric limit suggested to stabilize “B5” sites [17,23]. Although the other two regimes do not apply to SMR, they may be relevant for the steam reforming of higher hydrocarbons with more reactive CH bonds.

To deduce which metal will be most reactive for methane production, it is useful inspect the elementary expression for the rate of CO production per surface atom on a uniform surface

$$d\theta_{CO}/dt = k_{\text{recombination}} \theta_C \theta_O$$

For simplicity, we assume in this expression carbon-oxygen bond formation through direct recombination of adsorbed carbon and oxygen atoms. This reaction rate has a maximum when the coverages with carbon (θ_C) and oxygen (θ_O) are equal and the two surface species are completely mixed on the surface. Critical values for the adsorption energies of carbon on a surface are 600 kJ/mol for methane (this value equals the standard enthalpy of formation of

methane augmented by the sublimation energy of carbon to the gas phase) and of oxygen to decompose water and carbon dioxide are 480 and 520 kJ/mol, respectively. For comparison, the critical adsorption energy of oxygen for O₂ dissociation is low and only 250 kJ/mol (half the bond energy of molecular oxygen). In Table 10a, calculated adsorption energies of atomic O on the (111) surfaces of the various metals are collected. Pd, Pt, and Ir and the group IB metals are not capable of dissociating water. Rh forms a borderline case. However, note that the accuracy of the calculations is not better than 10 kJ/mol and that we only compare the least reactive surfaces. Moreover, in our recent study [10], we computed a slightly higher adsorption energy of oxygen with an improved functional. The higher stability of CO₂ makes not only Rh but also Ni less reactive for CO₂ reforming of CH₄. There is no restriction to the use of group VIII metals when methane is reformed by partial oxidation. Jones *et al.* [11] provide a comparison of the reactivity for SMR of the different metals. Ru and Rh are the most reactive.

Table 10b compares the computed activation energies for methane activation on the respective (111) surfaces of the group VIII metals [43]. Rh and Ir show the lowest activation energies for methane activation. This is in line with the high reactivity of Rh. Ir has a low reactivity in SMR because of low reactivity with respect to the dissociation of water. Pd also has a low reactivity, because the coverage with oxygen will be too low. Ru and Rh are the most active metals, because they provide the optimum compromise between relatively low barriers for methane activation and reasonable oxygen coverage. Ni and Co are less reactive, because methane dissociation is most difficult, notwithstanding their high reactivity with oxygen. Thus, there is a qualitative agreement of the reactivity order of transition metals for SMR with the analysis of microkinetic simulations by Jones *et al.* [11] This kinetic simulation, which compares the reactivity of different metals, is based on parameters that have been deduced using BEP relations and scaling laws. Only then the proper ranking is found when differences in trends as a function of adsorbed C and O energies are included.

Interestingly, a very different reactivity order is predicted for partial oxidation of methane toward carbon monoxide. In this case, in addition to methane activation, the rate of water removal from the surface becomes a limiting factor. In such case, over oxidation of the metal has to be prevented. Whereas the activation energy for methane activation is lower on Rh than on Pt [59], Pt is preferred for partial oxidation of methane because oxygen is more readily hydrogenated on Pt. In this case, Ir is also an attractive metal, because similar to Pt oxygen dissociation proceeds very easily.

Table 10. DFT calculated binding energy (kJ/mol) [43] for atomic carbon (a) and atomic oxygen (b) on the most dense surface of selected metals. A: Based on the critical adsorption energies of CH₄ (600 kJ/mol) and CO₂ (520 kJ/mol) some metals can be excluded (grey) as potential metal SMR catalysts. B: Based on the critical adsorption energies of H₂O (480 kJ/mol) some metals can be excluded (grey) as potential metal SMR catalysts. Rhodium is on the threshold of this barrier.

a)				b)			
Fe (hcp)	Co	Ni	Cu	Fe (hcp)	Co	Ni	Cu
-769	-668	-629	-476	-714	-550	-496	-429
Ru	Rh	Pd	Ag	Ru	Rh	Pd	Ag
-688	-690	-645	-338	-557	-469	-382	-321
Os	Ir	Pt	Au	Os	Ir	Pt	Au
-696	-675	-657	-411	-533	-428	-354	-270

4.4. Conclusions

Three different reaction pathways toward CO formation from adsorbed CH and O as relevant to methane steam reforming were investigated by quantum-chemical density functional theory (DFT) calculations for planar and stepped Rh surfaces. The conventional pathway, which requires CH dissociation prior to CO recombination, is in competition with the pathway involving a formyl (CHO) species. This result holds for both planar and stepped surfaces. The energy barriers for CO formation are 180 and 90 kJ/mol, respectively. Consequences of this difference in reactivity for particle size dependence of the steam reforming reaction are discussed. Because of the relatively high temperature of methane steam reforming, the activation free energy of methane is higher than that of the recombination reactions to form the C-O bond. The particle size dependence observed experimentally therefore follows the changes in the activation of methane. This is due to the increase of edge and corner sites with decreasing particle size. When C-O bond formation would have been rate controlling, a maximum in the rate of the methane steam reforming reaction as a function of decreasing particle size would have been predicted. Periodic trends in the adsorption energies of carbon and oxygen are quite different. Because adsorbed oxygen is needed for the reaction of the adsorbed CH intermediate to give CO, the metal with the lowest barrier for methane activation (Ir) is not the metal with the highest reactivity in the methane steam reforming reaction (Ru).

4.5. Acknowledgments

This work has been carried out with financial support from SenterNovem. Financial support for supercomputing facilities was provided by the National Computational Facilities Foundation of The Netherlands Organization for Scientific Research (NWO-NCF). The authors thank E. A. Pidko for providing the artwork for the Table of Contents image.

4.6. References

- [1] J.R. Rostrup-Nielsen, J. Sehested, J.K. Nørskov, *Adv. Catal.* 47 (2002) 65.
- [2] D. Hildebrandt, D. Glasser, B. Hausberger, B. Patel, B. Glasser, *Science* 323 (2009) 1680.
- [3] C.H. Bartholomew, R.J. Farrauto, *Fundamentals of Industrial Catalytic Processes*, 2nd ed.; Wiley: Hoboken, NJ, USA; 2006.
- [4] J.M. Wei, E. Iglesia, *J. Phys. Chem. B* 108 (2004) 4094.
- [5] J.R. Rostrup-Nielsen, J.-H. Bak Hansen, *J. Catal.* 144 (1993) 38.
- [6] J.M. Wei, E. Iglesia, *Angew. Chem., Int. Ed.* 43 (2004) 3685.
- [7] J.M. Wei, E. Iglesia, *J. Phys. Chem. B* 108 (2004) 7253.
- [8] J.M. Wei, E. Iglesia, *J. Catal.* 255 (2004) 116.
- [9] J.M. Wei, E. Iglesia, *Phys. Chem. Chem. Phys.* 6 (2004) 3754.
- [10] P.W. van Grootel, E.J.M. Hensen, R.A. van Santen, *Surf. Sci.* 603 (2009) 3275.
- [11] G. Jones, J.G. Jakobsen, S.S. Shim, J. Kleis, M.P. Andersson, J. Rossmeisl, F. Abild-Pedersen, T. Bligaard, S. Helveg, B. Hinnemann, J.R. Rostrup-Nielsen, I. Chorkendorff, J. Sehested, J.K. Nørskov, *J. Catal.* 259 (2008) 147.
- [12] M. Maestri, D.G. Vlachos, A. Beretta, G. Groppi, E. Tronconi, *J. Catal.* 259 (2008) 211.
- [13] O.R. Inderwildi, S.J. Jenkins, D.A. King, *J. Am. Chem. Soc.* 129 (2007) 1751.
- [14] B.S. Bunnik, G.J. Kramer, *J. Catal.* 242 (2006) 309.
- [15] Z.-P. Liu, P. Hu, *J. Am. Chem. Soc.* 125 (2003) 1958.
- [16] H.S. Bengaard, J.K. Nørskov, J. Sehested, B.S. Clausen, L.P. Nielsen, A.M. Molenbroek, J.R. Rostrup-Nielsen, *J. Catal.* 209 (2002) 365.
- [17] R.A. van Santen, *Acc. Chem. Res.* 42 (2009) 57.
- [18] R.A. van Santen, M. Neurock, S.G. Shetty, *Chem. Rev.* 110 (2010) 2005.
- [19] J.-F. Paul, P. Sautet, *J. Phys. Chem. B* 102 (1998) 1578.
- [20] F. Abild-Pedersen, O. Lytken, J. Engbæk, G. Nielsen, I. Chorkendorff, J.K. Nørskov, *Surf. Sci.* 590 (2005) 127.
- [21] I.M. Ciobica, R.A. van Santen, *J. Phys. Chem. B* 107 (2003) 3808.

- [22] A. Michaelides, Z.-P. Liu, C.J. Zhang, A. Alavi, D.A. King, P. Hu, *J. Am. Chem. Soc.* 125 (2003) 3704.
- [23] R. van Hardeveld, A. van Montfoort, *Surf. Sci.* 4 (1966) 396.
- [24] I.M. Ciobica, R.A. van Santen, *J. Phys. Chem. B* 106 (2002) 6200.
- [25] S. Shetty, A.P.J. Jansen, R.A. van Santen, *J. Am. Chem. Soc.* 131 (2009) 12874.
- [26] M.P. Andersson, F. Abild-Pedersen, I.N. Remediakis, T. Bligaard, G. Jones, J. Engbæk, O. Lytken, S. Horch, J.H. Nielsen, J. Sehested, J.R. Rostrup-Nielsen, J.K. Nørskov, I. Chorkendorff, *J. Catal.* 255 (2008) 6.
- [27] O.R. Inderwildi, S.J. Jenkins, D.A. King, *J. Am. Chem. Soc.* 129 (2007) 1751.
- [28] O.R. Inderwildi, S.J. Jenkins, D.A. King, *Angew. Chem., Int. Ed.* 47 (2008) 1.
- [29] G. Jones, T. Bligaard, F. Abild-Pedersen, J.K. Nørskov, *J. Phys.: Condens. Matter* 20 (2008) 064239.
- [30] G.A. Somorjai, *Philos. Trans. R. Soc. London, Ser. A* 318 (1986) 81.
- [31] G.A. Somorjai, *Introduction to Surface Chemistry and Catalysis*; John Wiley & Sons: New York, 1994.
- [32] S. Dahl, A. Logadottir, R.C. Egeberg, J.H. Larsen, I. Chorkendorff, E. Törnqvist, J.K. Nørskov, *Phys. Rev. Lett.* 83 (1999) 1814.
- [33] K. Honkala, A. Hellman, I.N. Remediakis, A. Logadottir, A. Carlsson, S. Dahl, C.H. Christensen, J.K. Nørskov, *Science* 307 (2005) 555.
- [34] G.-C. Wang, S.-X. Tao, X.-H. Bu, *J. Catal.* 244 (2006) 10.
- [35] G. Kresse, J. Furthmüller, *Comput. Mater. Sci.* 6 (1996) 15.
- [36] G. Kresse, J. Furthmüller, *Phys. Rev. B* 54 (1996) 11169.
- [37] J.P. Perdew, J.A. Chevary, S.H. Vosko, K.A. Jackson, M.R. Pederson, D.J. Singh, C. Fiolhais, *Phys. Rev. B* 46 (1992) 6671.
- [38] P.E. Blöchl, *Phys. Rev. B* 50 (1994) 17953.
- [39] G. Kresse, J. Joubert, *Phys. Rev. B* 59 (1999) 1758.
- [40] H.J. Monkhorst, J.D. Pack, *Phys. Rev. B* 13 (1976) 5188.
- [41] G. Henkelman, B.P. Uberuaga, H. Jónsson, *J. Chem. Phys.* 113 (2000) 9901.
- [42] P. Atkins, J. De Paula, *Atkins' Physical Chemistry*, 8th ed.; Oxford University Press: Oxford, 2006.
- [43] R.A. van Santen, M. Neurock, *Molecular Heterogeneous Catalysis*, 1st ed.; Wiley-VCH: Weinheim, Germany, 2006.
- [44] D. Loffreda, F. Delbecq, F. Vigne, P. Sautet, *Angew. Chem., Int. Ed.* 48 (2009) 8978.
- [45] T. Bligaard, J.K. Nørskov, S. Dahl, J. Matthiesen, C.H. Christensen, J. Sehested, *J. Catal.* 224 (2004) 206.
- [46] N. Brønsted, *Chem. Rev.* 5 (1928) 231.
- [47] M.G. Evans, N.P. Polanyi, *Trans. Faraday Soc.* 34 (1938) 11.

- [48] B.S. Bunnik, G.-J. Kramer, R.A. van Santen, *Top. Catal.* 53 (2010) 403.
- [49] H.L. Abbott, I. Harrison, *J. Catal.* 254 (2008) 27.
- [50] R.M. Watwe, H.S. Bengaard, J.R. Rostrup-Nielsen, J.A. Dumesic, J.K. Nørskov., *J. Catal.* 189 (2000) 16.
- [51] S.-G. Wang, D.-B. Cao, Y.-W. Li, J. Wang, H. Jiao, *J. Phys. Chem. B* 110 (2006) 9976.
- [52] K.M. DeWitt, L. Valadez, H.L. Abbott, K.W. Kolasinski, I. Harrison, *J. Phys. Chem. B* 110 (2006) 6705.
- [53] A. Kokalj, N. Bonini, C. Sbraccia, S. de Gironcoli, S. Baroni, *J. Am. Chem. Soc.* 126 (2004) 16732. [54] R.C. Egeberg, S. Ullmann, I. Alstrup, C.B. Mullins, I. Chorkendorff, *Surf. Sci.* 497 (2002) 183.
- [55] A. Michaelides, A. Alavi, D.A. King, *J. Am. Chem. Soc.* 125 (2003) 2746.
- [56] Y. Cao, Z.-X. Chen, *Surf. Sci.* 600 (2006) 4572.
- [57] M. Pozzo, G. Carlini, R. Rosei, D. Alfe, *J. Chem. Phys.* 126 (2007) 164706.
- [58] A.A. Phatak, W.N. Delgass, F.H. Ribeiro, W.F. Schneider, *J. Phys. Chem. C* 113 (2009) 7269.
- [59] L.D. Schmidt, et al.; *Science* 259 (2009) 343.

Chapter 5: CH₄ dissociation on high and low indices Rh surfaces¹

We present DFT calculations of the energetics of the elementary reaction steps in the dehydrogenation of CH₄ to C on extended Rh(111) and Rh(211) surfaces, which are compared to values for these reaction steps on a planar (111) surface and the edge atoms that are shared between two (111) facets of a nanorod model. The adsorption energies between comparable surfaces of the extended and nanorod models are very similar. Only C adsorbs significantly stronger on the planar surface of the nanorod model than on the extended (111) surface due to the involvement of more reactive edge atoms. Also the reaction energies between the two types of surface models are very similar. The small differences in reaction and activation energies are largely due to small geometrical differences. In all cases, CH dissociation has the highest activation barrier. However, dissociative CH₄ adsorption is rate controlling under typical steam reforming conditions because of the entropy loss associated with methane adsorption. The barrier for CH₄ dissociation significantly decreases with a decrease of the coordination number of the surface metal atoms. Accordingly, the corrugated surfaces are more reactive for methane dissociation than the planar ones.

¹ This chapter has been published as “Methane Dissociation on High and Low Indices Rh Surfaces” by P.W. van Grootel, R.A. van Santen and E.J.M. Hensen in Journal of Physical Chemistry C 115 (2011) 13027-13034.

5.1. Introduction

Steam methane reforming is the principle reaction for the production of synthesis gas and hydrogen [1]. Synthesis gas is a key intermediate in the chemical industry for production of a wide range of higher value fuels and chemicals such as methanol and clean synthetic diesel and gasoline via Fischer-Tropsch synthesis (FTS) [2,3]. Hydrogen is primarily used for the synthesis of ammonia and for hydrogenation purposes in petroleum refineries [1]. Ni is the preferred transition metal for steam methane reforming (SMR) [4,5]. Besides Ni, a number of other transition metals exhibit high catalytic activity in SMR, most notably Rh and Ru [6-8].

SMR requires the complete dissociation of methane to carbon with carbon monoxide being the principle product besides hydrogen. In recent years, the complete pathway for CH₄ dissociation has been computed by DFT for metals such as Ni [9-11], Pt [12], Ru [12-14] and Rh [12,15,16]. Although many studies have focused on close-packed surfaces, it is by now clear that corrugated surfaces are more reactive [17-19]. Depending on the nature of the elementary reaction step, the coordination number of the surface metal atoms and the occurrence of special surface topologies such as step edge sites affect the reaction rate [20]. Our recent studies have addressed the influence of the surface topology on the dissociation of water [21] and C-O recombination [22], two other critical steps in the reaction mechanism of steam reforming. In these works we investigated Rh(111) and Rh(211) surfaces. Rh was chosen, because it is one of the most active metals for SMR [6,23-28]. Further focusing on Rh surfaces, we found in literature that the complete dehydrogenation of CH₄ to C on rhodium has only been investigated for a Rh(111) surface [16]. An important corollary of this and related studies for other metals is that CH₄ and CH dissociation are candidate rate limiting steps. Typically, CH dissociation is more difficult than the initial methane activation step. Hu and Liu [19] found that the activation barrier of CH₄ dissociation decreases significantly with a decrease of the surface metal atom coordination number. We have earlier determined that CH dissociation is preferred over Rh(211) as compared to Rh(111) [22]. Despite these studies, there is no comparison of the complete CH₄ dissociation to C on planar and stepped surfaces of Rh. To counter this, we carried out a minimum energy path analysis for the stepwise dissociation of CH₄ to C. Besides periodic models of Rh(111) and Rh(211) surfaces, we included a nanorod model earlier explored by Van Steen and co-workers [29]. The latter calculations serve the purpose to establish whether particular edge atoms, which occur between the facets of nanoparticles have any particular properties in the methane

dissociation mechanism. Similar to the stepped surface topologies, these edge atoms have also lower coordination number than the planar surfaces. The geometry of the edge sites of such a nanorod model is different from that of a step edge site.

This paper is organized in the following manner. The dissociation of methane to carbon and hydrogen is compared for a Rh(111) planar surface, a stepped Rh(211) surface, a Rh(111) planar surface on a nanorod model and the edge atoms between two Rh(111) surfaces of the nanorod model. The computations of the Rh(111) surface are the same as reported in Bunnik and Kramer [16] with the exception that a larger $p(3 \times 3)$ supercell was employed. The Rh(211) surface presents a model for step edges containing surface atoms with a lower coordination number (7) than the surface atoms in the planar (111) surface (9). Methane dissociation is considered on the edge atoms between two (111) facets with a coordination number of 7, similar to that of the step edge atoms of the Rh(211) model. For comparison, we also studied methane dissociation on the (111) facet of such a nanorod model.

5.2. Methods

The quantum-chemical calculations were carried out using the Vienna Ab Initio Simulation Package (VASP) [30,31] using the gradient-corrected PW91 exchange-correlation functional [32]. The projected-augmented wave (PAW) method [33,34] was used to describe electron-ion interactions. A plane wave basis set was employed for the valence electrons. The energy cut-off was set at 400 eV. Computations were performed with $3 \times 3 \times 1$ k -point sampling of the Brillouin zone (11 k -points) [35]. The third vector is perpendicular to the surface. The relaxation of the electronic degrees of freedom was assumed to be converged, when the total energy and the band structure energy changes between two electronic optimization steps were both smaller than 10^{-5} eV. Forces below 10^{-3} eV/Å for all ions were used as the criterion for convergence of ionic relaxation. The choices for the number of k -points, the plane-wave cut-off energy and the size of the vacuum are generally comparable to literature works that will serve as reference [16,19].

Adsorption energies (ΔE_{ads}) were calculated from the energy difference between the surface containing the geometry optimized adsorbate ($E_{\text{surface} + \text{adsorbate}}$) and the same surface with the adsorbing molecule placed in the middle of an empty box ($E_{\text{surface}} + E_{\text{adsorbing molecule}}$)

$$\Delta E_{\text{ads}} = E_{\text{surface} + \text{adsorbate}} - (E_{\text{surface}} + E_{\text{adsorbing molecule}}).$$

For determining the transition state of reaction pathways, the Climbing Images Nudged Elastic Band-method (CI-NEB) [36] was employed. The initial, final and transition state geometries were tested by analyzing the harmonic normal modes, which were calculated by using the finite difference method as implemented in VASP. Small displacements (0.02 \AA) of adsorbed atoms and the three relaxed surface layers were used for the estimation of numerical Hessian matrix. The energy of each state was corrected for the zero point energy [37], determined using the results of the normal mode analysis.

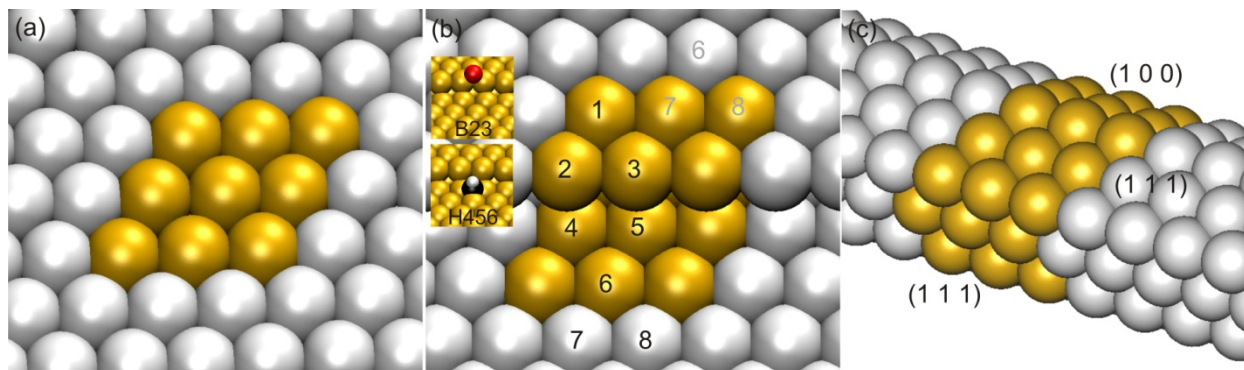


Figure 1. Representation of the three Rh surfaces employed in the present work: (a) Rh(111), (b) Rh(211) and (c) the nanorod model. The yellow atoms represent the unit cell.

The models employed in this study are depicted in Figure 1. The Rh(111) model consists of a periodic $p(3 \times 3)$ unit cell containing five layers of Rh atoms in an *fcc* arrangement and a vacuum of 13 \AA . The resulting surface consists of close packed atoms. The layering gives rise to two kind of hollow sites, an *hcp* hollow site having a neighbouring Rh atom directly located in the subsurface second layer and an *fcc* hollow site that does not contain a subjacent metal atom. This super cell contains 45 Rh atoms. The coordination number of the surface Rh atoms is 9. Four symmetric adsorption sites can be distinguished on the terrace surface. Besides the two three-fold hollow sites (*hcp* and *fcc*), the surface contains top and bridge sites.

The Rh(211) surface contains (111) terraces and a (100) oriented monoatomic step. The geometry of the terrace is the same as that of the planar Rh(111) surface. The number of layers in this model is six and the super cell contains 66 Rh atoms. The coordination numbers of the terrace and step edge surface atoms are 9 and 7, respectively. The coordination number of the atoms at the bottom of the step is 11. The stepped surface leads to a large number of potential adsorption sites. Fourteen symmetric sites are considered as adsorption sites of interest and are denoted in Figure 1b in which *H*, *B* and *T* stand for hollow, bridge and top sites.

The Rh nanorod model was constructed on the basis of the method presented by Van Steen and co-workers [29] by cutting a bulk *fcc* structure in such way that a octahedron morphology is obtained with (111) and (100) surfaces. The nanorod has four (111) and two (100) facets. In this particular model the edge atoms between the various facets have a coordination number of 7. The surface coordination number of the metal atoms in the (111) surface is 9 and those in the (100) surface 8, similar to the corresponding extended surfaces. The width of the rod is three layers. Each layer contains 7 atoms with a coordination number of 12, 6 surface atoms with a coordination number of 9 and 6 surface atoms with a coordination number of 7. Methane dissociation to carbon and hydrogen has been studied on (i) the (111) facet of the Rh nanorod and (iii) the edge atoms between two (111) facets denoted by Rh-rod(111) and Rh-rod(111)-(111), respectively.

The vacuum space above all slab models was chosen to be at least 13 Å and the minimal distance between two instances of the nanorod is 15 Å. Larger separation distances between the slabs in periodic images did not lead to a significantly lower energy. The top three layers of the slab supercells and all but the single middle row of atoms of the nanorod model were allowed to relax during energy optimizations. No symmetry restrictions were imposed. For several reaction pathways, it was confirmed that dipole corrections were not required.

5.3. Results and discussion

5.3.1. Adsorption of CH_x and H fragments

Table 1 reports the most stable adsorption energies of the CH_x ($x = 0-3$) and H fragments on the various surfaces. The stable adsorption geometries reported by Bunnik and Kramer [16] were employed as starting geometries for optimizations of the adsorbates on the Rh(111) and Rh-rod(111) surfaces.

The adsorption energies of the various adsorbates on the Rh(111) surface are significantly higher than the values reported by Bunnik and Kramer [16]. This is due to the choice of a larger unit cell size, *i.e.* $p(3 \times 3)$, in the current work as compared to $p(2 \times 2)$ employed in Ref. [16]. The larger unit cell size results in a lower surface coverage (0.11 ML) and, accordingly, in lower repulsion energies between the images. The adsorption energy increases going from CH₃ to C due to the larger number of free valence electrons upon a decrease of the number of H atoms. Generally speaking, the differences in the adsorption energies of CH₃, CH₂ and CH between Rh(111) and Rh-rod(111) are negligible. The *fcc* site is the preferred adsorption site

for CH₃, while CH₂ and CH prefer to be adsorbed in the *hcp* site with only small differences between *hcp* and *fcc* sites in all cases. The C atom also prefers to adsorb in a *hcp* site and in this case it is seen that the C adsorption energy on Rh-rod(111) is somewhat higher than on Rh(111). The adsorption of H on both surfaces is very similar.

Table 1. Adsorption energies and sites of CH_x (x = 0-3) and H on the various surface models.

Surface	CH ₃	CH ₂	CH	C	H
Rh(111)	263 (fcc)	496 (hcp)	730 (hcp)	848 (hcp)	272 (fcc)
Rh(111) [16]	179 (fcc)	419 (hcp)	651 (hcp)	690 (hcp)	275 (fcc)
Rh-rod(111)	268 (fcc)	496 (hcp)	727 (hcp)	867 (hcp)	270 (fcc)
Rh(211)	294 (BU23)	505 (BU23)	734/723 (HU123/HD123)	8881/851 (HU123/HD123)	273 (BU23)
Rh-rod(111)-(111)	284 (B)	510 (B)	663 (B)	802 (B)	269 (B)

¹ The preferred adsorption site for carbon is the H2345 site with an adsorption energy of 813 kJ/mol.

When a similar comparison is made for the two corrugated surface, it is noticed that the adsorption energies for CH₃ and CH₂ are again very similar for Rh(211) and Rh-rod(111)-(111) with a preference for the bridged site. It is not meaningful to compare the results of CH and C adsorption on both surfaces, because the adsorption sites are different: CH and C are preferentially adsorbed on the three-fold hollow site on the Rh(211) surface, whereas they prefer two-fold binding on Rh-rod(111)-(111). Note that the adsorption energies for the three-fold sites on Rh(211) are quite similar to those found for Rh-rod(111). The adsorption energies on the corrugated surfaces are obviously higher than on the planar surfaces as they should be because of the lower metal-metal coordination numbers of the former surfaces. The surface atoms of Rh(211) and Rh-rod(111)-(111) have seven neighbours, while those of Rh(111) and Rh-rod(111) have nine.

5.3.2. Methane dissociation on Rh(111) and Rh-rod(111)

The stepwise dissociation of methane to carbon and hydrogen was first investigated for the Rh(111) and Rh-rod(111) surfaces. Figure 2 compares the minimum energy paths for methane dehydrogenation on these surfaces with the one for Rh(111) reported earlier [16].

The corresponding reaction energies and activation barriers for the dehydrogenation of methane are collected in Table 2. The geometries of the initial, transition and final state for the four elementary reaction steps are depicted in Figure 3. The minimum energy path involves CH_3 , CH_2 and CH on *fcc*, *fcc* and *hcp* sites, respectively. The product C adatom is located on a *hcp* site and the four H atoms on *fcc* sites. Each dissociation step of a CH_x fragment ends with co-adsorbed CH_{x-1} and H fragments. The next step starts by diffusing the H atom to infinite distance. This assumes the presence of sufficient adsorption sites and fast diffusion of H atoms [16]. The initial surface coverage in the present study (0.11 ML) is lower than the one (0.25 ML) employed in the study of Bunnik and Kramer. This results in lower repulsion between the images and translates into increasingly lower energies of the total system ($\text{CH}_{4-x} + x \text{H}$) as a function of the reaction coordinate. Consequently, the total reaction energies for methane dehydrogenation are -206 and -225 kJ/mol, respectively, for Rh(111) and Rh-rod(111) as compared to a value of -28 kJ/mol reported before.

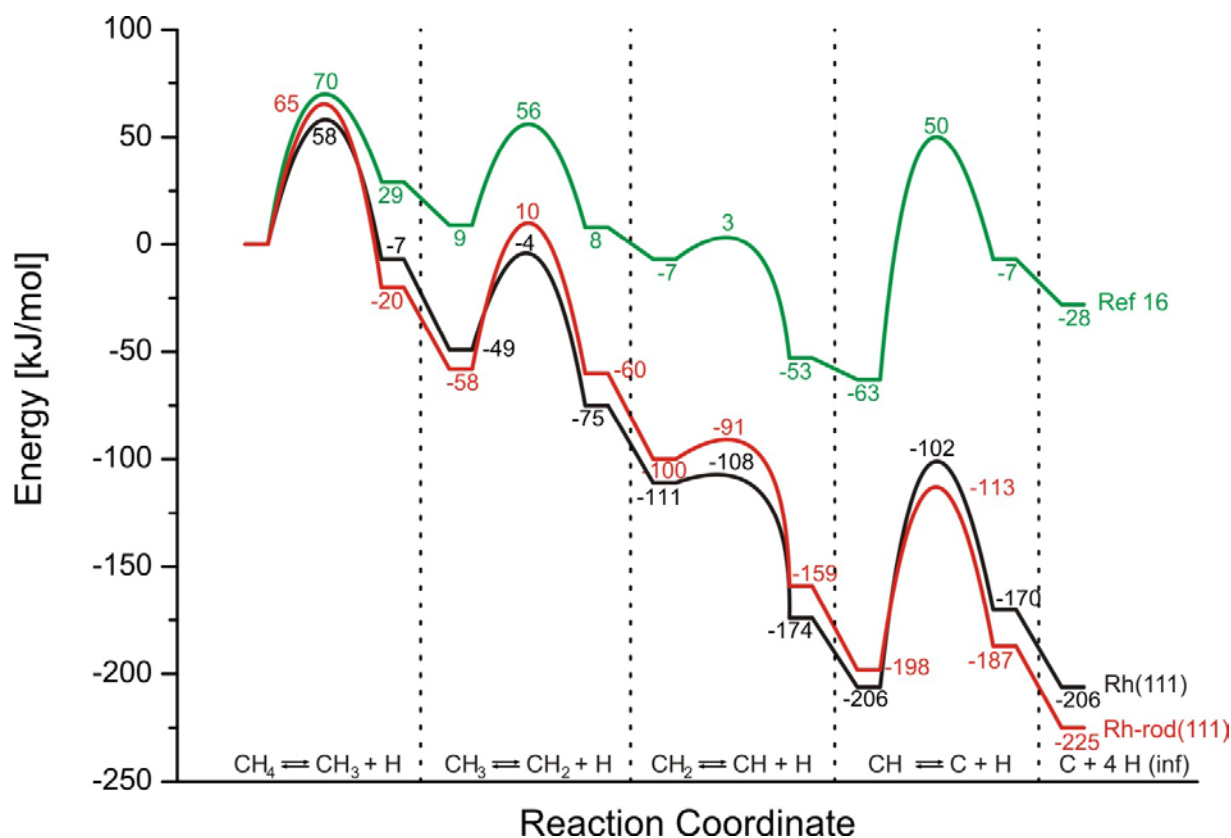


Figure 2. Potential energy diagram (energies in kJ/mol) for the dehydrogenation of CH_4 to C and 4 H on planar Rh(111) surfaces: (black) periodic Rh(111) surface, (red) Rh-rod(111) and (green) periodic Rh(111) surface by Bunnik et al. [16]. The large difference between the present results for the periodic Rh(111) and literature is due to the choice of a larger unit cell, which results in decreased repulsive interactions.

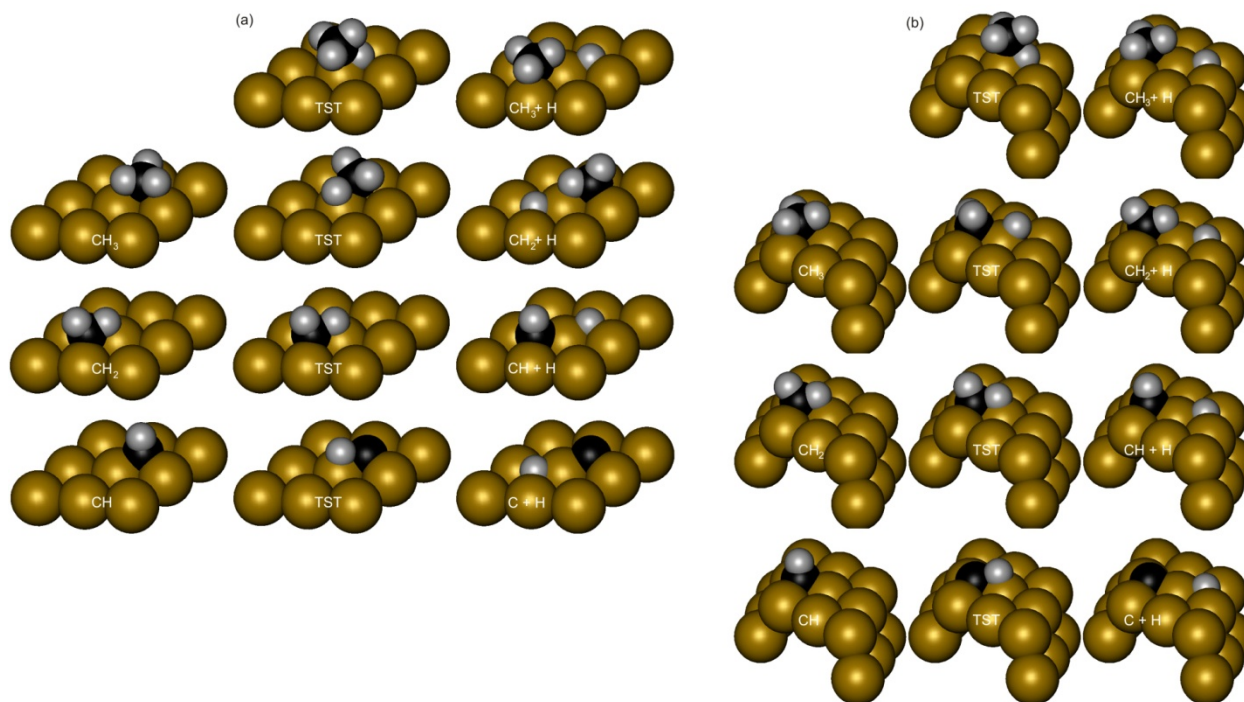


Figure 3. Full dehydrogenation of CH_4 on the planar surfaces (a) Rh(111) and (b) Rh-rod(111) with carbon and hydrogen atoms in black and white, respectively. Shown are the initial state (left), transition state (middle), and final state (right).

Table 2. Reaction energies and activation barriers for dehydrogenation of CH_4 to C for various surface models.

	E_{act} (kJ/mol)					E_{react} (kJ/mol)				
	Rh(111)	Rh(111) [16]	Rh-rod(111)	Rh(211)	Rh-rod(111)-(111)	Rh(111)	Rh(111) [16]	Rh-rod(111)	Rh(211)	Rh-rod(111)-(111)
$\text{CH}_4 \rightarrow \text{CH}_3^* + \text{H}^*$	58	70	65	35	42	-7	20	-20	-40	-26
$\text{CH}_3^* \rightarrow \text{CH}_2^* + \text{H}^*$	45	47	68	60	30	-26	0	-2	-12	-16
$\text{CH}_2^* \rightarrow \text{CH}^* + \text{H}^*$	3	10	9	25	$69^1/32^2$	-63	-45	-59	-63	$38^1/14^2$
$\text{CH}^* \rightarrow \text{C}^* + \text{H}^*$	104	113	85	$78^3/76^4$	90	36	36	11	$24^3/-2^4$	16

¹ CH product adsorbed on bridge site on edge of the Rh-rod;

² CH product adsorbed in three-fold hollow site behind the edge on the Rh(111) surface;

³ Initial CH adsorbed on top terrace of Rh(211) surface;

⁴ Initial CH adsorbed on lower terrace of Rh(211) surface.

5.3.3. The $\text{CH}_4^* \rightarrow \text{CH}_3^* + \text{H}^*$ reaction step

Dissociation of methane occurs over a single Rh atom. In the transition state the methyl fragment is slightly tilted and the H atom moves over the top of the Rh atom. The final state contains the CH_3^* and H^* fragments in *fcc* sites. One of the H atoms of the methyl group is

tilted slightly upwards on the Rh-rod(111) surface. The activation energies of this step are calculated to be 58 and 65 kJ/mol for the Rh(111) and Rh-rod(111) surfaces. These values are similar to values of 65 kJ/mol [19] and 70 kJ/mol [16] reported before. The small difference in the final geometry of the methyl group leads to a slightly more exothermic reaction energy for methane dissociation on Rh-rod(111) as compared to Rh(111). Due to the lateral interactions between adsorbed CH₃ and H, the product of co-adsorbed methyl and hydrogen is less stable by 42 kJ/mol and 38 kJ/mol than the separately adsorbed fragments for the Rh(111) and Rh-rod(111), respectively.

5.3.4. The CH₃* → CH₂* + H* reaction step

Similar to Ru(0001) [14] and Rh(111) [16], the reaction of CH₃* preferably proceeds from the *fcc* site. The activation energies for Rh(111) and Rh-rod(111) amount to 45 and 68 kJ/mol, respectively. The former value is in good agreement with the value of 47 kJ/mol found by Bunnik et al. [16]. The higher barrier for dissociation on Rh-rod(111) can be related to the difference in CH₃ adsorption. The hydrogen atoms are pointing outwards from the rod and have to be brought closer to the surface over a larger distance as compared to case of dissociation of CH₃ over the planar surface. Hydrogen abstraction takes place over the top of a Rh surface atom and in both cases the final CH₂ is rotated to accommodate the two hydrogen atoms in a stable configuration. In this case, the energy for methyl dissociation is exothermic on the Rh(111) surface (-26 kJ/mol) and thermoneutral (-2 kJ/mol) for Rh-rod(111). The geometric difference of CH₃ dissociation mechanism over the extended and rod models leads to destabilization of the final state in case of Rh-rod(111) and, accordingly, to a higher activation energy.

5.3.5. The CH₂* → CH* + H* reaction step

The reaction energies for the dissociation of methylene are -63 and -59 kJ/mol with very low activation energies of 3 and 9 kJ/mol for the Rh(111) and Rh-rod(111) models, respectively. Dissociation occurs over the top of the Rh atom and results in the methyldyne in a three-fold hollow site. The activation energies are very low in agreement with the low barrier reported before for Rh(111) [16]. Due to the lower lateral interactions in our model, the value is negligible for Rh(111) and competes with diffusion of CH₂.

5.3.6. The $\text{CH}^* \rightarrow \text{C}^* + \text{H}^*$ reaction step

The activation barrier for dissociation of CH^* is significantly higher than for the other steps because of the perpendicular adsorption geometry. The C-H fragment has to bend over to the surface in order to dissociate. The values for the activation barrier are 104 kJ/mol and 85 kJ/mol for Rh(111) and Rh-rod(111), respectively. The value for Rh(111) is slightly lower than the one identified for the same surface with a smaller unit cell [16]. The reaction energy for the Rh(111) surface is higher than that for the Rh-rod(111) one, because the Rh-rod(111) surface bonds the C atom significantly stronger.

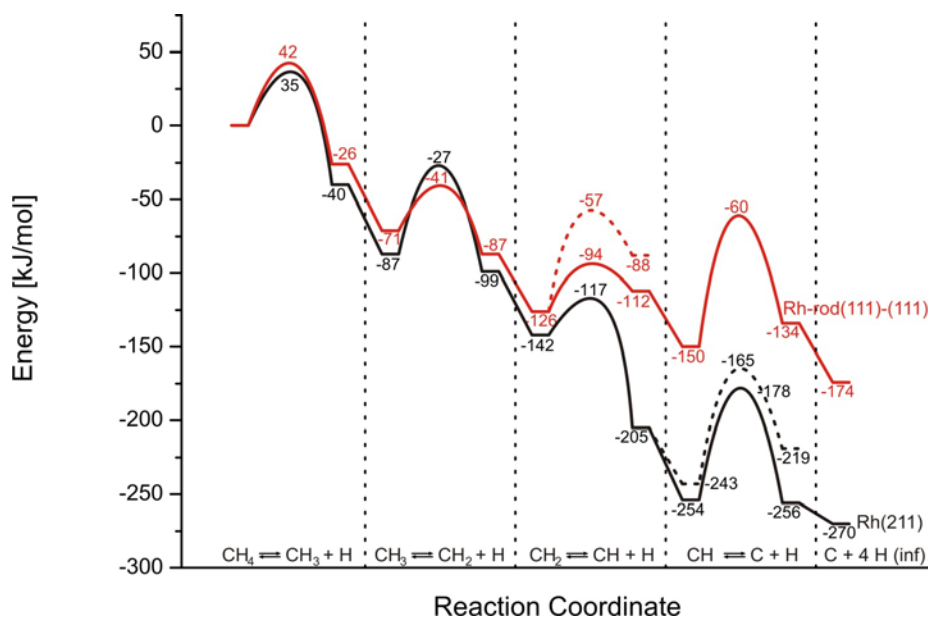


Figure 4. Potential energy diagram (energies in kJ/mol) for the dehydrogenation of CH_4 to C and 4 H on conjugated rhodium surfaces: (black) periodic Rh(211) surface and (red) Rh-rod(111)-(111).

5.3.7. Methane dissociation on Rh(211) and Rh-rod(111)-(111)

Figure 4 shows the minimum energy path for the dehydrogenation of methane over the stepped Rh(211) surface and the edge atoms between two (111) facets of the nanorod model. In both cases, the surface atoms have a coordination number of seven. Figure 5 shows the corresponding geometries of initial, transition and final states (the final state contains the co-adsorbed hydrogen). The total reaction energy for Rh(211) is -270 kJ/mol. The lower reaction energy as compared to Rh(111) and Rh-rod(111) is mainly due to the higher adsorption energy of carbon. Note that we have placed carbon in the H123 site as the final state, which is not the most stable geometry for C. Our earlier work [22] has shown that the most stable geometry for C is the site in the step (H2345). The total energy is -174 kJ/mol when the reaction takes place over the edge atoms of the nanorod. This involves CH and C in a bridged

configuration on the edge sites of the nanorod. As we have already computed the energetics of CH dissociation behind the edge [22], we have included this path to complete the full catalytic pathway toward C and H on the edge of the rod. These geometries were not considered for the Rh(211) surface.

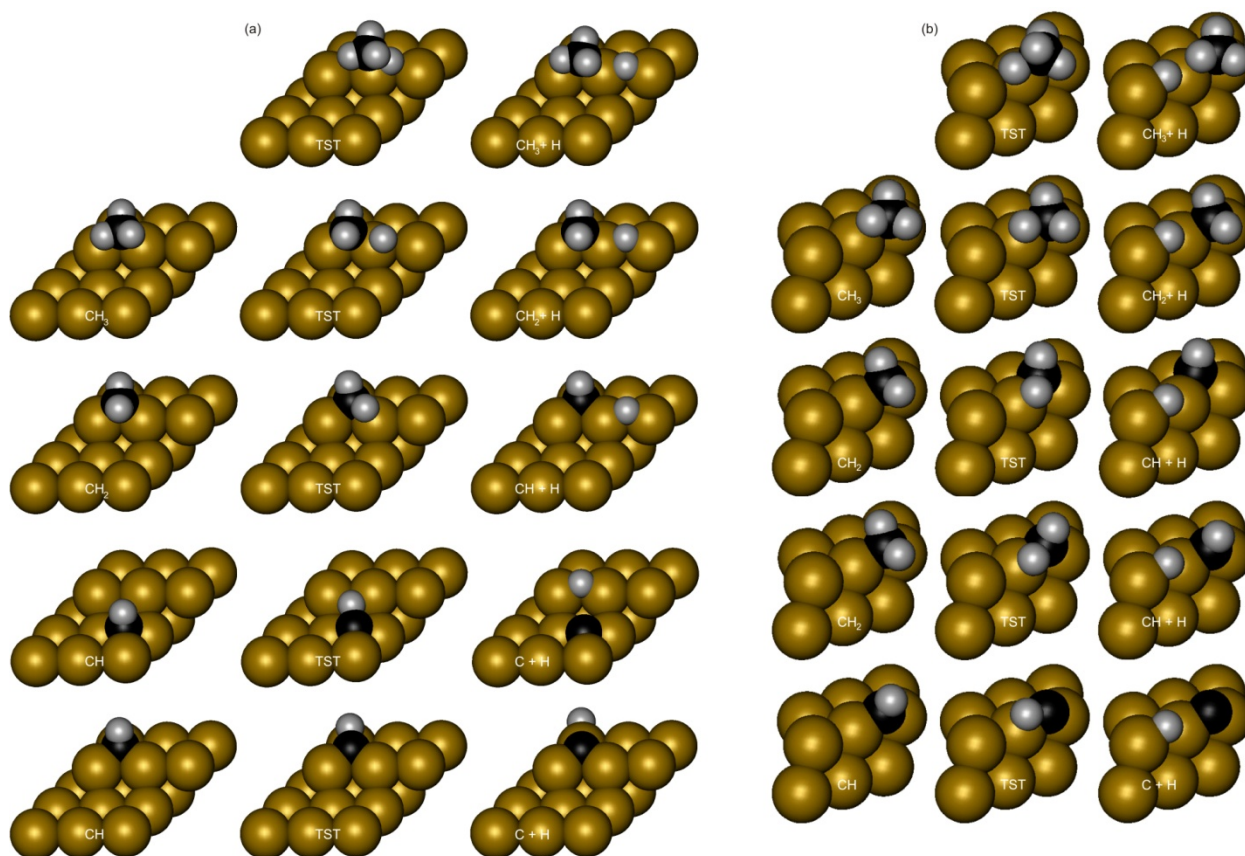


Figure 5. Full dehydrogenation of CH_4 on the conjugated surfaces (a) Rh(211) and (b) Rh-rod(111)-(111) with carbon and hydrogen atoms in black and white, respectively. Shown are the initial state (left), transition state (middle), and final state (right).

5.3.8. The $\text{CH}_4 \rightarrow \text{CH}_3^* + \text{H}^*$ reaction step

Dissociative methane adsorption on the stepped Rh(211) surface proceeds with an activation barrier of only 35 kJ/mol and a reaction energy of -40 kJ/mol. The barrier is significantly lower than on the planar surfaces considered above. The value is very close to the barrier of 31 kJ/mol reported for a stepped Rh(211) site by Liu and Hu [19]. The activation barrier of 42 kJ/mol and the reaction energy of -26 kJ/mol for methane dissociation are slightly higher on Rh-rod(111)-(111) than on Rh(211). The CH_3 product on Rh-rod(111)-(111) has one hydrogen oriented towards a neighbouring edge atom. This is the cause of the lower reaction energy and somewhat higher activation energy for methane dissociation.

5.3.9. The $\text{CH}_3^* \rightarrow \text{CH}_2^* + \text{H}^*$ reaction step

The subsequent dissociation of methyl to methylene proceeds with a barrier of 60 kJ/mol on the Rh(211) surface. This barrier is 15 kJ/mol higher than on the Rh(111) surface. The final geometry of methylene is in the bridge position, similar to the initial CH_3 adsorption geometry with the H atom adsorbed on an adjacent bridge site. The barrier for methyl dissociation is very low at 30 kJ/mol on the edge atoms of the nanorod model. This significant difference in the activation energy is related to the geometry of CH_3 adsorption of the methyl. The methyl is already in an activated state on the edge of the rod, whereas the CH_3 fragment has to rotate on the edge of the Rh(211) surface.

5.3.10. The $\text{CH}_2^* \rightarrow \text{CH}^* + \text{H}^*$ reaction step

Upon dissociation of methylene the CH fragment becomes adsorbed in the three-fold hollow site on the top terrace behind the bridge site to which CH_2 was initially adsorbed. The dissociation of CH_2 to CH and H proceeds with a relatively low barrier of 25 kJ/mol on Rh(211). This value is substantially higher than the value on the terrace. The large difference can be explained by comparing the transition states for CH_2 dissociation on Rh(111) and Rh(211). On the former surface, one of the C-H bonds of the CH_2 fragment is already oriented towards the top of a surface Rh atom, whereas the CH_2 on the stepped surface has to rotate before dissociation can occur. The adsorption energy of CH on the edge of Rh(211) is approximately 60 kJ/mol higher than on the threefold hollow site. This is already higher than the previously mentioned CH_2 dissociation energy of 25 kJ/mol [16]. The pathway for dissociation in which CH ends up in the two-fold bridge site is therefore not considered here. The CH_2 dissociation with CH finally adsorbed in the bridge site between two edge atoms of Rh-rod(111)-(111) has an activation and reaction energy of 69 kJ/mol and 38 kJ/mol, respectively, whereas the pathway in which CH ends up in the three-fold hollow site behind the edge has a barrier of 32 kJ/mol and a reaction energy of 14 kJ/mol. The latter pathway is favored. Its activation energy is comparable to that of Rh(211) as expected from the similarity of the reaction pathway.

5.3.11. The $\text{CH}^* \rightarrow \text{C}^* + \text{H}^*$ reaction step

Two different starting configurations are considered for methylenidene dissociation. The first one with CH initially on the three-fold site behind the step and the second one with CH in a

three-fold site on the bottom of the step of the Rh(211) surface. For the latter reaction, we assume, similar to Inderwildi [38], that CH diffuses with low barrier over the surface. The dissociation of CH for this case has been studied by us before [22]. Methylidene dissociation for these two initial states has a very similar activation barrier of around 76 kJ/mol. The reaction energy is -2 kJ/mol starting from CH in the three-fold position and 24 kJ/mol from CH on the terrace. The dissociation of CH adsorbed on the bridge position of Rh-rod(111)-(111) has a barrier of 90 kJ/mol. The product C and H are both adsorbed on the edge of the rod. The latter activation energy cannot be directly compared to the energies for Rh(211), because the reaction mechanism is different.

5.4. General discussion

The energetics (reaction energies and activation barriers) for the dissociation of CH₄ to C and 4 H have been computed for various surface models. The differences in the adsorption energies between Rh(111) and Rh-rod(111) and between Rh(211) and Rh-rod(111)-(111) are negligible, except for the adsorption of C. Similarly, the differences in the activation barriers can be explained by subtle geometrical differences in the transition and final states. The lower barrier for the CH* → C* + H* reaction on Rh-rod(111) as compared to Rh(111) is due to the stronger adsorption of C on the former surface. The dissociation barriers for CH dissociation between Rh-rod(111)-(111) and Rh(211) are different because of the difference in the geometries considered.

The highest activation barriers in methane dehydrogenation are those for CH₄, CH₃ and CH dissociation. Except for Rh(111), the activation barrier for CH₃ dissociation is close to that of methane dissociation. The barrier for CH₄ dissociation is higher on the terrace surfaces than on the surfaces that contain low-coordinated surface atoms in line with earlier results [19]. CH₄ dissociation occurs by C-H cleavage over a single Rh surface atom. As the transition state is late, the activation barrier is lower when the final products of C-H cleavage, CH₃ and H, are more strongly adsorbed. Their adsorption increases with decreasing coordination number of the surface metal atom. The small activation barrier differences between the extended and nanorod surfaces relate to differences in the reaction energies due to slightly different final states (mainly the location of H*). The barrier for CH* → C* + H* is highest in the dehydrogenation mechanism of CH₄ to C for all surfaces considered. In order to identify the rate controlling step in the overall mechanism, however, the free activation barriers should be compared. For the dissociative adsorption of CH₄ the entropy loss is

substantial (~ 130 J/mol.K [22]). In contrast, the surface dissociation reaction of CH does not involve a large change in entropy and, accordingly, the rate controlling step under typical reforming reaction conditions will be CH_4 dissociation for all surface models considered in this investigation.

In summary, the energetics of the dehydrogenation of methane to carbon on extended surface and nanorod models representing planar and corrugated surfaces are very similar. Differences in reaction and activation energies are largely due to small geometrical differences. The only significant deviation is the higher adsorption energy of C on the Rh-rod(111) model as compared to that of C on Rh(111). In an attempt to understand this difference in, we analysed the local density of states (LDOS) plots of the d -orbitals of the surface Rh atom involved in C adsorption (Figure 6). Two main parameters were derived from these LDOS plots, namely the average energy of the d -band

$$\bar{\epsilon} = \frac{\sum \epsilon_i w_i}{\sum w_i}$$

with w_i the occupancy of the energy level ϵ_i , and the average width of the d -band according to

$$\sigma = \sqrt{\frac{\sum |\bar{\epsilon} - \epsilon_i|^2 w_i}{\sum w_i}}$$

In general, the higher the d -band energy the higher the reactivity of the surface metal atom. Likewise, a decrease of the band width leads to a more reactive surface metal atom. Table 3 lists the values of the LDOS analysis for the surface atoms of the various models. Note that we considered only the edge atoms of the corrugated surfaces. As expected, $\bar{\epsilon}$ is shifted upwards for an edge atom of Rh(211) compared to the surface atoms in Rh(111) with the band width being smaller for the former surface in line with the higher reactivity of the surface atoms. This explains the significantly higher adsorption energy of C on Rh(211) than on Rh(111). These trends are very similar when comparing Rh-rod(111) and Rh-rod(111)-(111), although one cannot directly compare the C adsorption energies on these surface because of the different adsorption geometry of C on Rh-rod(111)-(111) (two-fold) as compared to Rh-rod(111) (three-fold). Note that a three-fold coordination of C on the former model would give the same adsorption geometry as three-fold coordination of C on Rh-rod(111). It is noteworthy that the two values for $\bar{\epsilon}$ for the nanorod model are lower than those for the extended surfaces because of the higher ionization potential associated with the model containing less Rh atoms (electrons are more localized). For completeness we have

also included the LDOS analysis of the surface atoms in the presence of adsorbed C. The differences are due to the interaction of the metal d -band with the C p -orbital perpendicular to the surface, which leads to a lower average energy and a wider d -band. Finally, the dominant reason that C adsorbs more strongly on Rh-rod(111) than on Rh(111) lies in the fact that in the latter case C is bonded to three surface Rh atoms with a coordination number of 9, whereas in the former C binds to only one surface atom with a coordination number of 9 and two with a coordination number of 7. The edge atoms are more reactive than the central atom of the rod(111) facet.

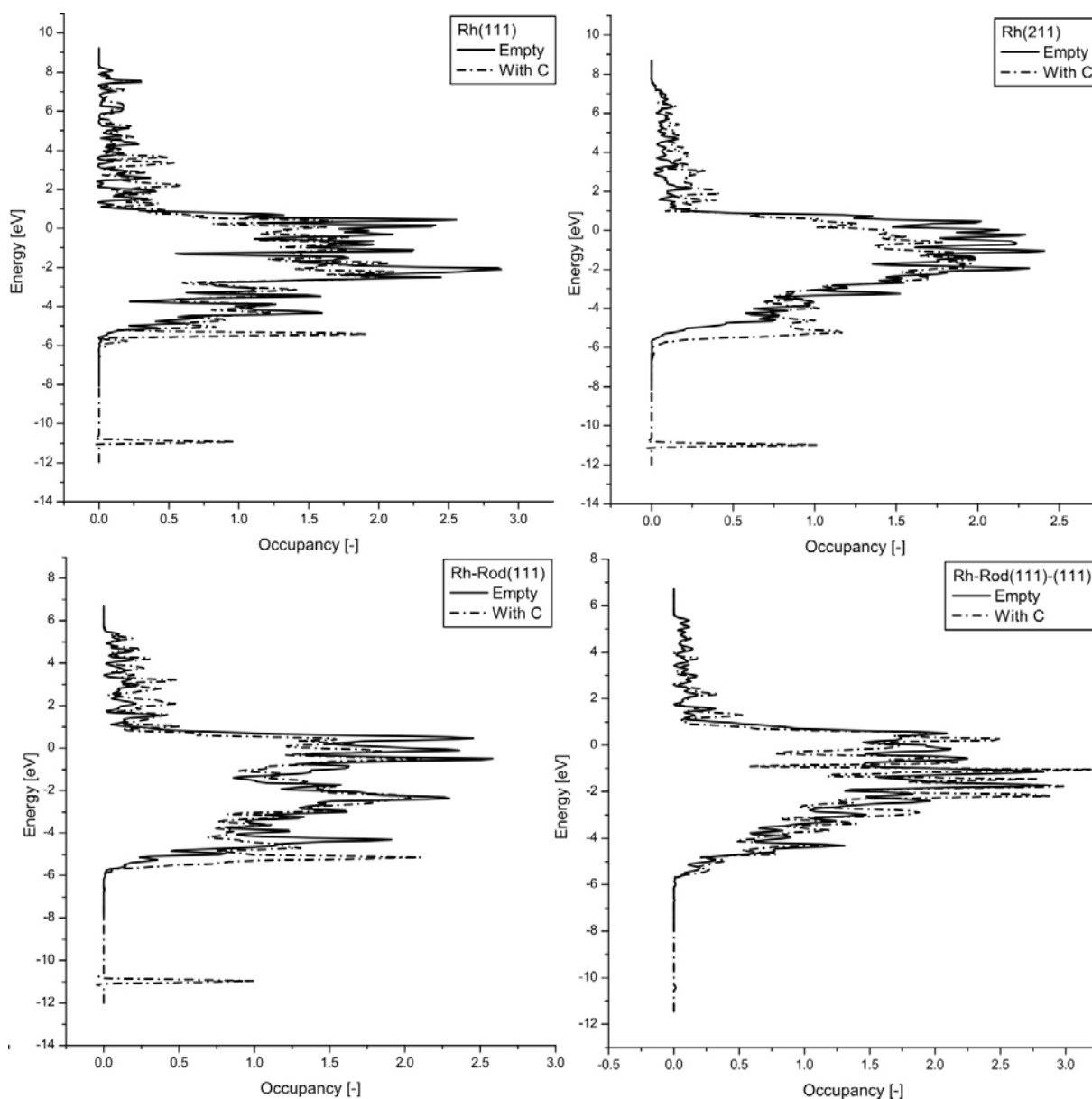


Figure 6. Local density of states (LDOS) plots of the d -orbitals of the surface Rh atom involved in C adsorption for the four respective surfaces, (a) Rh(111), (b) Rh(211), (c) Rh-rod(111) and (d) Rh-rod(111)-(111). The LDOS-plots are shown for the involved atom with (dashed line) and without (full line) carbon adsorbed.

Table 3. Average energy ($\bar{\epsilon}$) and width (σ) of the d -band of the surface Rh atoms.

	empty surface ¹		surface + C* ²	
	$\bar{\epsilon}$ (eV)	σ (eV)	$\bar{\epsilon}$ (eV)	σ (eV)
Rh(111)	-1.30	2.18	-1.54	2.78
Rh-rod(111) ¹	-1.59	2.01	-1.82	2.53
Rh(211)	-1.26	2.00	-1.55	2.67
Rh-rod(111)-(111) ¹	-1.40	1.80	-1.49	2.67

¹ involved in bonding of C before adsorption;

² involved in bonding after C adsorption;

³ Only the edge atoms are considered for Rh-rod(111) and Rh-rod(111)-(111).

5.5. Conclusions

In this study, we compare the energetics of the dehydrogenation of CH₄ to C on extended Rh(111) and Rh(211) surfaces and a planar (111) surface and the edge atoms that are shared between two (111) facets of a nanorod model. The adsorption energies between comparable surfaces of the extended and nanorod models are very similar. Only C adsorbs significantly stronger on the planar surface of the nanorod model than on the extended (111) surface due to the involvement of more reactive edge atoms. Also the reaction energies between the two types of surface models are very similar and small differences in reaction and activation energies are largely due to small geometrical differences. In all cases, CH dissociation has the highest activation barrier. However, dissociative CH₄ adsorption is rate controlling under typical steam reforming conditions because of the entropy loss associated with methane adsorption. The barrier for CH₄ dissociation significantly decreases with a decrease of the coordination number of the surface metal atoms. Accordingly, the corrugated surfaces are predicted to be more reactive for methane dissociation than the planar ones.

5.6. Acknowledgements

This project has been carried out in the framework of an EOS-LT program financed by SenterNovem. Supercomputing facilities were supported by the National Computational Facilities foundation of the Netherlands Organization for Scientific Research (NWO-NCF).

5.7. References

- [1] J.R. Rostrup-Nielsen, J. Sehested, J.K. Nørskov, Adv. Catal. 47 (2002) 65.
- [2] W.W. Irion, O.S. Neuwirth, Oil Refining; Wiley: Weinheim, Germany, 2005, 1-52.

- [3] H. Topsøe, B.S. Clausen, F.E. Massoth, *Hydrotreating Catalysis, Science and Technology*; Springer: Berlin, Germany, 1996.
- [4] J.R. Rostrup-Nielsen, *Steam Reforming Catalysts*; Danish Technical Press: Copenhagen, Denmark, 1975, 17-37.
- [5] J. Sehested, *Catal. Today* 111 (2006) 104.
- [6] J.R. Rostrup-Nielsen, J.H. Bak Hansen, *J. Catal.* 144 (1993) 40.
- [7] D. Qin, J. Lapszewicz, *Catal. Today* 21 (1994) 552.
- [8] G. Jones, J.G. Jakobsen, S.S. Shim, J. Kleis, M.P. Andersson, J. Rossmeisl, F. Abild-Pedersen, T. Bligaard, S. Helveg, B. Hinnemann, J.R. Rostrup-Nielsen, I. Chorkendorff, J. Sehested J.K. Nørskov, *J. Catal.* 259 (2008) 147.
- [9] S.-G. Wang, D.-B. Cao, Y.-W. Li, J. Wang, H. Jiao, *J. Phys. Chem. B* 110 (2006) 9976.
- [10] S.-G. Wang, D.-B. Cao, Y.-W. Li, J. Wang, H. Jiao, *Surf. Sci.* 600 (2006) 3226.
- [11] R.M. Watwe, H.S. Bengaard, J.R. Rostrup-Nielsen, J.A. Dumesic, J.K. Nørskov, *J. Catal.* 189 (2000) 16.
- [12] C.-T. Au, C.-F. Ng, M.-S. Liao, *J. Catal.* 185 (1999) 12.
- [13] I.M. Ciobica, R.A. van Santen, *J. Phys. Chem. B* 106 (2002) 6200.
- [14] I.M. Ciobica, F. Frechard, R.A. van Santen, A.W. Kleyn, J.P.J. Hafner, *J. Phys. Chem. B* 104 (2000) 3364.
- [15] A. Kokalj, N. Bonini, C. Sbraccia, S. de Gironcoli, S. Baroni, *J. Am. Chem. Soc.* 126 (2004) 16732. [16] B.S. Bunnik, G.J. Kramer, *J. Catal.* 242 (2006) 309.
- [17] F. Abild-Pedersen, O. Lytken, J. Engbæk, G. Nielsen, I. Chorkendorff, J.K. Nørskov, *Surf. Sci.* 590 (2005) 127.
- [18] K. Honkala, A. Hellman, I.N. Remediakis, A. Logadottir, A. Carlsson, S. Dahl, C.H. Christensen, J.K. Nørskov, *Science* 307 (2005) 555.
- [19] Z.-P. Liu, P. Hu, *J. Am. Chem. Soc.* 125 (2003) 1958.
- [20] R.A. van Santen, *Acc. Chem. Res.* 42 (2009) 57.
- [21] P.W. van Grootel, E.J.M. Hensen, R.A. van Santen, *Surf. Sci.* 603 (2009) 3275.
- [22] P.W. van Grootel, E.J.M. Hensen, R.A. van Santen, *Langmuir* 26 (2010) 16339.
- [23] C.H. Bartholomew, R.J. Farrauto, *Fundamentals of Industrial Catalytic Processes*, 2nd ed.; Wiley: USA, 2006.
- [24] J.M. Wei, E. Iglesia, *J. Phys. Chem. B* 108 (2004) 4094.
- [25] J.M. Wei, E. Iglesia, *Angew. Chem., Int. Ed.* 43 (2004) 3685.
- [26] J.M. Wei, E. Iglesia, *J. Phys. Chem. B* 108 (2004) 7253.
- [27] J.M. Wei, E. Iglesia, *J. Catal.* 225 (2004) 116
- [28] J.M. Wei, E. Iglesia, *Phys. Chem. Chem. Phys.* 6 (2004) 3754.
- [29] J.C.W. Swart, P. van Helden, E. van Steen, *J. Phys. Chem. C* 111 (2007) 4998.
- [30] G. Kresse, J. Furthmüller, *Comp. Mat. Sci.*, 6 (1996) 15.

- [31] G. Kresse, J. Furthmüller, *Phys. Rev. B* 54 (1996) 11169.
- [32] J.P. Perdew, J.A. Chevary, S.H. Vosko, K.A. Jackson, M.R. Pederson, D.J. Singh, C. Fiolhais, *Phys. Rev. B* 46 (1992) 6671.
- [33] P.E. Blöchl, *Phys. Rev. B* 50 (1994) 17953.
- [34] G. Kresse, J. Joubert, *Phys. Rev. B* 59 (1999) 1758.
- [35] H.J. Monkhorst, J.D. Pack, *Phys. Rev. B* 13 (1976) 5188.
- [36] G. Henkelman, B.P. Uberuaga, H. Jónsson, *J. Chem. Phys.* 113 (2000) 9901.
- [37] P. Atkins, J. De Paula, *Atkins' Physical Chemistry*, 8th ed.; Oxford University Press: Oxford, U.K., 2006.
- [38] O.R. Inderwildi, S.J. Jenkins, D.A. King, *J. Am. Chem. Soc.* 129 (2007) 1751.

Chapter 6:

Microkinetic model of steam methane reforming

A microkinetic model has been constructed to investigate the structure dependence of the steam methane reforming reaction for Rh. The model predicts a much higher reactivity for a stepped surface than for the close-packed planar surface. The composition of the adsorbed layer depends critically on the relative rates of methane and water activation and carbon monoxide recombination. On both surfaces, methane activation is the rate limiting step. A comparison of experimental and simulated kinetic parameters further underpins the importance of low coordinated surface atoms to catalyze methane activation with low barrier. This assignment is fully consistent with the experimentally observed structure dependence of the steam methane reforming reaction. A salient detail is the need for step-edge sites to maintain a high rate of CO recombination. Their density, however, is not critical as the activation free energy barrier for CO recombination on these sites is many times higher than the activation free energy barrier for dissociative CH_4 adsorption.

6.1. Introduction

One of the most intriguing and important questions in heterogeneous catalysis is the dependency of the activity and selectivity of catalytic reactions on the size of catalytic particles. It is by now well established that reactions involving cleavage of C-H bonds exhibit a rapid increase of the reaction rate with decreasing particle size, whereas when C-H bonds are formed in the course of the catalytic reaction, the overall rate does not depend on the

particle size. On the other hand, the rate of a reaction, in which a CO triple bond is broken, decreases along with the particle size. Quantum-chemical calculations have been performed relevant to the steam methane reforming (SMR) reaction, by which methane is converted to synthesis gas [1,2].

During the SMR process a range of surface-catalyzed processes take place in a consecutive as well as in a parallel manner. At the initial stage of the reaction, methane is activated on the surface resulting in the adsorbed CH_x fragments. Besides that, water also adsorbs and dissociates on the surface. To produce CO, the adsorbed CH_x fragments have to react with O adatoms resulting from dissociative water adsorption. DFT calculations evidence a pronounced surface structure dependency of the activation barriers for this recombination reaction [2-4]. The dependency on the type of metal is only weak though, which is in line with the Bronsted-Evans-Polanyi relationship for surface recombination reactions [5]. On dense surfaces the barriers for the CO recombination are higher than 160 kJ/mol for Rh [2]. On more open stepped surfaces this barrier decreases to values below 100 kJ/mol. H_2O dissociation proceeds with low barrier when preadsorbed oxygen atoms are present at the surface [6,7]. Such an O_{ads} -assisted water splitting yields adsorbed OH species. This reaction also shows only a weak dependence on the metal type, because it involves a simultaneous formation of a new metal oxygen bond and the weakening of another one. These two elementary processes effectively compensate each other. Oxygen adatoms are generated by further splitting of adsorbed OH species. The activation barriers for this reaction depend strongly on the strength of the metal-oxygen surface bond, in other words, on the affinity of a particular metal towards oxygen. The weaker this bond, the more difficult the OH bond cleavage [6].

Clearly the strong structure dependence of the $\text{CH}_{\text{ads}}\text{-O}_{\text{ads}}$ recombination implies that based on a comparison of the calculated activation energies, catalytic nanoparticles that expose more open (211) or (221) type surfaces will exhibit higher reactivity in this reaction. Because these surfaces are characterized by higher surface energies, they are expected to be present with a reasonable probability only for larger particles. When particle size decreases only the dense non-reactive surfaces will be exposed resulting in the increase of the activation energies for the recombination reaction. This expected particle size dependence is inconsistent with the observed increase of the overall rate of SMR with increasing dispersion of the transition metal particles [8,9]. This further supports the conclusion that the initial methane activation is the rate controlling step because of the high activation free energy of

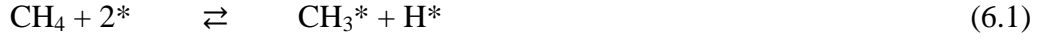
this reaction. Since the activation of methane is a reaction between a gas phase molecule with a surface there is a large entropy loss associated with the loss of translational and rotational degrees of freedom upon the surface reaction. The contribution of the activation free entropy change for dissociative methane adsorption is approximately 100 kJ/mol at a temperature of 773 K. This indeed increases dramatically the activation free energy as compared to the free activation enthalpies, which are generally in the order of 30-70 kJ/mol for Rh [1]. On the contrary, the values of activation enthalpies and activation free energies for elementary reaction steps on a catalyst surface are usually similar. Thus, it is of lesser importance to explicitly take into account the entropical contributions to reaction free energies for surface reactions as compared to adsorption or desorption reaction steps.

One can see that by using quantum chemical calculations one can unravel the detailed picture of the mechanism of surface-catalyzed reactions as well as compute individual energy parameters for elementary reaction steps. However, this information is not enough to directly compare the mechanistic details derived from quantum chemical modeling with the actual experimentally determined rates of catalytic reactions. Thus, we will here conclude our modeling work of the Rh-catalyzed SMR reaction by illustrating the consequences of differences in metal surface reactivity for the actual kinetics. In microkinetic modeling, as will be employed here, rate constants of elementary reaction steps are used in the mean field differential equations that describe the kinetics of the reaction. The output of such a simulation is reaction rate and surface coverage. Earlier, the groups of Vlachos [10] and Nørskov [8] have carried out microkinetic simulations of the SMR reaction for rhodium and other metals. The work of Vlachos is hampered by the quality of the input. Where in our study DFT calculations are used to determine activation energies and pre-exponential factors, they have used the less accurate UBI-QEP method to determine the activation energies, and have used the pre-exponential factors to fit their model to experimental results. The work of Nørskov is unclear how the reactions are calculated, but the activation energies are determined via a BEP-relation to results calculated on Ru. Also the H₂O and OH dissociation are neglected.

In the present work we base the reaction rate constants for all elementary reaction steps on activation energy barriers and entropy changes computed by quantum chemical modeling. Of particular interest is the structure dependence of the SMR reaction for Rh nanoparticles. To this end, the simulations are performed for planar and stepped Rh surface. In the discussion, particular attention will be paid to the influence of the step-edge site density on nanoparticles.

6.2. Computational details

The reaction mechanism for the SMR reaction includes thirteen elementary reaction steps. Besides the conventional reactions, we also consider here the formyl intermediate as well as oxygen-assisted water activation:



Corresponding to these are the rates of the elementary reaction steps, which for each step involve a forward and backward step. In the microkinetic model adsorption of the products CO and H₂ are not taken into account so that 24 reaction rates should be considered:

$$r_1 = Z_1 \cdot k_{\text{CH}_4,\text{ads}} \cdot \theta_* \cdot \theta_* \quad (6.14)$$

$$r_{-1} = Z_1 \cdot k_{\text{CH}_4,\text{des}} \cdot \theta_{\text{CH}_3} \cdot \theta_{\text{H}} \quad (6.15)$$

$$r_2 = Z_2 \cdot k_{\text{CH}_3,\text{dis}} \cdot \theta_{\text{CH}_3} \cdot \theta_* \quad (6.16)$$

$$r_{-2} = Z_2 \cdot k_{\text{CH}_3,\text{frm}} \cdot \theta_{\text{CH}_2} \cdot \theta_{\text{H}} \quad (6.17)$$

$$r_3 = Z_3 \cdot k_{\text{CH}_2,\text{dis}} \cdot \theta_{\text{CH}_2} \cdot \theta_* \quad (6.18)$$

$$r_{-3} = Z_3 \cdot k_{\text{CH}_2,\text{frm}} \cdot \theta_{\text{CH}} \cdot \theta_{\text{H}} \quad (6.19)$$

$$r_4 = Z_4 \cdot k_{\text{CH},\text{dis}} \cdot \theta_{\text{CH}} \cdot \theta_* \quad (6.20)$$

$$r_{-4} = Z_4 \cdot k_{\text{CH},\text{frm}} \cdot \theta_{\text{C}} \cdot \theta_{\text{H}} \quad (6.21)$$

$$r_5 = k_{\text{H}_2\text{O},\text{ads}} \cdot \theta_* \quad (6.22)$$

$$r_{-5} = k_{\text{H}_2\text{O},\text{des}} \cdot \theta_{\text{H}_2\text{O}} \quad (6.23)$$

$$r_6 = Z_6 \cdot k_{\text{H}_2\text{O},\text{dis}} \cdot \theta_{\text{H}_2\text{O}} \cdot \theta_* \quad (6.24)$$

$$r_{-6} = Z_6 \cdot k_{\text{H}_2\text{O,frm}} \cdot \theta_{\text{OH}} \cdot \theta_{\text{H}} \quad (6.25)$$

$$r_7 = Z_7 \cdot k_{\text{OH,dis}} \cdot \theta_{\text{OH}} \cdot \theta_*$$

$$r_{-7} = Z_7 \cdot k_{\text{OH,frm}} \cdot \theta_{\text{O}} \cdot \theta_{\text{H}} \quad (6.27)$$

$$r_8 = Z_8 \cdot k_{\text{H}_2\text{O,dis2}} \cdot \theta_{\text{H}_2\text{O}} \cdot \theta_{\text{O}} \quad (6.28)$$

$$r_{-8} = Z_8 \cdot k_{\text{H}_2\text{O,frm2}} \cdot \theta_{\text{OH}} \cdot \theta_{\text{OH}} \quad (6.29)$$

$$r_9 = Z_9 \cdot k_{\text{CO,frm}} \cdot \theta_{\text{C}} \cdot \theta_{\text{O}} \quad (6.30)$$

$$r_{-9} = Z_9 \cdot k_{\text{CO,dis}} \cdot \theta_{\text{CO}} \cdot \theta_*$$

$$r_{10} = Z_{10} \cdot k_{\text{CHO,frm}} \cdot \theta_{\text{CH}} \cdot \theta_{\text{O}} \quad (6.32)$$

$$r_{-10} = Z_{10} \cdot k_{\text{CHO,dis}} \cdot \theta_{\text{CHO}} \cdot \theta_*$$

$$r_{11} = Z_{11} \cdot k_{\text{CHO,frm2}} \cdot \theta_{\text{CO}} \cdot \theta_{\text{H}} \quad (6.34)$$

$$r_{-11} = Z_{11} \cdot k_{\text{CHO,dis2}} \cdot \theta_{\text{CHO}} \cdot \theta_*$$

$$r_{-12} = k_{\text{CO,des}} \cdot \theta_{\text{CO}} \quad (6.36)$$

$$r_{-13} = Z_{13} \cdot Z_{13} \cdot k_{\text{H}_2,\text{des}} \cdot \theta_{\text{H}} \cdot \theta_{\text{H}} \quad (6.37)$$

In these rate equations k_i are the reaction rate constants, θ_i the surface coverages and Z_i the coordination numbers. Z equals 6 for the closed-packed (111) surface. For the stepped surface, Z_i equals 1 for those elementary reaction steps taking place in the step edge and 2 for those occurring along the edge. In the present study all reactions occur in the step edge except steps 1-3.

For unimolecular adsorption the reaction rate constant is calculated from

$$k_{ads}^i = \frac{A_{site} P_i \sigma_i}{\sqrt{2\pi m_i k_B T}}$$

with A_{site} the area of the adsorption site, P_i the partial pressure of component i , σ_i the sticking coefficient of component i , m the mass of component i , k_B Boltzmann's constant and T the temperature. The sticking coefficients of H_2O , H_2 and CO are taken to be unity and that of CH_4 0.01.

The rate constants of the surface and desorption reaction are computed by use of the transition state theory:

$$k_{TST} = \frac{k_B T}{h} \frac{p f'_{TST}}{p f_0} \cdot e^{-\Delta E_{barrier}/k_B T}$$

with pf'_{TST} the partition function of the transition state complex excluding the contribution of the partition function of the reaction coordinate, pf_0 the partition function of the ground state and $\Delta E_{barrier}$ the activation energy barrier.

Finally, the mean field differential equations that describe the surface coverage change with time are then:

$$\begin{aligned}
 d\theta_{CH_3}/dt &= + r_1 - r_{-1} - r_2 + r_{-2} \\
 d\theta_{CH_2}/dt &= + r_2 - r_{-2} - r_3 + r_{-3} \\
 d\theta_{CH}/dt &= + r_{-4} - r_4 - r_5 + r_{-5} - r_{10} + r_{-10} \\
 d\theta_C/dt &= + r_4 - r_{-4} - r_9 + r_{-9} \\
 d\theta_{CO}/dt &= + r_9 - r_{-9} - r_{11} + r_{-11} - r_{-12} \\
 d\theta_{CHO}/dt &= + r_{10} - r_{-10} + r_{11} - r_{-11} \\
 d\theta_{H_2O}/dt &= + r_5 - r_{-5} - r_6 + r_{-6} - r_8 + r_{-8} \\
 d\theta_{OH}/dt &= + r_6 - r_{-6} - r_7 + r_{-7} + 2 \cdot r_8 - 2 \cdot r_{-8} \\
 d\theta_O/dt &= + r_7 - r_{-7} - r_8 + r_{-8} - r_9 + r_{-9} - r_{10} + r_{-10} \\
 d\theta_H/dt &= + r_1 - r_{-1} + r_2 - r_{-2} + r_3 - r_{-3} + r_4 - r_{-4} + r_6 - r_{-6} + r_7 - r_{-7} - r_{11} \\
 &\quad + r_{-11} - 2 \cdot r_{-13} \\
 d\theta^*/dt &= - 2 \cdot r_1 + 2 \cdot r_{-1} - r_2 + r_{-2} - r_3 + r_{-3} - r_4 + r_{-4} - r_5 + r_{-5} - r_6 + r_{-6} \\
 &\quad - r_7 + r_{-7} + r_9 - r_{-9} + r_{10} - r_{-10} + r_{11} - r_{-11} + r_{-12} + 2 \cdot r_{-13}
 \end{aligned}$$

Table 1 collects the pre-exponential factors and activation energy barriers as obtained from quantum-chemical modeling. Note that we have scaled all energies by a factor 0.9 as it is known that DFT overestimates the energies. The adsorption energies of all components except CO were taken independent of the surface coverage. For carbon monoxide, the surface coverage dependent adsorption energy was fitted by a polynomial from the scaled DFT-computed adsorption energies (216 kJ/mol for $\theta \rightarrow 0$, 203 kJ/mol for $\theta = 0.11$, 180 kJ/mol for $\theta = 0.25$ and 166 kJ/mol for $\theta > 0.5$).

The microkinetic simulations were then carried out as follows. First, the steady-state surface coverages were calculated by solving the differential equations describing the coverage of each of the surface intermediates. This is done by using the ordinary differential equation solver ODE15s as implemented in Matlab. These steady-state surface coverages are then used to compute the rates of the individual elementary reaction steps, including the rates of CH_4 and H_2O adsorption and CO and H_2 desorption. These rates are turnover frequencies.

Thus, the reaction rates and surface coverages were obtained in the temperature range 523-1073 K (steps of 50 K) at given partial pressures of CH₄ and H₂O of 0.25 and 0.75 bar, respectively. We also computed the rates in a small temperature interval around the set temperature to obtain the apparent activation energy and the rates in a small interval of partial pressures for methane and water to determine the reaction orders in these two reactants.

Table 1. Kinetic parameters used for the microkinetic model of SMR on the planar Rh(111) and stepped Rh(211) surfaces.

Elementary reaction step	Rh(111)		Rh(211)	
	v_{pre}	$E_{barrier}$ [kJ/mol]	v_{pre}	$E_{barrier}$ [kJ/mol]
CH ₄ + 2* → CH ₃ * + H*	$7.3 \times 10^{4a)}$	52	$4.4 \times 10^{5a)}$	35
CH ₃ * + H* → CH ₄ + 2*	$1.6 \times 10^{11a)}$	96	$1.6 \times 10^{11a)}$	101
CH ₃ * + * → CH ₂ * + H*	6.7×10^{12}	41	2.4×10^{12}	54
CH ₂ * + H* → CH ₃ * + *	2.5×10^{12}	104	3.2×10^{12}	104
CH ₂ * + * → CH* + H*	1.7×10^{12}	3	3.4×10^{12}	23
CH* + H* → CH ₂ * + *	1.4×10^{13}	88	4.1×10^{13}	123
CH* + * → C* + H*	1.9×10^{13}	94	1.4×10^{13}	68
C* + H* → CH* + *	1.6×10^{13}	94	1.7×10^{13}	83
H ₂ O + * → H ₂ O*	$1.3 \times 10^{8a)}$	0	$1.3 \times 10^{8a)}$	0
H ₂ O* → H ₂ O + *	$1.9 \times 10^{16a)}$	35	$1.9 \times 10^{16a)}$	62
H ₂ O* + * → OH* + H*	2.3×10^{12}	57	6.2×10^{11}	55
OH* + H* → H ₂ O* + *	5.3×10^{13}	123	2.9×10^{13}	148
OH* + * → O* + H*	1.1×10^{13}	85	1.6×10^{13}	65
O* + H* → OH* + *	2.7×10^{13}	110	1.6×10^{13}	81
H ₂ O* + O* → 2 OH*	3.8×10^{12}	77	6.2×10^{11}	53
2 OH* → H ₂ O* + O*	3.5×10^{13}	31	2.9×10^{13}	51
C* + O* → CO*	2.4×10^{12}	164	6.4×10^{12}	66
CO* → C* + O*	2.3×10^{12}	208	1.6×10^{12}	127
CH* + O* → CHO* + *	$1.0 \times 10^{13b)}$	166	$1.0 \times 10^{13b)}$	84
CHO* + * → CH* + O*	$1.0 \times 10^{13b)}$	113	$1.0 \times 10^{13b)}$	56
CO* + H* → CHO* + *	$1.0 \times 10^{13b)}$	123	$1.0 \times 10^{13b)}$	87
CHO* + * → CO* + H*	$1.0 \times 10^{13b)}$	26	$1.0 \times 10^{13b)}$	62
CO* → CO + *	$6.1 \times 10^{16a)}$	225	$6.1 \times 10^{16a)}$	225
2 H* → H ₂ + 2*	$6.7 \times 10^{13a)}$	92	$6.7 \times 10^{13a)}$	120

a) Pre-exponential factors of adsorption and desorption steps at 773 K. Partial pressure of CH₄ and H₂O are 0.25 and 0.75 bar.

b) Not calculated.

Finally, it was determined which step was rate controlling by procedures as proposed by Stegelmann *et al.* [11]. To this end, two parameters are employed, namely the degree of thermodynamic control (X_{TRC}):

$$X_{TRC} = \frac{k_i}{r} \left(\frac{\partial r}{\partial \left(\frac{-G_i^0}{RT} \right)} \right)_{G^0_{m \neq n}, G^0_{i,TS}} = \left(\frac{\partial \ln r}{\partial \ln \left(\frac{-G_i^0}{RT} \right)} \right)_{G^0_{m \neq n}, G^0_{i,TS}},$$

where the partial derivative is taken keeping the standard-state Gibbs free-energy constant of all other intermediates $m \neq n$ ($G_{m \neq n}^0$) and Gibbs free energy of all transition states i constant ($G_{i,TS}^0$), and the degree of rate control (X_{RC}):

$$X_{RC} = \frac{k_i}{r} \left(\frac{\partial r}{\partial k_i} \right)_{k_{j \neq i}, K_i} = \left(\frac{\partial \ln r}{\partial \ln k_i} \right)_{k_{j \neq i}, K_i}$$

where the partial derivative is taken holding constant the rate constants, k_j , for all other steps $j \neq i$, and the equilibrium constant K .

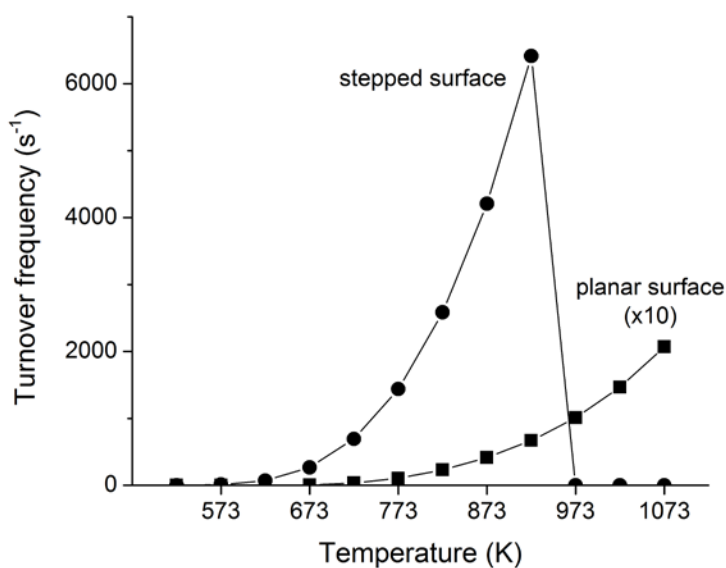


Figure 1. Turnover frequency (in s^{-1}) of steam methane reforming on the planar (squares) and stepped (circles) Rh surfaces as a function of temperature (in K).

6.3. Results

6.3.1. Reaction kinetics of SMR on planar and stepped surfaces

Figure 1 shows the reaction rates for the planar and stepped Rh surfaces as a function of temperature. It is immediately clear that the reaction rate per surface site (= turnover frequency, TOF) is much higher for the stepped surface. Whereas the activity of the planar surface shows a strong increase up to 1073 K, the rate for the stepped surface becomes very small for temperatures higher than 923 K. To explain this very different behavior, it is useful to compare the composition of the adsorbed layer as a function of temperature (Figure 2). Expectedly, the surface coverages tend to decrease with increasing temperature. For the planar surface (Figure 2a), at relatively low temperature, the surface is completely covered by C and O adatoms and CO. At 523 K, when the surface predominantly contains oxygen

adatoms, the rate is very low. With increasing temperature the surface becomes increasingly covered by C_{ads} at the expense of O_{ads} , which is due to the increased rate of CH_4 dissociation. The $C_{\text{ads}}+O_{\text{ads}}$ coverage is high because of the high barrier for CO recombination. Above 773 K, when the rate increases strongly, the C surface coverage decreases because C_{ads} is removed via CO recombination. Under these conditions, the rate of dissociative CH_4 adsorption is seven orders of magnitude lower than the rate of H_2O adsorption. In the considered temperature range, the rate controlling step is dissociative CH_4 adsorption ($X_{\text{RC}} = 1$). By inspection of the rates of the individual elementary reaction steps, it is also found that all CO_{ads} is formed by direct recombination of C_{ads} and O_{ads} and not via CHO_{ads} .

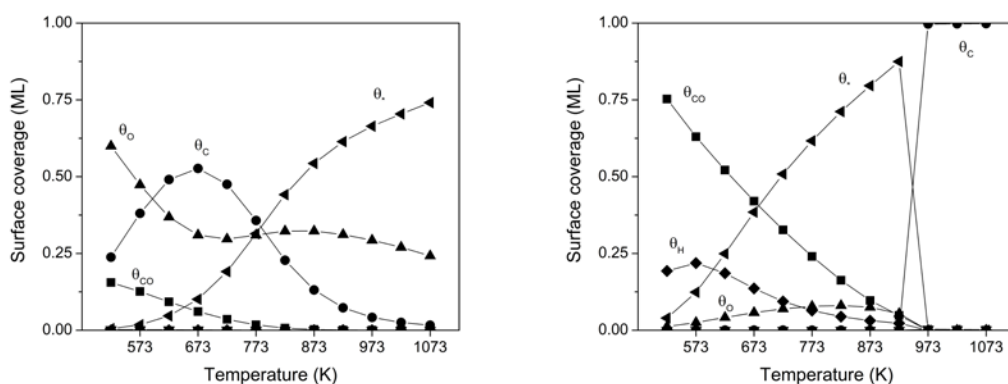


Figure 2: The steady-state surface coverage (in ML) as a function of temperature (in K) for (a) planar and (b) stepped Rh surfaces. The surface coverage for the species not indicated in the graph are smaller than 0.01 ML.

The composition of the adsorbed layer for the stepped Rh surface is very different (Figure 2b). The total surface coverage is lower than on the planar surface due to the higher reactivity of the step-edge sites. At low temperature the dominant surface intermediate is CO_{ads} . The much lower C surface coverage for the stepped surface is explained by the much lower barrier for CO recombination. This also leads to a lower steady-state coverage with O. As a result, the rate for the stepped surface is substantially higher than for the planar one. Comparison of the rates of the elementary surface reaction steps shows that the rate of CO surface recombination is higher than the rate of CO desorption. The reason is that a considerable part of CO reacts with H atoms via the formyl surface intermediate to adsorbed CH and O. This is a consequence of (i) the higher stability of adsorbed $\text{CH}_{\text{ads}} + \text{O}_{\text{ads}}$ vs. $\text{CO}_{\text{ads}} + \text{H}_{\text{ads}}$ and (ii) the relatively low barrier for the reverse reaction. With increasing temperature, the surface coverage with CO decreases substantially. This leads to a small increase of the O surface coverage. It is seen that above 823 K the oxygen surface coverage begins to decrease.

When the oxygen surface coverage becomes too low, *i.e.* at temperatures above 923 K, the rate of removal of C_{ads} by $C_{ads} + O_{ads}$ recombination becomes so low that the surface becomes poisoned by C_{ads} . Under these circumstances it is found that the rate controlling steps are molecular H_2O adsorption ($X_{RC} = 1$), H_2O dissociation to OH and H ($X_{RC} = 1$) and CO desorption ($X_{RC} = 2$). From Table 1, we can then infer that the reason for poisoning by C_{ads} of the Rh(211) surface is the higher ratio of the rates of dissociative CH_4 adsorption and H_2O adsorption as compared to Rh(111).

Table 2. Rates (in s^{-1}), MARI (in ML) and rate controlling reactions for changing activation energies (in kJ/mol), starting at those for the planar surface and ending with those for the stepped surface (*italic*). The reaction temperature is 773 K.

Eact (CH_4 diss)	Eads (H_2O)	Eact (CO rec)	Eact (OH diss)	TOF (s^{-1})	Coverage (ML)	X_{RC}	Model
52	35	164	85	4.4	<i>O (0.31)</i> C (0.36) * (0.74)	CH_4 diss. = 1	<i>Rh(111)</i>
52	35	66	85	10.6	<i>O (0.47)</i> * (0.48)	CH_4 diss. = 1	
35	35	164	85	10^{-14}	C (0.99)	CH_4 diss. = 0.53 H_2O ads. = 0.84 H_2O des. = -0.86 H_2O diss. = 0.83 OH diss. = 0.18 CO des. = 1.89	
35	35	66	85	10^{-14}	C (0.99)	CH_4 diss. = -0.08 H_2O ads. = 0.89 H_2O des. = -0.94 H_2O diss. = 0.92 OH diss. = 0.19 CO des. = 1.99	
35	62	66	85	1096	CO (0.22) O (0.18) * (0.54)	CH_4 diss. = 1	
35	62	66	65	1560	CO (0.24) O (0.10) * (0.64)	CH_4 diss. = 1	
35	62	164	65	0.1	C (0.99)	CH_4 diss. = 1	
32	62	66	65	1438	CO (0.24) <i>O (0.08)</i> * (0.61)	CH_4 diss. = 1	<i>Rh(211)</i>

To understand in more detail how the substantial activity differences between the planar and stepped Rh surfaces relates to the composition of the surface adlayer we investigate how the rate, the most abundant reaction intermediate (MARI) and the degree of rate control of the various steps (X_{RC}) are influenced by changes in the kinetic parameters. Table 2 contains data

for the planar (first entry) and stepped (last entry) surfaces as well as intermediate cases in which several parameters were varied.

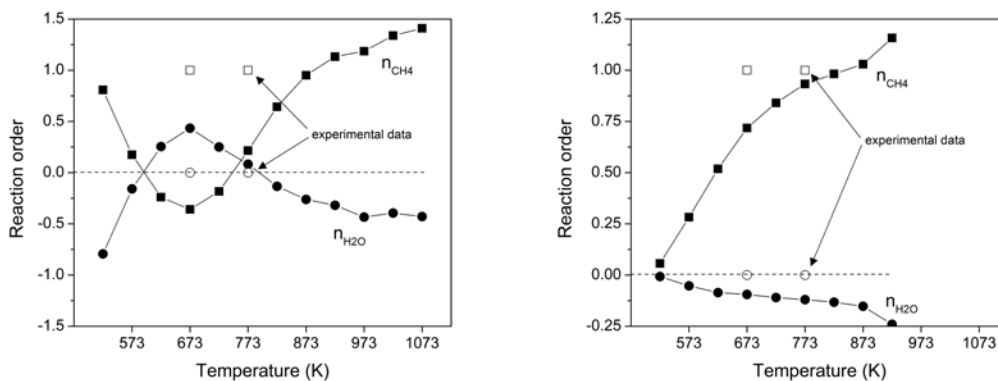


Figure 3. Reaction order of methane (full squares) and water (full circles) on the (a) planar and (b) stepped Rh surfaces. The experimentally determined reaction orders [9] for methane (open square) and water (open circles) are shown for comparison.

The TOF for the planar and stepped surfaces at 773 K are 4.4 and 1438 s^{-1} , respectively. For the planar surface, dissociative CH_4 adsorption is rate limiting ($X_{\text{RC}} = 1$). It can be seen that a decrease of the activation energy for CO recombination from 164 kJ/mol to 66 kJ/mol, *i.e.* the value for Rh(211), only results in a very small increase of the TOF to 10.6 s^{-1} for the planar surface. This is consistent with this step not being rate controlling. Alternatively, when alternatively the barrier for dissociative CH_4 adsorption is lowered from 52 kJ/mol to 35 kJ/mol, the activity becomes negligible because of poisoning by C_{ads} . From the rate control parameters, it becomes immediately clear then that O_{ads} is the limiting intermediate. This situation of a high rate of CH_4 activation relative to that of H_2O activation is similar to the case for the stepped surface at high temperature (*vide supra*). The next entry contains the same parameters for CH_4 activation but with the higher water adsorption energy of the stepped surface. In this case, C_{ads} poisoning does not occur because of the higher coverage with O. The rate is now 1096 s^{-1} , which is still somewhat lower than the value for the stepped surface. The rate limiting step has expectedly changed to dissociative CH_4 adsorption. To have nearly same rate as for the stepped surface, it is only required to decrease the barrier for OH dissociation from 85 to 65 kJ/mol, leading to a final rate of 1560 s^{-1} . In the latter two cases, the MARI is CO in line with the results for the stepped surface. When, in the latter case, the barrier for CO recombination is increased to the value for the planar surface (164 kJ/mol), the TOF decreases sharply to 0.1 s^{-1} , but again with dissociative CH_4 adsorption remaining rate limiting.

Expectedly, the rate of the SMR reaction is controlled by the surface coverage of atomic C and O adatoms, but a facile pathway to CO recombination is also required. The above discussion shows that a subtle balance between CH₄ and H₂O activation and CO recombination is required to avoid C_{ads} poisoning and maintain high activity.

It is not straightforward to directly compare these data to experimental results, because (i) the exact surface topology of Rh nanoparticles in technical catalysts is not known so that we do not know the exact turnover frequency and (ii) surface coverages cannot be directly measured. Therefore, we also computed the reaction orders in CH₄ and H₂O as well as the apparent activation energies as a function of temperature for comparison with experimental data. The reaction orders for the planar surface (Figure 3a) show the following trends. At low temperature, with O_{ads} being the MARI, the reaction order in water is negative, whereas that in methane is positive. Obviously, an increase in the water partial pressure will increase the O surface coverage and decrease the C surface coverage. The overall effect on the reaction rate is negative. The situation reverses for intermediate temperatures (600 K < T < 773 K), when the surface contains more C than O. With increasing temperatures then the order in H₂O is negative, because of the reasonable oxygen surface coverage, and that in CH₄ increases. At high temperature, the reaction order in CH₄ is slightly above unity. This is because an increase of the CH₄ partial pressure will lead to a more than proportional increase of the C surface coverage as the increasing C surface coverage will also lead to a lower O surface coverage (higher rate of CO recombination reactions). On the stepped surface (Figure 3b) the order in CH₄ is always positive, which agrees with the very low steady-state C surface coverage. The order is close to zero for low temperature, because the surface is nearly completely covered by CO. Similarly, the reaction order in H₂O is also close to zero. With increasing temperature and decreasing CO coverage, the reaction order in CH₄ increases to unity and that in H₂O becomes slightly negative. Again, as discussed above, the reaction order in CH₄ is slightly higher than unity because the reaction does not proceed over an empty surface. From the comparison of the simulated reaction orders in Figure 3 with experimental data [9], it can be concluded that the stepped surface is a more likely candidate to represent the surface sites active in actual nanoparticle catalysts. This is further underpinned by comparing the experimentally determined apparent activity energies with the simulated values in Figure 4. In all cases, the apparent activation energy is substantially higher than the activation energy of the rate limiting methane dissociation step. The reason is the high surface coverage with the products of dissociative methane adsorption, namely C_{ads},

O_{ads} and CO_{ads} , whose removal facilitates the reaction. Consequently, the lower coverages at higher temperatures due to CO recombination and desorption result in lower apparent activity energies.

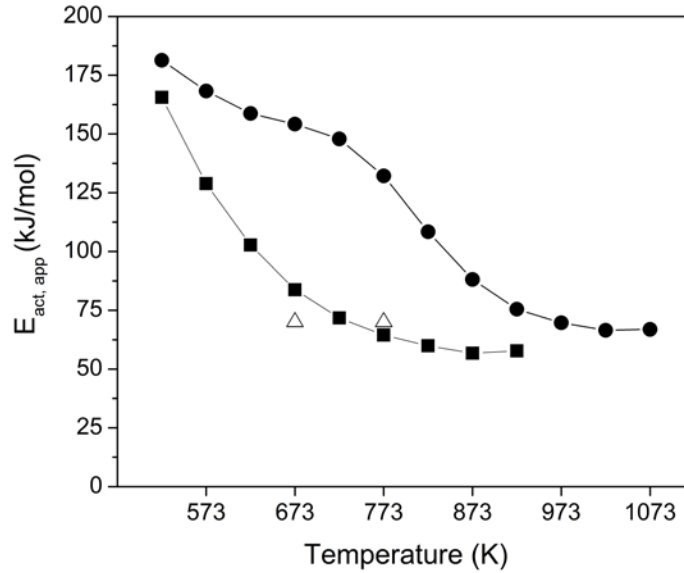


Figure 4. The calculated apparent activation energy of steam methane reforming on the planar (circles) and stepped (squares) Rh surfaces. The experimental data [9] (open triangles) is also depicted.

Table 3. Simulating a nano particle with decreasing size by changing the ratio of available sites for methane dissociation and carbon monoxide formation.

$E_{act,COfrm}$ [kJ/mol]	N_{CH4}	N_{CO}	rate [s ⁻¹]	MARI	$X(rc)$
66	1	1	1439	CO (0.24) O (0.08) * (0.61)	CH ₄ diss = 1
164	1	1	0.03	CO (0.00) C (0.98) O (0.00) * (0.00)	CH ₄ diss = 1
66	1	0.1	1438	CO (0.24) O (0.08) * (0.61)	CH ₄ diss = 1
66	1	0.01	1426	CO (0.24) O (0.08) * (0.61)	CH ₄ diss = 1
66	1	0.001	1310	CO (0.23) O (0.07) * (0.61)	CH ₄ diss = 1
66	2	1	2643	CO (0.27) O (0.05) * (0.59)	CH ₄ diss = 1

N.B.: CHO path disabled by increasing $E_{act,CHOfrm}$ and $E_{act,CHOfrm2}$ to 300 kJ/mol

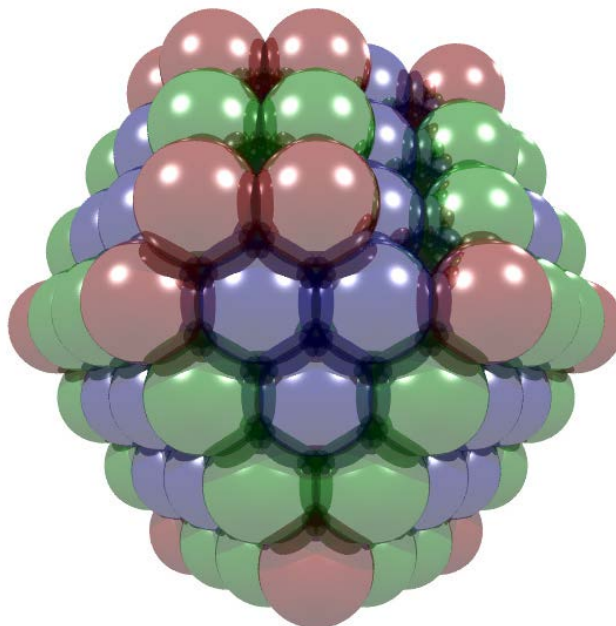


Figure 5. Rh_{153} nanoparticle with an added layer of 6 atoms on one of the faces to form a step-site. This particle consists of 57 bulk, 38 terrace (blue), 44 edge (green) and 16 corner (red) atoms.

Hence, the present microkinetic analysis shows that (i) dissociative CH_4 adsorption is the rate determining step, (ii) low-coordinated Rh surface atoms are the active sites for dissociative CH_4 adsorption and (iii) step-edge sites are required for facile $\text{C}_{\text{ads}}+\text{O}_{\text{ads}}$ recombination. Conclusions (i) and (ii) are fully consistent with the experimentally determined particle size dependence for the SMR reaction by Rh. However, our simulations indicate that the surface of these nanoparticles should contain step-edge sites because these sites allow fast CO recombination. It is commonly believed that, when the nanoparticles become very small, the surface is dominated by edge and corner sites with a very low density of step-edge sites. If this were true, one would expect to find a maximum in the rate as a function of particle size. The absence of step-edge sites on small nanoparticles will lead to a high barrier for CO recombination and a low reaction rate (Table 2). However, under these circumstances of low reaction rate dissociative CH_4 adsorption remains rate controlling. Thus, we may expect that a lower density of step-edge sites will not substantially affect the overall rate as long as they are present. To simulate the strong decrease of the ratio of step-edge sites and corner/edge sites with decreasing particle size, we independently varied the densities of both these types of sites. The results of such simulations, presented in Table 3, immediately show that the rate does not substantially depend on the step-edge site density. Even when the number of step-edge is lower by three orders of magnitude than the number of edges, the rate only decreases by less than 10%. Thus, it can be inferred that a very low density of step-edges is sufficient to

maintain a high rate of CO recombination, which remove the C and O adatoms. In the absence of step-edge sites, the barrier for CO recombination will be that for the terrace surface, resulting in a too low rate of CO recombination and, consequently, C poisoning of the surface. Although it has not yet been possible to accurately determine the step-edge density on nanoparticles, it is useful to consider a Rh₁₅₃ nanoparticle (Figure 5) built from an ideal Rh₁₄₇ cubooctahedron to which 6 atoms have been added to create two step-edge sites. For this case, the ratio of edge-over-step-edge sites is ca. 30, which would be sufficient to maintain a high rate of steam methane reforming.

6.4. Conclusions

A microkinetic model has been constructed to investigate the structure dependence of the steam methane reforming reaction for Rh. The rate constants of all elementary reaction steps were calculated on the basis of reaction energy parameters computed by DFT calculations for the close-packed planar and a stepped surface. The microkinetic model predicts overall reaction rate, the rates of the individual reaction steps, surface coverages and rate control parameters as a function of partial pressures and temperature.

The reaction rate of the stepped surface is much higher than of the planar surface. For both surfaces, dissociative methane adsorption is rate limiting. The composition of the adsorbed layer depends critically on the relative rates of methane and water activation and carbon monoxide recombination. The higher rate of the stepped surface is due to the low barrier for CH₄ activation combined with easy removal of C_{ads} on step-edge sites. The high adsorption energy of H₂O is also critical to maintain a sufficiently high O surface coverage. Consequently, the surface contains strongly bound CO and also O_{ads}, while the C coverage is low. At high temperatures, however, the reaction rate becomes very low because of poisoning by C_{ads} due to depletion of O_{ads}. The adsorbed layer of the terrace surface contains C_{ads} and O_{ads} in more equal proportions. The rate, however, is very low because of the much lower rate of CH₄ activation. In this case C poisoning is avoided, because the surface always contains enough O_{ads}, despite the lower adsorption energy of H₂O.

The proposition of the low coordinated surface atoms of the stepped surface as the active sites for the SMR reaction is confirmed by the close similarity of experimental and simulated kinetic parameters. This conclusion is fully consistent with the experimentally reported structure dependence. Thus, the rate limiting step is methane activation on edges and corners of Rh nanoparticles. Importantly, the present work also shows that step-edge sites are

required to maintain a high rate of CO recombination. Their density, however, is not critical as the activation free energy barrier for CO recombination on these sites is many times higher than the activation free energy barrier for dissociative CH₄ adsorption.

6.5. References

- [1] P.W. van Grootel, R.A. van Santen, E.J.M. Hensen, *J. Phys. Chem. C*, 115 (2011) 13027.
- [2] P.W. van Grootel, E.J.M. Hensen, R.A. van Santen, *Langmuir*, 26 (2010) 16339.
- [3] O.R. Inderwildi, S.J. Jenkins, D.A. King, *J. Am. Chem. Soc.*, 129 (2007) 1751.
- [4] Z.-P. Liu, P. Hu, *J. Am. Chem. Soc.*, 125 (2003) 1958.
- [5] R.A. van Santen, *Acc. Chem. Res.*, 42 (2009) 57.
- [6] P.W. van Grootel, E.J.M. Hensen, R.A. van Santen, *Surf. Sci.*, 603 (2009) 3275.
- [7] G.-C. Wang, S.-X. Tao, X.-H. Bu, *J. Catal.*, 244 (2006) 10.
- [8] G. Jones, J.G. Jakobsen, S.S. Shim, J. Kleis, M.P. Andersson, J. Rossmeisl, F. Abild-Pedersen, T. Bligaard, S. Helveg, B. Hinnemann, J.R. Rostrup-Nielsen, I. Chorkendorff, J. Sehested, J.K. Nørskov, *J. Catal.*, 259 (2008) 147.
- [9] D.A.J.M. Ligthart, R.A. van Santen, E.J.M. Hensen, *Journal of Catalysis* 280 (2011) 206
- [10] M. Maestri, D.G. Vlachos, A. Beretta, G. Groppi, E. Tronconi, *Journal of Catalysis* 259 (2008) 211.
- [11] C. Stegelmann, A. Andreasen, C.T. Campbell, *J. Am. Chem. Soc.* 131 (2009) 9.

Summary:

A Theoretical Study on the Structure Dependence of the Steam Methane Reforming Reaction by Rhodium

Steam methane reforming is an important industrial reaction for the conversion of methane with steam to synthesis gas, a mixture of carbon monoxide and hydrogen. Hydrogen is used in many applications, e.g. for hydrogenation purposes. It is also used for the production of bulk chemicals such as ammonia and in combination with carbon monoxide for the manufacture of methanol and other oxygenates. Fischer-Tropsch synthesis is rapidly becoming a more important source of clean transportation fuels and potentially of chemicals and is also based on the use of synthesis gas. The most frequently used metal for steam methane reforming (SMR) catalysts is nickel. Typical reaction conditions for SMR are 800-900 °C to obtain high conversion of this endothermic reaction. However, in a number of applications, e.g. in pre-reforming and especially in future membrane steam reformers, the use of noble metals with a higher catalytic activity may be interesting. Especially in separation-enhanced reformers, which are typically run at lower temperatures, it is important to maintain high catalytic activity by shifting to noble metals such as Ru or Rh. Noble metals also show a higher resistance against carbon formation, which is one of the primary causes of deactivation, especially under carbon-rich conditions as can occur in a separation-enhanced reformer. The main goal of separation-enhanced steam reformers is to obtain pure streams of H₂ and CO₂ (CO is converted by the water-gas shift reaction to CO₂), the former to be used for electricity generation, the latter for storage. As such, this concept is a potential technology

for carbon capture and sequestration. As cost is a crucial factor for electricity generation, it is important to decrease the catalyst cost as much as possible, especially when the use of noble metals is required. Thus, we explore here in detail the structure dependence of the SMR reaction for Rh nanoparticles with the aim to guide the design and synthesis of optimal steam reforming catalysts.

To investigate structure sensitivity, we study the three candidate rate controlling elementary reaction steps in steam methane reforming, i.e. water dissociation (Chapter 3), CO formation (Chapter 4) and CH₄ dissociation (Chapter 5). This is done by density functional theory (DFT), which is a state-of-the-art technique to compute activation barriers of periodic models of transition metal surfaces. The results of these three studies are used as input for a microkinetic simulation model, which aims to understand the importance of the various reaction mechanisms as well as to explain experimentally observed structure dependence (Chapter 6).

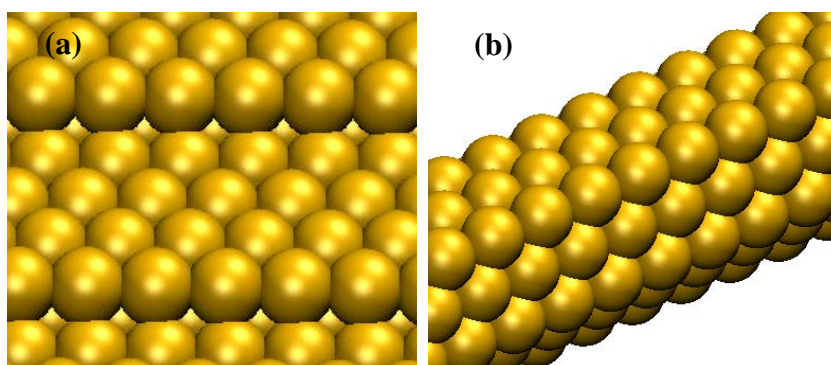


Figure 1. Representation of two Rh surfaces models employed in the present work. A stepped surface (a) with (211) steps and (111) terraces. The reactivity of the edge atoms as occurring on nanoparticles is simulated using a nanorod model (b).

In Chapter 3, the dissociation of water on planar and stepped surfaces (Figure 1a) and the role of oxygen adatoms herein were investigated. It is concluded that the activation of water is not influenced by the coordination number of the surface atoms involved. The activation energies are very close with a value of 63 kJ/mol for the planar Rh(111) and of 61 kJ/mol for the stepped Rh(221) surface. However, in the presence of a surface oxygen atom, which can act as a hydrogen acceptor, the barrier for the stepped surface (28 kJ/mol) is significantly lower than on the planar surface (53 kJ/mol). Despite this difference, a close inspection of the potential energy diagram indicates that the overall barrier in the latter cases is also around 60 kJ/mol, because one needs to account for the energy cost to bring the oxygen adatom in a favorable position. This process is endothermic because of the lateral interactions. A

Brønsted-Evans-Polanyi type correlation of the activation barriers with the metal-hydroxyl bond shows that the transition state of water dissociation has a slightly late character. Another finding is that there are large compensation effect for the oxygen-assisted water dissociation mechanism.

Chapter 4 compares three different reaction mechanisms for CO formation on planar Rh(111) and stepped Rh(211) surfaces (Figure 1a) starting from adsorbed CH and O. A general conclusion is that the direct mechanism via C+O recombination competes with the one going through a formyl intermediate (HCO), whereas the pathway via an alcoholate intermediate (COH) is unfavorable. On the planar surface the barrier for CH dissociation is ~100 kJ/mol, but the overall barrier for CO formation is 180 kJ/mol. The formation of the formyl intermediate on the planar surface has an activation barrier of 180 kJ/mol and its subsequent decomposition towards CO and H is easy. Overall barriers for these two processes are very similar. The presence of a step-edge site is favorable for formyl formation and decreases the barrier to 93 kJ/mol. Its influence of CH dissociation is minor and as a result the overall barrier for the formyl pathway is slightly preferred on the stepped surface. The consequences of these differences in reactivity are discussed for particle size dependence of the steam methane reforming reaction. Because this reaction is typically applied at relatively high temperature, the activation free energy of dissociative methane adsorption will be significantly higher than that of the surface recombination reactions that lead to CO formation. The particle size dependence observed experimentally, therefore, follows the changes in the activation of methane and this should be due to the increase of edge and corner sites with decreasing particle size. When C-O bond formation would have been rate controlling, a maximum in the rate of the methane steam reforming reaction as a function of decreasing particle size would have been predicted, because smaller particles will have fewer step-edge sites for CO recombination. Based on the metal-carbon and metal-oxygen binding energies the periodic trends of transition metals for the elementary reaction steps of the steam methane reforming reaction are compared. For highest catalytic performance both carbon and oxygen intermediates are required. The activation of methane and water can be related to the metal-carbon and metal-oxygen binding energies. Because of the requirement of optimal O coverage, the metal with the lowest barrier for methane activation (Ir) is not the metal with the highest reactivity in the methane steam reforming reaction (Ru).

In Chapter 5, we compare the energetics of the dehydrogenation of CH₄ to C on extended Rh(111) and Rh(211) surfaces and a planar (111) surface and the edge atoms that are shared

between two (111) facets of a nanorod model (Figure 1b). We found that similar surfaces on the periodic and nanorod model have almost comparable adsorption and reaction energies. This is not the case for the adsorption of the carbon adatom, which adsorbs stronger on the (111) surface of the nanorod than on the periodic planar surface. This is attributed to the binding of the adsorbate to the more reactive edge atoms in the nanorod model. The reaction energies only differ slightly due to small geometrical differences. The dissociation of CH was on all surfaces the reaction with the highest barrier. However, due to the contribution of the entropic loss during dissociative methane adsorption, this step is the most likely rate controlling step. In accordance with the earlier comparison of CO recombination on different surfaces, the barrier for CH₄ dissociation is strongly structure sensitive. The rate is much higher for surfaces that contain low-coordinated surface atoms.

A microkinetic model of SMR has been constructed and is described Chapter 6. This model is based on the elementary reaction steps and allows us to determine macroscopic properties such as the overall reaction rate, the rates of the individual elementary reaction steps, surface coverages and rate control parameters. The reaction rate constants are computed from the DFT computed barriers and entropic contributions. Based on this model, we conclude that for both planar and stepped surfaces, the rate of dissociative methane adsorption is rate limiting. The rate on the stepped surface is higher than on the planar. It becomes obvious that to maintain high activity a balance in the rates of dissociative adsorption of CH₄ adsorption, dissociation of H₂O and formation of CO is required. Although methane dissociation is rate limiting, it is necessary to also generate sufficient O adatoms to remove the carbon-containing surface intermediates. For the planar surface, the surface contains sufficient O_{ads} to remove C_{ads} under typical reaction conditions. However, because the structure dependence of water adsorption is less strong than for methane dissociation, it is found that at high temperature on the stepped surface the reaction rate becomes very low due to O_{ads} depletion leading to C_{ads} poisoning. The most important finding is that the experimentally observed structure dependence is consistent with the proposal of the dissociative methane adsorption on low coordinated surface atoms as the rate limiting step. However that may be, to maintain high activity one needs step-edge sites to remove C_{ads} and O_{ads} with low barrier. The step-edge density, however, is not critical as the activation free energy barrier for CO recombination on these sites is many times higher than the activation free energy barrier for dissociative CH₄ adsorption.

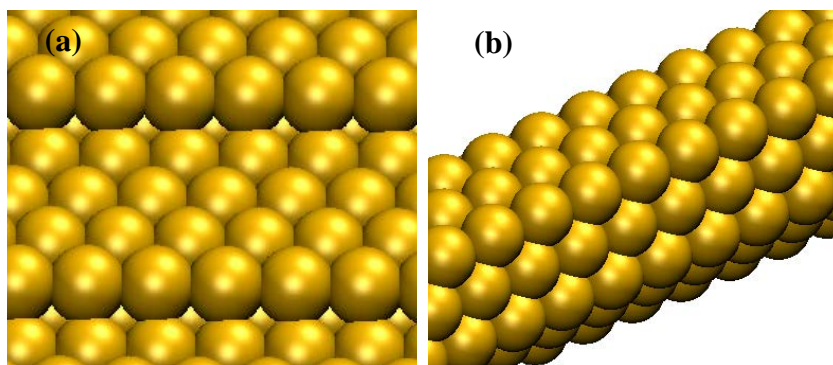
This work provides a complete picture on Rh-catalyzed steam methane reforming in which all potential rate controlling steps, namely CH₄ and H₂O dissociation and CO formation, have been studied with the same accuracy and methods. It is also clear that a microkinetic model is required to understand the exact implications of these reaction energy parameters. The present data only take into account lateral interactions between adsorbed CO. Moreover, the model has only assumed the presence of one type of sites. In this respect, it would be important to carry out similar simulations by kinetic Monte Carlo modeling with the advantage of (i) easily incorporating lateral interactions, (ii) diffusion, which may be important since the site for C_{ads} generation is different from C_{ads} removal and, related, (iii) the presence of different sites in one particle, their proportion depending on the particle size. Another research direction could be to use Brønsted-Evans-Polanyi relations to predict periodic trends as well as the behaviour of alloys. Coking due to carbon-carbon coupling reactions, likely occurring on terrace facets, is another topic of future interest.

Samenvatting: A Theoretical Study on the Structure Dependence of the Steam Methane Reforming Reaction by Rhodium

De reformering van methaan door stoom is een belangrijke industriële reactie voor de conversie van methaan naar synthese gas, een mengsel van kooldioxide en waterstof. Waterstof heeft vele toepassingen, bijvoorbeeld hydrogenering. Het wordt ook gebruikt voor de productie van bulk chemicaliën, zoals ammonia en in combinatie met koolmonoxide voor de productie van methanol en andere oxygenaten. Fischer-Tropsch synthese is hard op weg om een belangrijke bron van schone brandstof en mogelijk voor de productie van chemicaliën te worden. Deze synthese is ook gebaseerd op het gebruik van synthese gas. Het meest gebruikte metaal als katalysator voor de reformering van methaan door stoom (SMR) is nikkel. Gebruikelijke reactiecondities voor SMR is 800-900 °C om een hoge conversie te bereiken voor deze endotherme reactie. Echter bij een aantal toepassingen, zoals pre-reformering en op de lange termijn membraan stoom reformers, kan het gebruik van edelmetalen, in plaats van nikkel, met hogere activiteit interessant zijn. Dit is vooral nodig in de scheidingsversterkte reformers, die vooral op lagere temperaturen werken, waar de hoge katalytische activiteit behouden kan worden door over te stappen naar edelmetalen, bijvoorbeeld Ru of Rh. Edelmetalen zijn ook beter bestand tegen koolvorming, wat een van de grootste oorzaken is van deactivering van de katalysator, vooral onder de koolstofrijke condities zoals die bestaan in de scheidingsversterkte reformer. Het hoofddoel van de scheidingsversterkte reformer is het verkrijgen van pure stromen van H₂ en CO₂ (CO wordt

omgezet door de water-gas shift reactie naar CO_2). De reformer wordt gebruikt voor elektriciteitsproductie, waarbij de elektriciteit opgeslagen kan worden. Op deze manier kan de reformer als mogelijke techniek gebruikt worden voor CO_2 -scheiding en -afvang. Omdat bij elektriciteitsproductie de kosten zeer belangrijk zijn, is het belangrijk de kosten voor de katalysator zoveel mogelijk te drukken, vooral als er een edelmetaal bij gebruikt wordt. Daarom onderzoeken we hier in detail de structuurafhankelijkheid van de SMR-reactie voor Rh-nanodeeltjes, met als doel het sturen van het ontwerp en synthese van mogelijke SMR-katalysatoren.

Om de structuurafhankelijkheid te onderzoeken, bestuderen we drie mogelijke snelheidsbepalende elementaire reactiestappen in SMR, zijnde waterdissociatie (Hoofdstuk 3), CO -vorming (Hoofdstuk 4) en CH_4 -dissociatie (Hoofdstuk 5). Dit wordt gedaan met behulp van dichtheidspotentialtheorie (DFT), een state-of-the-art rekentechniek om o.a. activeringsbarrières in periodieke modellen van overgangsmetalen te bepalen. De resultaten van deze drie onderzoeken worden gebruikt als input voor een microkinetisch simulatiemodel. Dit model wordt gebruikt om de belangrijkste reactiemechanismen te onderscheiden en om de structuurafhankelijkheid die gezien wordt in experimenten te verklaren.



Figuur 1. Voorbeeld van de twee Rh oppervlakmodellen die in dit onderzoek gebruikt worden. Een gestapt oppervlak (a) met (211) stappen en (111) terrassen. De reactiviteit van de randatomen zoals die zich op nanodeeltjes bevinden, wordt gemodelleerd door een nanostaafmodel (b).

In Hoofdstuk 3 wordt de dissociatie van water op vlakke en gestapte oppervlakken (Figuur 1a), alsmede de rol van zuurstof-adatomen hierin, bestudeerd. Wij concluderen dat de waterdissociatie niet beïnvloed wordt door het coördinatiegetal van het betrokken oppervlakteatoom. De activeringsenergieën zijn 63 kJ/mol op het vlakke Rh(111)-oppervlak en 61 kJ/mol op het gestapte Rh(221)-oppervlak. Echter, in het bijzijn van een zuurstofatoom op het oppervlak, die kan dienen als ontvanger voor het waterstof, is de barrière op het

gestapte Rh(221)-oppervlak met 28 kJ/mol significant lager dan op het vlakke oppervlak (53 kJ/mol). Ondanks dit groot verschil, blijkt dat, bij nader onderzoek van het potentieel energie diagram, de totale barrière op het gestapte oppervlak ook rond 60 kJ/mol is, omdat de energie die nodig is om het adatoom in zijn meest gunstige positie te brengen ook erbij moet worden geteld. Dit proces is endothermisch als gevolg van de laterale interacties op het oppervlak. Een Brønsted-Evans-Polanyi-achtige correlatie van de activeringsenergieën met de metaal-hydroxylverbinding laat zien dat de overgangsvorm van waterdissociatie een lichtelijk laat karakter heeft. Daarnaast bestaat er ook een groot compensatie-effect bij het zuurstofondersteunde waterdissociatie-mechanisme.

Hoofdstuk 4 beschrijft de vergelijking van drie verschillende reactiepaden voor de vorming van CO op het vlakke Rh(111) en het gestapte Rh(211) oppervlak (Figuur 1a) vanuit de geabsorbeerde CH en O. Algemeen is bepaald dat het directe mechanisme via C+O recombinatie in competitie is met het mechanisme via een formyl tussenstap (HCO), en het pad via een alcoholachtige tussenstap (COH) niet gunstig is. Op het vlakke oppervlak is de barrière voor CH-dissociatie ~100 kJ/mol, maar de totale barrière voor CO-vorming is 180 kJ/mol. De vorming van de formyl tussenstap op het vlakke oppervlak heeft een activeringsenergie van 180 kJ/mol. De decompositie die daarop volgt naar CO en H is eenvoudig. De totale barrière voor de beide processen zijn erg gelijk aan elkaar. De aanwezigheid van stappen is gunstig voor formylvorming en verlaagt de barrière naar 93 kJ/mol. De invloed van de stappen op CH-dissociatie is miniem, wat tot resultaat heeft dat de totale barrière voor de vorming van formyl op het gestapte oppervlak de voorkeur heeft. De gevolgen van deze verschillen in reactiviteit worden onderzocht in relatie tot het deeltjesgrootte-effect op SMR. Deze reactie gewoonlijk plaats vind op relatief hoge temperaturen. Daarom zal de entropische vrije energie van de dissociatieve adsorptie van methaan significant hoger zijn dan de vrije energie van de CO-vormingsreacties. Het deeltjesgrootte-effect dat wordt waargenomen in experimenten, volgt de verandering in de activering van methaan. Dit zou het gevolg moeten zijn van de toenemende verhouding van gestapte en hoek-sites met de dalende deeltjesgrootte. Zou de C-O verbindingvorming de snelheidscontrolerende stap zijn, dan zou er een maximum in de snelheid van SMR als een functie van dalende deeltjesgrootte verwacht worden, omdat de kleinere deeltjes minder gestapte sites heeft voor CO-recombinatie. Op basis van de metaal-koolstof en metaal-zuurstof-vormingsenergie worden de periodieke trends van de elementaire reactiestap van SMR vergeleken. Voor de beste katalytische werking zijn koolstof- en zuurstofintermediären

nodig. De activering van methaan en water kan gerelateerd worden aan de metaal-koolstof en metaal-zuurstof-vormingsenergie. Als gevolg van de eis van optimale O-bezetting, is het metaal met de laagste activeringsenergie voor methaanactivering (Ir) niet het metaal met de hoogste activiteit voor SMR (Ru).

We vergelijken het energieverloop van de dehydrogenering van CH_4 tot C op de periodieke Rh(111) en Rh(211) oppervlakken, alsmede het vlakke (111) oppervlak en de hoekatomen tussen twee (111) facetten van een nanostaafmodel (Figuur 1b) in Hoofdstuk 5. Het blijkt dat vergelijkbare oppervlakken op het periodieke en nanostaafmodel bijna gelijke adsorptie en reactie-energieën hebben. Echter is dit niet het geval voor de adsorptie van het koolstof-adatoom, deze adsorbeert sterker op het (111)-oppervlak van de nanostaaf dan op het periodieke vlakke oppervlak. De reactie-energieën wijken slechts marginaal af als gevolg van kleine geometrische verschillen. De dissociatie van CH is op alle oppervlakken de reactie met de hoogste barrière. Echter als gevolg van het entropisch verlies gedurende de dissociatieve adsorptie van methaan, wordt deze adsorptie gezien als de meest waarschijnlijke snelheidsbepalende stap. In overeenstemming met de eerdere vergelijking van CO recombinitie op verschillende oppervlakken, is de barrière voor CH_4 -dissociatie sterk structuurafhankelijk. De snelheid is veel hoger op periodieke oppervlakken, die laag gecoördineerde oppervlakteatomen hebben.

In Hoofdstuk 6 is een microkinetisch model van SMR ontwikkeld en beschreven. Dit model is gebaseerd op de elementaire reactiestappen en stelt ons in staat om macroscopische eigenschappen te bepalen, zoals totale reactiesnelheid, snelheden van de individuele elementaire reactiestappen, oppervlaktebedekking en snelheidsbepalende parameters. De reactiesnelheidsconstanten zijn bepaald aan de hand van barrières en entropische bijdrages berekend door middel van DFT. Aan de hand van dit model kunnen we concluderen dat op het vlakke en het gestapte oppervlak de dissociatieve adsorptie van CH_4 snelheidsbepalend is. De snelheid op het gestapte oppervlak is hoger dan op het vlakke. Om een hoge activiteit te behouden is het duidelijk dat er een balans is in de snelheden van dissociatieve adsorptie van CH_4 , dissociatie van H_2O en de vorming van CO. Ondanks het feit dat methaandissociatie snelheidsbepalend is, is het nodig om voldoende O-adatomen te genereren om de koolstofhoudende oppervlakte-intermediären te verwijderen. Op het vlakke oppervlak bevinden zich onder standaard reactiecondities voldoende O_{ads} om C_{ads} te verwijderen. Echter de structuurafhankelijkheid van wateradsorptie is minder sterk dan die van de methaan adsorptie en dissociatie. Dit betekent dat de reactiesnelheid bij hoge temperaturen op gestapte

oppervlakken laag wordt als gevolg van O_{ads} leegloop en daarmee C_{ads} vergiftiging. De belangrijkste conclusie is dat de experimenteel waargenomen structuurafhankelijkheid in overeenstemming is met het idee van dat dissociatieve adsorptie van methaan op laag gecoördineerde oppervlakteatomen de snelheidsbepalende stap is. Echter om een hoge activiteit te behouden zijn er gestapte sites nodige om C_{ads} en O_{ads} met een lage barrière te kunnen verwijderen. De dichtheid van gestapte sites is daarentegen niet van belang, aangezien de vrije activeringsenergie voor CO-recombinatie op deze oppervlakken vele malen hoger is dan de vrije activeringsenergie voor dissociatieve CH_4 -adsorptie.

Dit proefschrift levert een compleet beeld van de Rh-gekatalyseerde SMR-reactie, waarin alle mogelijke snelheidsbepalende elementaire stappen, zijnde CH_4 en H_2O -dissociatie en CO-vorming, met gelijke nauwkeurigheid en methodes zijn onderzocht. Het is ook duidelijk dat een microkinetisch model nodig is om de exacte implicaties van onderliggende parameters te doorgronden. Dit onderzoek houdt alleen rekening met laterale interacties tussen geadsorbeerde CO. Daarnaast wordt er ook maar één type site verondersteld. In dit licht zou het interessant kunnen zijn om vergelijkbare simulaties uit te voeren aan de hand van kinetische Monte Carlo, waarbij het voordeel is dat (i) eenvoudige laterale interactie mee kunnen worden genomen, alsmede (ii) diffusie over het oppervlak, welke belangrijk is omdat de C_{ads} -vormingsplaats anders is dan de C_{ads} -verwijderingsplaats, en (iii) de aanwezigheid van verschillende sites in verschillende verhoudingen op een deeltje. Een andere mogelijke onderzoeksrichting is te vinden in het gebruik van Brønsted-Evans-Polanyi relaties om periodieke trends te voorspellen alsmede het gedrag van legeringen. Coking, deactivering als gevolg van koolstof-koolstof bindingsreacties, die het meest waarschijnlijk plaatsvinden op de vlakke facetten, zou ook een goed onderwerp zijn voor onderzoek.

Acknowledgements

Na meer dan vijf jaar hard werken, kom je op het punt dat het af is. En dat is natuurlijk ook het moment om terug te kijken en mensen die je tegen bent gekomen en vooral die geholpen hebben te bedanken.

Om te beginnen wil ik Rutger van Santen en Emiel Hensen bedanken voor de kans die ze me geboden hebben om de kennis die ik heb opgedaan bij Biomedische Technologie uit te bereiden. Ik heb de eerste zes maanden wel flink moeten bijspijkeren om precies te begrijpen waar ze het telkens over hadden, maar uiteindelijk kon ik het allemaal volgen en vooral aanvullen. Mede door hun inzet, inzicht en overredingskracht is dit werk geworden wat het is. Ook de mensen waarmee ik in dit project heb samengewerkt dank ik. Michel Ligthart was de experimentele tegenpool tijdens de vijf jaar, jammer dat we onze resultaten niet dicht genoeg bij elkaar hebben kunnen brengen om er een gezamenlijk paper van te maken. Ik ben met veel plezier je kamergenoot geweest. Ook de partners van ECN, Paul van Beurden en Jean-Pierre Pieterse moeten hierin gekend worden, zonder de samenwerking binnen het SenterNovem project, zou ik nooit aan dit project hebben kunnen beginnen. Aan Tonek Jansen heb ik dit project uiteindelijk te danken. Door het volgen van twee cursussen bij hem en wat assertief vragen kwam ik bij Rutger en Emiel terecht.

Tijdens de vijf jaar zijn er natuurlijk allerlei mensen die zich, naast Emiel en Rutger, ook met de inhoud bemoeid hebben. Ik ben in eerste instantie opgevangen door Willy Offermans, die mij de basis van VASP heeft uitgelegd, waarna Peter Vassilev dat stokje heeft overgenomen. Van Ionel Ciobica heb ik veel geleerd over berekeningen aan methaan en koolstofmonoxide. Mijn beste collega en goede vriend Evgeny Pidko, wat hebben wij veel plezier gehad op onze wetenschappelijke uitjes. Ook jij kon je af en toe mengen in de inhoud van mijn werk. Ook heb ik direct input gekregen van mijn enige student, Jeaphianne van Rijn, die samen met

Emiel van Kimmenade, heel veel werk verricht heeft voor het microkinetisch model. Zonder hun en de inzet van Emiel Hensen had Hoofdstuk 6 niet bestaan.

Ik wil ook graag alle collega's bedanken waar ik in al die jaren mee samen heb gewerkt op wetenschappelijk of vriendschappelijk niveau: Dilip, Neelesh, Denzil, Prabashni, Tiny, Robert, Arjan, Pijus, Michelle, Jos, Paul, Thijs, Jarno, Gilbert, Remco, Paul, Vittorio, Christiaan, Alessandro, Yejun, Yi, Hougchuan, Yanmei, Leilei, Chouchou, Xianyang, Tianwei, Volkan, Aysegul, Farid, Sami, Abdul-Karim, Peng, Shu-Xia, Bouke, Christina, Peiyuan, Lu, Ad, Adelheid, Brahim, Victor, Ivo, Pieter, Sharan, Bartek, Thuat, Ojwang, en natuurlijk de twee secretaresses bij wie ik mijn vele vragen kwijt kon Elise en Emma. Vooral de spontane gesprekken met Emma waren een verlichting in de tijd dat we burens waren. Bedankt voor de fijne werkomgeving!

Buiten het werk om heb ik mijn stoom goed kunnen afblazen in mijn hobby, honkbal. Ik wil vooral me verontschuldigen bij de jeugdteams voor die enkele keer dat ik wat minder vrolijk was, omdat er iets misgegaan was.

Natuurlijk wil ik eindigen met het noemen van mijn familie. Bij een recente promotie hoorde ik dat een persoon voor merendeel door "nature" en "nurture" gevormd wordt, daarvoor dank ik mijn ouders Maarten en Marianne. Graag noem ik mijn broertje René, mijn schoonouders Theo en Angeline en schoonfamilie Willeke, Patrizio, Johan, ik heb nooit echt goed kunnen uitleggen wat ik nu deed, maar ik hoop dat mijn presentatie en proefschrift het een en ander verhelderd heeft. Als allerlaatste bedank ik mijn lieve vrouw Marieke en mijn twee kinderen Femke en Thijmen, voor het plezier wat ik met hun beleef buiten het werk en onderzoek, ik houd zo veel van jullie.

Curriculum Vitae

Pieter Willem van Grootel is op 24 februari 1981 geboren in Roermond. Na het afronden van het Atheneum op het Bisschoppelijk College in Sittard in 1999 heeft hij Biomedische Technologie gestudeerd aan de Technische Universiteit Eindhoven. In 2006 is hij afgestudeerd binnen de groep BioMIM bij prof. Peter Hilbers op het onderwerp “Theoretical analysis of Hydroxylation by Cytochrome P450 Enzymes”. Aansluitend is hij een promotieproject gestart bij prof. Van Santen en prof. Hensen aan de Technische Universiteit Eindhoven waarvan de resultaten worden gepresenteerd in dit proefschrift. Sinds 2010 is hij in dienst als klinisch informaticus i.o. van het Maxima Medisch Centrum en het instituut School of Medical Physics and Engineering (SMPE/e) aan de Technische Universiteit Eindhoven.